# ROLE OF CONTINUUM IN REACTION DYNAMICS INVOLVING WEAKLY BOUND NUCLEI

By

## Sanat Kumar Pandit
PHYS01201104007

### Bhabha Atomic Research Centre, Mumbai

A thesis submitted to the
Board of Studies in Physical Sciences

In partial fulfillment of the requirements
For the Degree of

## DOCTOR OF PHILOSOPHY
*of*
## HOMI BHABHA NATIONAL INSTITUTE

March 2018

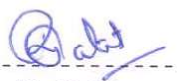# Homi Bhabha National Institute

## Recommendations of the Viva Voce Board

As members of the Viva Voce Board, we recommend that the dissertation prepared by **Sanat Kumar Pandit** entitled **"Role of continuum in reaction dynamics involving weakly bound nuclei"** may be accepted as fulfilling the dissertation requirement for the Degree of Doctor of Philosophy.

------------------------------------------------ Date : 26.03.2018
Chairman : Prof. A. K. Mohanty

------------------------------------------------ Date : 26.03.2018
Convener : Prof. A. Shrivastava

------------------------------------------------ Date : 26/03/2018
Member : Prof. B. K. Nayak

------------------------------------------------ Date : 26/03/2018
Member : Prof. R. Palit

------------------------------------------------ Date : 26/03/2018
External Examiner : Prof. Samit Kumar Mandal

Final approval and acceptance of this dissertation is contingent upon the candidate's submission of the final copies of the dissertation to HBNI.

I hereby certify that I have read this dissertation prepared under my direction and recommend that it may be accepted as fulfilling the dissertation requirement.

------------------------------------------------ Date : 26.03.2018
Guide : Prof. A. Shrivastava

I would like to thank my friends and colleagues P. Patale, Abhinav, Dr. C. S. Palshetkar, S. Gupta, T. N. Nag, Rajib, Dibyenduda, Sabya, Debes, Shiba bhai, Asim, Dipayan, A. Kundu, Rajendra, Dr. Y. K. Gupta, Somda, and L. S. Danu.

My special thank goes to Dr. S. Santra, Dr. B. J. Roy for inspiration and support in both on an academic and a personal level.

It is a great pleasure to thank Dr. G. Ravi Kumar, Dr. D. C. Biswas, Dr. A. K. Gupta, Dr. S. R. Jain and Mr. J. A. Gore for their support and encouragement.

I would also like to thank the technical staff of the Pelletron-Linac facilities, Indian National Gamma Array facilities, and target laboratory. The help of the NPD office staff and each and every member of NPD during this period are gratefully acknowledged.

I would like to take this opportunity to thank all my teachers from school to university who imparted value education and moral courage. I can't miss this opportunity to thank Utpal sir, whose magical and inspiring teaching deeply motivated me to choose research in physics as my scientific career.

To all my friends (Bhashkar, Vik, Arya, Ashish, Mazid, Mamu, KK, Nishant) who make my life a wonderful experience, thank you for your understanding and encouragement throughout. I cannot list all the names here, but you are always on my mind.

Finally, I owe my heartfelt gratitude and indebtedness to my parents, grandfathers, and Jahar mama for their love and support throughout my life. Thank you, Maa and Baba for giving me strength and freedom to chase my dreams. I am really indebted to my loving brothers Biplab and Arjun for their sacrifices, encouragement, love, and support that helped me to achieve what I am today. Last, but not the least, I thank my loving and supportive wife, Moni and my dustu, Tuplu who missed me at home while I was busy with the thesis work.

Sanat Kumar Pandit

# ACKNOWLEDGEMENTS

To

my grandfathers,

Late Shri Bishwanath Pandit

&

Late Shri Bhupendranath Pal

# DECLARATION

I, hereby declare that the investigation presented in the thesis has been carried out by me. The work is original and the work has not been submitted earlier as a whole or in part for a degree/diploma at this or any other Institution or University.

Sanat Kumar Pandit

# STATEMENT BY AUTHOR

This dissertation has been submitted in partial fulfillment of requirements for an advanced degree at Homi Bhabha National Institute (HBNI) and is deposited in the library to be made available to borrowers under rules of the HBNI.

Brief quotations from this dissertation are allowable without special permission, provided that accurate acknowledgement of source is made. Requests for permission for extended quotation from or reproduction of this manuscript in whole or in part may be granted by the Competent Authority of HBNI when in his or her judgment the proposed use of the material is in the interests of scholarship. In all other instances, however, permission must be obtained from the author.

Sanat Kumar Pandit

# Contents

# List of Tables

# List of Figures

# Bibliography

[1] L. F. Canto *et al.*, Phys. Rep. **596**, 1 (2015); L. F. Canto *et al.*, Phys. Rep. **424**, 1 (2006).

[2] J. J. Kolata *et al.*, Eur. Phys. J. A **52**, 123 (2016).

[3] N. Keeley *et al.*, Prog. Part. Nucl. Phys. **63**, 396 (2009).

[4] R. A. Broglia and A. Winther, *Heavy Ion Reactions, Lecture Notes Vol. I* (Addison-Wesley Publishing Company, Redwood City, CA, 1991), p. 114.

[5] G. R. Satchler, *Direct Reactions* (Clarendon, Oxford, 1983).

[6] A. Shrivastava *et al.*, Phys. Lett. B **633**, 463 (2006).

[7] A. Shrivastava *et al.*, Phys. Lett. B **718**, 931 (2013).

[8] R. J. de Meijer, R. Kamermans, Rev. Mod. Phys. **57**, 147 (1985).

[9] M. Dasgupta *et al.*, Phys. Rev. Lett. **82**, 1395 (1999).

[10] D. H. Luong *et al.*, Phys. Lett. B **695**, 105 (2011).

[11] I. J. Thompson, Comput. Phys. Rep. **7**, 167 (1988).

[12] A. Diaz-Torres *et al.*, Phys. Rev. Lett. **98**, 152701 (2007).

[13] S. K. Pandit *et al.*, Phys. Rev. C **93**, 061602 (2016).

[14] R. Palit *et al.*, Nucl. Instrum. Methods Phys. Res., Sect. A **680**, 90 (2012).

[15] S. K. Pandit *et al.*, Phys. Rev. C **96**, 044616 (2017).

reported in chapter 5 and 6, respectively. Chapter 7 contains the summary and conclusions. The future outlook is also included to improve the understanding of the reaction dynamics involving weakly bound nuclei.

ulated in $t$-capture and $\alpha$-capture reactions. The predicted compound nuclear contribution of $\alpha$-evaporation from the statistical model calculations account for 10-20% of the $\alpha$-inclusive cross-sections. The combination of $\alpha$-production due to, (a) $t$-capture, (b) evaporation from compound nucleus, and (c) breakup and nucleon transfer followed by breakup, explain almost all the measured $\alpha$-inclusive cross-sections for $^7$Li + $^{93}$Nb system at the measured energy range [15]. A systematic behavior of the $t$-capture and inclusive-$\alpha$ cross-sections for reactions involving $^7$Li over a wide mass range has also been carried out. The present measurements along with the systematic study for different systems suggest that the main source of the $\alpha$-production mechanism is $t$-capture. A complete data set together with the theoretical analysis has been reported in this thesis.

The thesis is organized into seven chapters. In chapter 1 importance of the study of reaction dynamics of weakly bound stable and unstable nuclei has been discussed. Present status of this subject, motivation and structure of the thesis work is described. Chapter 2 contains the details of experimental procedure along with a brief description of the Pelletron Linac Facility. The analysis method to identify different reaction mechanisms, cross-sections and error estimations are discussed. The details of the Monte Carlo simulations on 3-body kinematics for breakup fragments to interpret the measured data and efficiency estimation are documented in third chapter. The chapter 4 includes different nuclear models used to understand the measured data. Continuum discretized coupled channels (CDCC), coupled channels Born approximation (CCBA), statistical model for compound nuclear evaporation along with the classical dynamical trajectory calculations are briefly discussed in this chapter. The results from the measurements of breakup fragments in coincidence, and particle-$\gamma$ in coincidence have been

events from direct breakup of $^7$Li. Coupled channels Born approximation (CCBA) and continuum discretized coupled channels (CDCC) calculations were performed to explain the large number of observables. The mechanism direct transfer to unbound states of the ejectile, is responsible for the $\alpha + \alpha$ and $\alpha + d$ production. The total $\alpha$-yields from the three processes is found to be accounted for only $\sim 8$ % of the measured inclusive-$\alpha$.

The fragment-capture reaction mechanism was identified by measuring prompt $\gamma$-rays arising from the residue in coincidence with the outgoing particles. The absolute cross-sections of residues arising from capture of various fragments and complete fusion reaction have been extracted from the measurements of the characteristic $\gamma$-ray transitions employing in-beam and off-beam methods. The cross-sections of the residue that are stable and have even-even nucleons, were obtained from the yrast $\gamma$-ray transitions built on the ground state. In case of odd-even nuclei, the cross-sections were extracted by adding the $\gamma$-ray transitions feeding directly to the ground state. The $\beta$-unstable residues with reasonable half lives for decay were identified by measuring the off-beam $\gamma$-ray activity. The cross-sections were extracted following the half lives and intensity of each transitions.

The measured $t$-capture cross-sections are found to be more than $\alpha$-capture cross-sections at all the energies. The present study shows that the $t$-capture mechanism is the dominant reaction channel for the production of $\alpha$-particle and account for 62-73% of the measured $\alpha$-inclusive cross-sections. The $2n$ stripping ($^5$Li$^* \rightarrow \alpha + p$) cross-sections along with $1p$ pickup ($^8$Be$^* \rightarrow \alpha + \alpha$), inelastic excitation ($^7$Li$^* \rightarrow \alpha + t$) and $1n$ stripping ($^6$Li$^* \rightarrow \alpha + d$) explains $\sim$15% of the inclusive-$\alpha$ cross-sections. The statistical model calculations were performed to estimate the compound nuclear contribution in the cross-sections of residues pop-

normalization. The time stamped data were collected using PCI-PXI based digital data acquisition (DDAQ) system with a sampling rate of 100 MHz.

The off-beam $\gamma$-ray counting were carried out using an efficiency calibrated high-purity germanium (HPGe) detector. Low background was achieved by using a graded shielding (Cu, Cd sheets of thickness $\sim$2 mm each followed by 5 cm Pb). Aluminum catcher foils of thickness $\sim$1 mg/cm$^2$ were used along with each target foil to stop the recoiling residues. The target and catcher foil assemblies were irradiated for $\sim$6 h (beam current $\sim$ 50 nA) at each bombarding energies and counted together at a distance of 10 cm from the detector. The beam current was monitored using a CAMAC scaler, which recorded the integrated current in intervals of 1 min duration.

We now discuss about the different reaction mechanisms studied in the present work. Various breakup processes, breakup of $^7$Li ($^7$Li$^* \rightarrow \alpha + t$) together with 1$p$-pickup followed by breakup ($^8$Be $\rightarrow \alpha + \alpha$) and 1$n$-stripping followed by breakup ($^6$Li $\rightarrow \alpha + d$) were disentangled by analyzing the data in event by event mode. The breakup events from direct and resonance states were identified by extracting the relative energies. A simulation code on 3-body kinematics has been developed using the Monte Carlo technique to interpret the observables of different breakup processes and to estimate the efficiency for coincident detection of the breakup fragments. The energy spectra of each outgoing fragments were reproduced by simulation. The absolute cross-sections of all the above mentioned breakup processes have been extracted. Angular distributions for elastic scattering, neutron and proton transfer to bound states of $^6$Li and $^6$He, respectively, have also been measured. The cross sections for $\alpha + \alpha$ events from one proton pickup have been found to be smaller than those for $\alpha + d$ events from one neutron stripping and $\alpha + t$

energy resolution of individual strips were ~70 keV for the measurements of $\alpha$-particles from a $^{239}$Pu-$^{241}$Am-source. Three Si surface-barrier detector telescopes (thicknesses: $\Delta E \sim$ 20-50 $\mu$m, $E \sim$ 450-1000 $\mu$m) were also used to obtain the elastic scattering angular distribution at forward angles (25°-40°) where the count rate is too high for the strip detectors to cope with. Two Si surface-barrier detectors (thickness $\sim$ 300 $\mu$m) were kept at ±20° to monitor Rutherford scattering for absolute normalization.

Indian National Gamma Array (INGA) consisting 18 number of Compton suppressed clover detectors was used to measure the prompt $\gamma$-rays [14]. Each of the clovers has four n-type high purity germanium crystals kept in a single cryostat. Each crystal is connected to a low temperature FET coupled with the resistive charge sensitive preamplifier. The Compton suppressed BGO shield has 16 photo multiplier. The sum of the 16 photo multipliers is given to a timing filtering amplifier and then to the analogue constant fraction module which generates a NIM logic signal. This goes as an input to the digital data acquisition system for the veto of the clover signals. In this particular experiment 18 detectors were arranged in a spherical geometry with three detectors at 23°, six detectors at 40°, five detectors at 65°, and four detectors at 90° with respect to the beam direction. The distance from the target to crystal is 25 cm and the overall photo peak efficiency is around 2% at $E_\gamma = 1$ MeV. The efficiency and energy calibration of the Clover detectors were carried out using standard calibrated $\gamma$-ray sources $^{152}$Eu and $^{133}$Ba. Three Si surface barrier telescopes (thicknesses $\Delta E \sim$ 15-30 $\mu$m, $E \sim$ 300-5000 $\mu$m), were kept inside the scattering chamber at 35°, 45° and 70° for the detection of charged particles around the grazing angle. One Si surface barrier detector (thickness $\sim$ 300 $\mu$m) was kept at 20° to monitor Rutherford scattering for absolute

and complete fusion cross-sections were carried out for $^7$Li+$^{93}$Nb system by performing two independent experiments on prompt $\gamma$-ray counting and off-beam $\gamma$-radioactivity measurement. Both the measurements were performed at beam energies of 24, 26, 28 and 30 MeV, in which some of the energies are common with the measurement on breakup fragments in coincidence. The fragment-capture mechanism has been studied by performing exclusive particle-gamma coincidences measurements. Self-supporting $^{93}$Nb foils of thickness $\sim 1.6$ mg/cm$^2$ were used as target. Prompt $\gamma$-ray transitions were detected using the Indian National Gamma Array and out going fragments were measured using Si-surface-barrier detector telescopes. The off-beam $\gamma$-activity were measured using a high purity germanium (HPGe) detector. The details of all the detecting systems are given below.

Silicon strip detectors are widely used for charged particle detection in nuclear and particle physics experiments. We have used a set up, that consists of two segmented Si-detector telescopes, at the Mumbai Pelletron Linac Facility. Both the telescopes consist of $\Delta E$ and $E$-detector of thicknesses 50 $\mu$ and 1.5 mm, respectively. Active area of each of the strip detector was $5 \times 5$ cm$^2$. The $\Delta E$ detector was single sided with 16 strips on the junction side and $E$-detector was double sided with 16 strips on each side. These telescopes, set 30° apart, were mounted at a distance of 16 cm from the target on a movable arm inside a scattering chamber. In this geometry, the cone angle between the two detected fragments ranged from 1° to 24°. The angular range 30°-130° (around the grazing angle) was covered by measurements at different angle settings. Signals from individual strips were collected using multichannel preamplifier. These detectors were used to obtain position and energy-loss information. Particles were identified using energy loss information from $\Delta E$ and $E$ detectors of the telescopes. The typical

weakly bound projectile $^7$Li on targets around $Z$=40 $N$=50. Elastic scattering and fusion cross-sections have also been studied to get a complete understanding of the reaction dynamics. Origin of the source of large $\alpha$-production with $^7$Li having $\alpha - t$ cluster structure has been investigated by considering almost all the reaction channels contributing to the $\alpha$-yield. All the experiments documented in this thesis were performed at Pelletron Linac Facility, Mumbai. (a) To study the breakup and transfer-breakup reaction mechanisms, breakup fragments in coincidence have been measured. (b) The fragment-capture reaction has been studied by measuring $\gamma$-rays, emitted from the composite systems in coincidence with the non captured fragments. In-beam and off-beam methods were employed to measure the absolute formation cross-sections of the residues populated due to capture of various fragments and complete fusion reaction processes. Coupled channels calculations have been performed including bound and unbound states of different ejectile to understand direct reaction processes [11]. Classical dynamical trajectory model calculations have been carried out to explain the breakup-fusion cross-sections [12].

The breakup and transfer-breakup reaction processes were measured for $^7$Li+ $^{93}$Nb, $^{89}$Y systems at energies $E_{beam}$ = 24, 28, and 30 MeV. Self-supporting, $^{93}$Nb foil of thickness $\sim$ 1.75 mg/cm$^2$ and $^{89}$Y foil of thickness $\sim$ 2.0 mg/cm$^2$ were used as target. These two targets were chosen to investigate the role of the nuclear structure of the target on the various nucleon transfer channels. The breakup events from low lying states of ejectile lead to a very small relative angle between the fragments. The cross-sections of these reaction mechanism are also very small compared to elastic scattering cross-sections. These difficulties were overcome by using segmented large area Si-detectors. The measurements of fragment-capture

nificant [1, 2, 3]. The complete fusion (CF) cross section (absorption of all the charges of the projectile) is reported to be suppressed at above-barrier energies in comparison to the predictions of the barrier penetration model [1, 9]. It has been shown that the time scale of the breakup processes plays a crucial role in deciding dynamics of the complete fusion of the projectile with the target [10]. In case of reaction involving weakly bound nuclei with $\alpha + x$ cluster structure, e.g. $^{6,8}$He, $^{6,7}$Li, and $^{7,9}$Be, $\alpha$-particle production is found to be large compared to that of the complementary fragment. Investigation of the mechanisms responsible for the large $\alpha$-particle production cross sections is also a topic of current interest. Contributions to the alpha yield arising from different reaction mechanisms, such as breakup, transfer-breakup, cluster transfer, transfer followed by evaporation, incomplete fusion, compound nuclear evaporation, etc are entangled and it is not trivial to separate them from inclusive measurements. Experimentally it is challenging to disentangle these reaction processes, and exclusive measurements are essential. To understand the experimental observables, several models based on classical, quantum mechanical, and semi-classical theory have been developed over the past years. The continuum discretized coupled channels (CDCC) method [11] provides good results concerning certain observables such as the elastic scattering, breakup, transfer-breakup and total fusion (TF) (i.e., the sum of CF and ICF) cross sections. The classical dynamical trajectory model [12] can explain the ICF and CF data simultaneously, but does not include the quantum tunneling probability. Hence in theoretical modeling, there is a strong limitation as a single model is unavailable to calculate all observables simultaneously.

In the present thesis, extensive study of reactions populating the continuum, viz, breakup, transfer-breakup and fragment-capture, have been performed with

# SYNOPSIS

Exploring the properties of weakly-bound stable/unstable nuclei is a topic of current interest [1, 2, 3] and also focus of the next generation of high-intensity isotope-separator on-line (ISOL) radioactive ion beam facilities. Presence of loosely bound cluster structure and exotic shapes are the distinct features seen in these nuclei with respect to the tightly-bound nuclei. Due to the low breakup threshold, population of the continuum is probable and consequently a large coupling effect is expected in the reactions involving the weakly bound nuclei at energies around the Coulomb barrier. Continuum states can be populated by direct inelastic excitation of the projectile (breakup) or nucleon transfer, leaving the ejectile in an unbound state (transfer-breakup) [1, 2, 3, 4, 5, 6, 7]. The breakup processes occurring in the nuclear reaction time scale are called direct-breakup or prompt-breakup. Whereas in case of sequential or resonance breakup, the time scale is relatively long and depends on the lifetime of the unstable system [8]. Investigation of projectile breakup—whether direct or sequential— along with the transfer-breakup is crucial while studying the reaction dynamics of weakly bound nuclei. Another dominant reaction mode is transfer/capture of one of the cluster-fragment from bound/unbound state of the projectile to the target nuclei. Capture of a cluster-fragment from unbound states of the projectile can be looked upon as a two-step process, breakup followed by fusion (breakup-fusion) or incomplete fusion (ICF). This process is indistinguishable from the direct stripping of the cluster-fragment. However, it has been shown that breakup-fusion reaction is dominant over the one step stripping reaction. The admixture of these two reaction processes is generally referred to as fragment-capture [7]. Role of the breakup channels on the elastic scattering angular distribution and fusion cross-sections has been found to be sig-

1

Shrivastava, V. Nanal, and S. Pal DAE Symp. on Nucl. Phys. vol. 59, 560 (2014).

19. Measurement of direct breakup and transfer-breakup for $^{7}$Li+$^{89}$Y,$^{93}$Nb systems around the Coulomb barrier
**S. K. Pandit**, A. Shrivastava, K. Mahata, V. V. Parkar, P. C. Rout, C. S. Palshetkar, I Martel, Abhinav Kumar, A. Chatterjee, and S. Kailas
DAE Symp. on Nucl. Phys. vol. 57, 396 (2012).

20. Fission fragment angular distributions for $^{10,11}$B+$^{197}$Au systems
K. Mahata, A. Shrivastava, **S. K. Pandit**, K. Ramachandran, C. Palshetkar, A. Chatterjee, and S. Kailas
DAE Symp. on Nucl. Phys. vol. 57, 480 (2012).

21. Fusion using proximity potentials and effect of projectile breakup
P. K. Rath, S. Santra, N. L. Singh, K. Mahata, R. Palit, **S. K. Pandit**, A. Parihari, S. Appannababu, D. patel, B. K. Nayak, S. Kailas
DAE Symp. on Nucl. Phys. vol. 57, 518 (2012).

22. Universal behaviour of complete fusion suppression factor for $^{9}$Be projectile with different targets
V. Jha, V. V. Parkar, H. Kumawat, **S. K. Pandit**, and S. Kailas
DAE Symp. on Nucl. Phys. vol. 57, 572 (2012).

23. A protoype FPGA-based digital pulse processing system
J. A. Gore, S. G. Kulkarni, A. Shrivastava, K. Mahata, **S. K. Pandit**, V. V. Parkar, A. Chatterjee, P. V. Bhagwat, and S. Kailas
DAE Symp. on Nucl. Phys. vol. 57, 900 (2012).

Sanat Kumar Pandit

and S. Kailas
DAE Symp. on Nucl. Phys. vol. 59, 372 (2014).

13. np pairing correlation study in $^{10}$B+$^{209}$Bi reaction
V. V. Parkar, A. Shrivastava, **S. K. Pandit**, K. Mahata, V. Jha, P. Patale
DAE Symp. on Nucl. Phys. vol. 59, 568 (2014).

14. Multi-nucleon Transfer Study at above the Coulomb Barrier $E_{c.m.}/V_C \sim 1.6$
B. J. Roy, U. K. Pal, Sonika, A. Parmar, V. Jha, **S. K. Pandit**, V. V. Parkar, K. Ramachandran, K. Mahata, A. Pal, , A. Parihari, S. Santra, and A. K. Mohanty
DAE Symp. on Nucl. Phys. vol. 59, 80 (2014).

15. Analysis of Elastic Scattering Cross Section for $^{18}$O+$^{206}$Pb in the CRC Formalism and. Dependence on the Choice of Double Folding Potential
Sonika, B. J. Roy, A. Parmar, V. Jha, U. K. Pal, T. Sinha, **S. K. Pandit**, V. V. Parkar, K. Ramachandran, K. Mahata, A. Pal, A. Parihari, S. Santra, and A. K. Mohanty
DAE Symp. on Nucl. Phys. vol. 59, 314 (2014).

16. Fusion hindrance for asymmetric systems at extreme sub barrier energies
A. Shrivastava, K. Mahata, **S. K. Pandit**, V. Nanal, T. Ichikawa, K. Hagino, C. S. Palshetkar, V. V. Parkar, K. Ramachandran, P. C. Rout, Abhinav Kumar, P. Patale, A. Chatterjee, S. Kailas
DAE Symp. on Nucl. Phys. vol. 59, 338 (2014).

17. Two-neutron Transfer Reaction Mechanism in $^{18}$O+$^{206}$Pb below the Coulomb Barrier: Extreme Cluster Model Calculations assuming Di-neutron Transfer
B. J. Roy, A. Parmar, Sonika, V. Jha, U. K. Pal, T. Sinha, **S. K. Pandit**, V. V. Parkar, K. Ramachandran, K. Mahata, A. Pal, A. Parihari, S. Santra, and A. K. Mohanty
DAE Symp. on Nucl. Phys. vol. 59, 402 (2014).

18. Fragment emission mechanism in $^{12,13}$C+$^{12}$C reactions
S. Manna, C. Bhattacharya, T. K. Rana, V. Srivastava, K. Banerjee, S. Kundu, P. Roy, R. Pandey, A. Chaudhury, T. Roy, T. K. Ghosh, G. Mukherjee, S. Bhattacharya, J.K. Meena, **S. K. Pandit**, K. Mahata, P. Patale, A.

Ramachandran, A. Kumar, S. Gupta, and P. Patale
DAE Symp. on Nucl. Phys. vol. 60, 1042 (2015).

8. Understanding Reaction Mechanisms of Multi-nucleon Transfer Reactions in Deformed Nuclei
B. J. Roy, Anjali Aggarwal, Shivani, Taniya Basu, Sonika, H. Kumawat, **S. K. Pandit**, V. V. Parkar, K. Ramchandran, K. Mahata, A. Pal, A. Kundu, D. Chattopadhyay, S. Santra, T. Sinha, A. K. Mohanty, and K. Sakizawa
DAE Symp. on Nucl. Phys. vol. 60, 328 (2015).

9. Reaction Mechanism Studies of Multi-nucleon Transfer Reactions in $^{208}$Pb($^{16}$O,x) and comparison with $^{206}$Pb($^{18}$O,x)
B. J. Roy, K. Sakizawa, Sonika, Taniya Basu, Shivani, Anjali Aggarwal, H. Kumawat, **S. K. Pandit**, V. V. Parkar, K. Ramchandran, K. Mahata, A. Pal, A. Kundu, D. Chattopadhyay, S. Santra, T. Sinha, and A. K. Mohanty
DAE Symp. on Nucl. Phys. vol. 60, 392 (2015).

10. Role of fusion fission process on fragment emission mechanism in 32S+12C reaction
R. Pandey, C. Bhattacharya, S. Kundu, K. Banerjee, S. Manna, T. K. Rana, J. K. Meena, T. Roy, A. Chaudhari, Md. A. Asgar, V. Srivastava, A. Dey, M. Sinha, G. Mukherjee, P. Roy, T. K. Ghosh, S. Bhattacharya, A. Srivastava, K. Mahata, **S. K. Pandit**, P. Patle, S. Pal, V. Nanal
DAE Symp. on Nucl. Phys. vol. 60, 544 (2015).

11. Complete and incomplete fusion for $^{7}$Li+$^{93}$Nb reaction
**S. K. Pandit**, A. Shrivastava, K. Mahata, V. V. Parkar, R. Palit, S. Bhattacharya, V. Nanal, P. C. Rout, A. Kumar, K. Ramachandran, P. Gupta, S. Biswas, S. Saha, J. Sethi, P. Singh, and S. Kailas
DAE Symp. on Nucl. Phys. vol. 59, 340 (2014).

12. Study of breakup and transfer breakup reactions in $^{7}$Li+$^{93}$Nb system around the Coulomb barrier
**S. K. Pandit**, A. Shrivastava, K. Mahata, V. V. Parkar, P. C. Rout, I. Martel, C. S. Palshetkar, A. Kumar, K. Ramachandran, P. Patale, A. Chatterjee,

A. Chatterjee, S. Kailas

DAE Symp. on Nucl. Phys. vol. 61, 384 (2016).

2. Measurement of pre-fission neutron multiplicity for $^7$Li+$^{203}$Tl at E* ~43.8 MeV

K. Mahata, K. Ramachandran, P. C. Rout, A. Shrivastava, **S. K. Pandit**, V. V. Parkar, Shilpi Gupta, V. V. Desai, A. Kumar, P. Patale, E. T. Mirgule, B. K. Nayak, A. Saxena DAE Symp. on Nucl. Phys. vol. 61, 398 (2016).

3. Fusion hindrance at deep-sub barrier energies in $^{11}$B + $^{197}$Au

A. Shrivastava, K. Mahata, V. Nanal, **S. K. Pandit**, V. V. Parkar, P. C. Rout, N. Dokania, K. Ramachandran, A. Kumar, P. Patale, A. Chatterjee, S. Kailas DAE Symp. on Nucl. Phys. vol. 61, 402 (2016).

4. Fission Fragment mass distribution for neutron deficient nuclei in A~200 region

Shilpi Gupta, A. Shrivastava, K. Mahata, K. Ramachandran, **S. K. Pandit**, P. C. Rout, V. V. Parkar, G. Mohanto, A. Parihari, A. Kumar, P. Patale, B. K. Nayak, E. T. Mirgule, A. Saxena, A. Jhingan, P. Sugathan DAE Symp. on Nucl. Phys. vol. 61, 606 (2016).

5. Study of breakup and transfer breakup reactions in $^7$Li+$^{198}$Pt system around the Coulomb barrier

**S. K. Pandit**, A. Shrivastava, K. Mahata, K. Ramachandran, V. V. Parkar, P. C. Rout, A. Kumar, P. Patale, U. Singh, and S. Kailas DAE Symp. on Nucl. Phys. vol. 60, 396 (2015).

6. Study of continuum states of ejectiles in $^7$Li+$^{93}$Nb reaction around the Coulomb barrier

**S. K. Pandit**, A. Shrivastava, K. Mahata, N. Keeley, V. V. Parkar, P. C. Rout, I. Martel, C. S. Palshetkar, A. Kumar, K. Ramachandran, P. Patale, A. Chatterjee, and S. Kailas DAE Symp. on Nucl. Phys. vol. 60, 398 (2015).

7. Digital pulse shape analysis for charged particle identification with a nTD silicon detector and 1 GHz sampling digitizer

K. Mahata, J. A. Gore, A. Shrivastava, **S. K. Pandit**, V. V. Parkar, K.

2. Exclusive measurement of direct- and transfer-breakup reactions for $^7$Li+$^{89}$Y,$^{93}$Nb systems
   **S. K. Pandit**, A. Shrivastava, K. Mahata, V. V. Parkar, P. C. Rout, I. Martel, C. S. Palshetkar, A. Kumar, P. Patale, A. Chatterjee, and S. Kailas
   International Symposium on Nuclear Physics, vol. 58, 518 (2013)

3. Fusion and transfer studies in $^7$Li+$^{124}$Sn reaction by offline gamma counting technique
   V. V. Parkar, A. Shrivastava, K. Mahata, **S. K. Pandit**, P. K. Rath, R. Palit, S. Santra, V. Jha, and P. Patale
   International Symposium on Nuclear Physics, vol. 58, 506 (2013)

4. Coupled channel effects in quasi-elastic barrier distributions of $^{16,18}$O+$^{208}$Pb systems
   V. Jha, B.J. Roy, V.V. Parkar, H. Kumawat, U.K. Pal, **S. K. Pandit**, K. Mahata, A. Shrivastava, and A.K. Mohanty
   International Symposium on Nuclear Physics, vol. 58, 578 (2013)

5. Search for the 2$^+$ state built on the Hoyle State
   Suresh Kumar, A. Pal, P.C. Rout, Abhijit Bhattacharyya, S.P. Behera, R. Kujur, Ajay Kumar, K. Mahata, E.T. Mirgule, G. Mishra, A. Mitra, **S. K. Pandit**, A. Parihari, S. Santra, A. Shrivastava, and V.M. Datar
   International Symposium on Nuclear Physics, vol. 58, 580 (2013)

6. Particle identification using pulse shape discrimination in a nTD silicon detector with a 1 GHz sampling digitizer
   K. Mahata, J. A. Gore, A. Shrivastava, **S. K. Pandit**, V. V. Parkar, A. Kumar, and P. Patale
   International Symposium on Nuclear Physics, vol. 58, 902 (2013)

**List of publication in National Conference/ Symposium/ Reports :**

1. Study of reactions populating unbound states for $^7$Li+$^{89}$Y system around the Coulomb barrier
   **S. K. Pandit**, A. Shrivastava, K. Mahata, N. Keeley, V. V. Parkar, P. C. Rout, K. Ramachandran, I. Martel, C. S. Palshetkar, A. Kumar, P. Patale,

18. Fusion reaction studies for the $^6$Li + $^{90}$Zr system at near-barrier energies
    H. Kumawat, V. Jha, V. V. Parkar, B. J. Roy, **S. K. Pandit**, R. Palit, P. K. Rath, C. S. Palshetkar, Sushil K. Sharma, Shital Thakur, A. K. Mohanty, A. Chatterjee, and S. Kailas
    Phys. Rev. C **86**, 024607 (2012).

19. Complex-fragment emission in low-energy light-ion reactions
    S. Kundu, C. Bhattacharya, K. Banerjee, T. K. Rana, S. Bhattacharya, A. Dey, T. K. Ghosh, G. Mukherjee, J. K. Meena, P. Mali, S. Mukhopadhyay, D. Pandit, H. Pai, S. R. Banerjee, D. Gupta, P. Banerjee, Suresh Kumar, A. Shrivastava, A. Chatterjee, K. Ramachandran, K. Mahata, **S. K. Pandit**, and S. Santra
    Phys. Rev. C **85**, 064607 (2012).

20. Systematics of pre- and near-scission $\alpha$-particle multiplicities in heavy-ion-induced fusion-fission reactions
    Y. K. Gupta, D. C. Biswas, R. K. Choudhury, A. Saxena, B. K. Nayak, Bency John, K. Ramachandran, R. G. Thomas, L. S. Danu, B. N. Joshi, K. Mahata, **S. K. Pandit**, and A. Chatterjee
    Phys. Rev. C **84**, 031603(R) (2011).

21. Investigation of cluster structure of $^9$Be from high precision elastic scattering data
    **S. K. Pandit**, V. Jha, K. Mahata, S. Santra, C. S. Palshetkar, K. Ramachandran, V. V. Parkar, A. Shrivastava, H. Kumawat, B. J. Roy, A. Chatterjee, and S. Kailas
    Phys. Rev. C **84**, 031601(R) (2011).

**List of publication in International Conference/Symposium:**

1. Measurement of evaporation residue cross sections for $^{11}$B+$^{197}$Au system
   K. Mahata, A. Shrivastava, **S. K. Pandit**, V.V. Parkar, P.C. Rout, N. Dokania, and V. Nanal
   75-years of Nuclear Fission: Present status and Future Perspectives, 63 (2014)

jee, P. Roy, R. Pandey, V. Srivastava, A. Chaudhuri, T. Roy, T. K. Ghosh, G. Mukherjee, J. K. Meena, **S. K. Pandit**, K. Mahata, A. Shrivastava, and V. Nanal
Phys. Rev. C **94**, 051601(R) (2016).

12. Multinucleon transfer study in $^{206}$Pb($^{18}$O,x) at energies above the Coulomb barrier
Sonika, B. J. Roy, A. Parmar, U. K. Pal, H. Kumawat, V. Jha, **S. K. Pandit**, V. V. Parkar, K. Ramachandran, K. Mahata, A. Pal, S. Santra, A. K. Mohanty, and K. Sekizawa
Phys. Rev. C **92**, 024603 (2015).

13. Understanding the two neutron transfer reaction mechanism in $^{206}$Pb($^{18}$O,$^{16}$O)$^{208}$Pb
A. Parmar, Sonika, B. J. Roy, V. Jha, U. K. Pal, T. Sinhab, **S. K. Pandit**, V. V. Parkar, K. Ramachandran, K. Mahata, S. Santra, and A. K. Mohanty
Nucl. Phys. A **940**, 167 (2015).

14. Elastic scattering and $\alpha$ production in the $^9$Be $+^{89}$Y system
C. S. Palshetkar, S. Santra, A. Shrivastava, A. Chatterjee, **S. K. Pandit**, K. Ramachandran, V. V. Parkar, V. Nanal, V. Jha, B. J. Roy, and S. Kalias
Phys. Rev. C **89**, 064610 (2014).

15. Complete fusion in $^7$Li$+^{144,152}$Sm reactions
P. K. Rath, S. Santra, N. L. Singh, B. K. Nayak, K. Mahata, R. Palit, K. Ramachandran, **S. K. Pandit**, A. Parihari, A. Pal, S. Appannababu, Sushil K. Sharma, D. Patel, and S. Kailas
Phys. Rev. C **88**, 044617 (2013).

16. High spin spectroscopy of $^{201}$Tl
S. Das Gupta, S. Bhattacharyya, H. Pai, G. Mukherjee, Soumik Bhattacharya, R. Palit, A. Shrivastava, A. Chatterjee, S. Chanda, V. Nanal, **S. K. Pandit**, S. Saha, J. Sethi, and S. Thakur
Phys. Rev. C **88**, 044328 (2013).

17. Exploring the breakup and transfer coupling effects in $^9$Be elastic scattering
V. V. Parkar, V. Jha, **S. K. Pandit**, S. Santra, and S. Kailas
(Phys. Rev. C **87**, 034602 (2013).)

6. Deep-inelastic multinucleon transfer processes in the $^{16}O+^{27}Al$ reaction
   B. J. Roy, Y. Sawant, P. Patwari, S. Santra, A. Pal, A. Kundu, D. Chattopadhyay, V. Jha, **S. K. Pandit**, V. V. Parkar, K. Ramachandran, K. Mahata, B. K. Nayak, A. Saxena, S. Kailas, T. N. Nag, R. N. Sahoo, P. P. Singh, and K. Sekizawa
   Phys. Rev. C **97**, 034603 (2018).

7. Fusion hindrance at deep sub-barrier energies for the $^{11}B+^{197}Au$ system
   A. Shrivastava, K. Mahata, V. Nanal, **S. K. Pandit**, V. V. Parkar, P. C. Rout, N. Dokania, K. Ramachandran, A. Kumar, A. Chatterjee, and S. Kailas
   Phys. Rev. C **96**, 034620 (2017).

8. Fragment emission mechanism in the $^{32}S + ^{12}C$ reaction
   Ratnesh Pandey, S. Kundu, C. Bhattacharya, K. Banerjee, T. K. Rana, S. Manna, G. Mukherjee, J. K. Meena, A. Chaudhuri, T. Roy, Pratap Roy, Md. A. Asgar, V. Srivastava, A. Dey, M. Sinha, T. K. Ghosh, S. Bhattacharya, **S. K. Pandit**, K. Mahata, P. Patle, A. Shrivastava, and V. Nanal
   Phys. Rev. C **95**, 064603 (2017).

9. Deformed band structures at high spin in $^{200}Tl$
   S. Bhattacharya, S. Bhattacharyya, S. Das Gupta, H. Pai, G. Mukherjee, R. Palit, F. R. Xu, Q. Wu, A. Shrivastava, Md. A. Asgar, R. Banik, T. Bhattacharjee, S. Chanda, A. Chatterjee, A. Goswami, V. Nanal, **S. K. Pandit**, S. Saha, J. Sethi, T. Roy, and S. Thakur
   Phys. Rev. C **95**, 014301 (2017).

10. Evolution of fusion hindrance for asymmetric systems at deep sub-barrier energies
    A. Shrivastava, K. Mahata, **S. K. Pandit**, V. Nanal, T. Ichikawa, K. Hagino, A. Navin, C. S. Palshetkar, V. V. Parkar, K. Ramachandran, P. C. Rout, Abhinav Kumar, A. Chatterjee, and S. Kailas
    Phys. Lett. B **755**, 332 (2016).

11. Survival of cluster correlation in dissipative binary breakup of $^{24,25}Mg^*$
    S. Manna, T. K. Rana, C. Bhattacharya, S. Bhattacharya, S. Kundu, K. Baner-

# LIST OF PUBLICATIONS

1. * Probing transfer to unbound states of the ejectile with weakly bound $^7$Li on $^{93}$Nb
   **S. K. Pandit**, A. Shrivastava, K. Mahata, N. Keeley, V. V. Parkar, P. C. Rout, I. Martel, C. S. Palshetkar, A. Kumar, K. Ramachandran, P. Patale, A. Chatterjee, and S. Kailas
   Phys. Rev. C **93**, 061602(R) (2016).

2. * Investigation of large $\alpha$-production in reactions involving weakly bound $^7$Li
   **S. K. Pandit**, A. Shrivastava, K. Mahata, V. V. Parkar, R. Palit, N. Keeley, P. C. Rout, A. Kumar, K. Ramachandran, S. Bhattacharyya, V. Nanal, C. S. Palshetkar, T. N. Nag, Shilpi Gupta1, S. Biswas, S. Saha, J. Sethi, P. Singh, A. Chatterjee, and S. Kailas
   Phys. Rev. C **96**, 044616 (2017).

3. * Study of reactions populating unbound states of ejectile with weakly bound $^7$Li on $^{89}$Y
   **S. K. Pandit**, A. Shrivastava, K. Mahata, N. Keeley, V. V. Parkar, P. C. Rout, I. Martel, C. S. Palshetkar, A. Kumar, K. Ramachandran, P. Patale, A. Chatterjee, and S. Kailas
   Phys. Rev. C (to be submitted).

4. Investigation of complete and incomplete fusion in the $^7$Li+$^{124}$Sn reaction near Coulomb barrier energies
   V. V. Parkar, Sushil K. Sharma, R. Palit, S. Upadhyaya, A. Shrivastava, **S. K. Pandit**, K. Mahata, V. Jha, S. Santra, K. Ramachandran, T. N. Nag, P. K. Rath, Bhushan Kanagalekar, and T. Trivedi
   Phys. Rev. C **97**, 014607 (2018).

5. Particle identification using digital pulse shape discrimination in a nTD silicon detector with a 1 GHz sampling digitizer
   K. Mahataa, A. Shrivastavaa, J.A. Gore, **S. K. Pandit**, V.V. Parkar, K. Ramachandran, A. Kumar, S. Gupta, P. Patale
   Nucl. Instrum. Methods Phys. Res., Sect. A in press (2018).

*This thesis work is based on these papers

along with corresponding error are discussed. The chapter 3 is devoted to different theoretical models, which have been used to understand the measured data. Continuum discretized coupled channels (CDCC), coupled channels Born approximation (CCBA), statistical model for compound nuclear evaporation along with the classical dynamical trajectory calculations are briefly discussed in this chapter. The chapter 4 includes details of the Monte Carlo simulations of 3-body kinematics for breakup fragments to interpret the measured data and to estimate coincidence efficiency. The results obtained from the measurements of breakup fragments in coincidence are given in chapter 5. The study of various breakup processes along with the theoretical descriptions are reported. The investigated results from the study of fragment-capture reaction mechanisms are included in the chapter 6. A simultaneous description of breakup, incomplete fusion, and complete fusion, from classical dynamical trajectory calculations is also given. Chapter 7 contains the summary and conclusions. The future outlook is also included to improve the understanding of the reaction dynamics involving weakly bound nuclei.

residue formed due to the capture of the complementary fragment is required. In theoretical description, the use of a full quantum mechanical formalism is ideal. However, no such model currently exists. The only available classical dynamical trajectory model is based on semi-classical theory. In this view, the detail study of fragment-capture reaction is crucial for the complete understanding of the reaction dynamics of weakly bound nuclei.

Another interesting unresolved problem in this context is the large $\alpha$-yield compared to that of the complementary fragments. Most of the reaction mechanisms, which are mentioned above, along with the compound nuclear evaporation contribute to the production of $\alpha$-particle. To understand the role of different reaction processes in the $\alpha$-production and to get total accountability of the $\alpha$-yield, simultaneous measurements of all the reactions channels are required.

The present thesis work aims to study the reaction dynamics involving weakly bound nuclei $^7$Li in view of all the important points mentioned above. The motivation of the thesis are simultaneous understanding of all the reaction mechanism, their relative importance, the role of cluster structure in reaction dynamics and the total accountability of the large $\alpha$-yield.

## 1.5.1 Plan of the thesis

The thesis is organized into seven chapters. The present chapter discuss about the importance of the study of reaction dynamics of weakly bound stable and unstable nuclei. Present status of this subject, motivation and structure of the thesis work is described. In chapter 2, the details of experimental procedure along with a brief description of the Pelletron Linac Facility are documented. The analysis method to identify different reaction mechanisms and estimation of cross sections

well as theoretical calculations are required to understand the interplay between them. Among the limited exclusive measurements aimed at studying different breakup processes, very few data on absolute cross sections are available for direct breakup [23, 37, 38, 39, 40, 45], while for transfer-breakup absolute differential cross sections are only available for the neutron transfer channels at energies close to the Coulomb barrier [23, 39].

Among the processes discussed above, investigation of the two-step reaction mechanism, viz., one nucleon transfer followed by breakup, is of current interest for the weakly bound stable nuclei $^{6,7}$Li and $^9$Be [23, 41, 42, 43, 44, 46, 49]. This complex process needs the simultaneous understanding of both the breakup and transfer reactions. In an earlier measurement of the $^7$Li+$^{65}$Cu system [23], it was observed that $1n$-stripping leading to $^6$Li in its unbound $3_1^+$ excited state is more probable than inelastic excitation of $^7$Li to its resonant states. In recent measurements with $^7$Li [41, 42], the importance of $1p$-pickup over the direct breakup of the projectile was highlighted while explaining the suppression of fusion at energies above the Coulomb barrier. Hence, understanding the mechanism of projectile breakup—whether direct or transfer breakup—is crucial while studying the reaction dynamics of weakly bound nuclei.

The fragment-capture reaction is an equally interesting reaction channel. As mentioned in Sec. 1.3.3, the complexity in the study of the fragment-capture reaction is that, the two-step process breakup-fusion is indistinguishable from the direct stripping of the cluster-fragment. To understand the relative importance of the one step and two step processes, extensive effort is required in both experimental side and theoretical modeling. From experimental point of view, the coincident measurements of the outgoing fragments with the prompt $\gamma$-rays arising from the

## 1.4    Theoretical models

Several models based on classical, quantum mechanical, and semi-classical theory have been developed over the past years to understand the reaction mechanisms involving weakly bound nuclei. Here, the most challenging task is the inclusion of the continuum states in the analysis. In the continuum discretized coupled channels (CDCC) method [35], the continuum states are included in the calculations. The CDCC frame work is one of the successful formalism to describe the elastic scattering, breakup, transfer-breakup and total fusion (TF) (i.e., the sum of CF and ICF) cross sections simultaneously. In this model calculation CF and ICF can not be estimated separately. The recently developed classical dynamical trajectory model [31, 36] can explain the ICF and CF data simultaneously. The main limitation of the dynamical trajectory model is that, the quantum tunneling probability is not included in the calculations. Hence, there is a strong limitation in theoretical modeling, as a single model is unavailable to calculate all observables simultaneously.

## 1.5    Motivation of the thesis

Presence of loosely bound cluster structure and exotic shapes are the distinct features seen in these nuclei with respect to the tightly-bound nuclei. As discussed in Sec. 1.2 and  1.3, due to the low breakup threshold, population of the continuum is probable and consequently a large coupling effect is expected at energies around the Coulomb barrier [4, 5, 23, 25, 37, 38, 39, 40, 41, 42, 43, 44, 45, 46, 47, 48]. Exclusive measurements are essential to disentangle the reaction processes listed in Sec. 1.3. Also, complete measurements of different reaction channels as

the cluster-fragment. However, it has been shown that breakup-fusion is dominant over the one step stripping reaction [28, 29, 30]. The admixture of these two reaction processes is generally referred to as fragment-capture [27, 28, 29, 30].

### 1.3.4 Complete fusion

In case of weakly bound nuclei, fusion of the two colliding nuclei forming the compound nucleus, can occur in two different ways. The complete fusion involves the capture of the whole projectile by the target. The breakup followed by complete fusion (BCF) is the process when breakup does occur followed by the capture of all the fragments [4, 31]. From the experimental point of view, these two processes can not be separated.

### 1.3.5 Large $\alpha$-yield

One of the interesting observation in case of reactions involving weakly bound nuclei with $\alpha + x$ cluster structure, e.g. $^{6,8}$He, $^{6,7}$Li, and $^{7,9}$Be, is the large $\alpha$-yield compared to that of the complementary fragments [3, 4, 5, 32]. Investigation of the mechanisms responsible for such large inclusive $\alpha$-particle production cross sections is of current interest [33, 34]. Different reaction mechanisms, e.g. breakup (direct and sequential), nucleon transfer followed by breakup, cluster transfer, incomplete fusion (only part of the projectile fuses), and compound nuclear (CN) evaporation, contribute to the $\alpha$ yield. It is difficult to separate the contributions of these individual reaction mechanisms from an inclusive $\alpha$-particle spectrum. Exclusive measurements are therefore needed to investigate the origins of the large $\alpha$ production and to study the role of the weakly bound cluster structure in the reaction dynamics.

scattering and fusion reactions [3, 6, 22].

## 1.3.2  Transfer-breakup

There are two types of transfer reactions, which are the stripping reaction and pickup reaction. In case of stripping reaction, part of the incident projectile is stripped away and enters the target nucleus. Whereas, in pickup reactions, the outgoing emitted particle is a combination of the incident projectile and one or more target nucleons. The breakup of an ejectile following transfer reaction is called transfer-breakup, which is a two step process [6, 23, 24, 25]. The study of transfer-breakup process is crucial for the understanding of transfer form factor. Transfer-breakup reaction mechanism is a good probe to choose the best configuration in the projectile wave function [25]. A limit on absolute cross section of two-step process $n$-transfer followed by breakup of $^6$Li via its $3^+$ state was reported for $^7$Li+$^{197}$Au system from coincidence measurement [25]. A detailed study of this two step reaction mechanism from coincidence measurements together with theoretical modeling, was carried out for $^7$Li+$^{65}$Cu system [23]. $1p$-peakup followed by breakup has been reported for $^7$Li+$^{40}$Ca system at energies much above the barrier [26].

## 1.3.3  Fragment-capture

Another dominant reaction mode is transfer/capture of one of the cluster-fragment from bound/unbound state of the projectile to the target nuclei. Capture of a cluster-fragment from unbound states of the projectile can be looked upon as a two-step process, breakup followed by fusion (breakup-fusion) or incomplete fusion (ICF) [27, 28, 29, 30]. This process is indistinguishable from the direct stripping of

## 1.3.1 Non-capture breakup

Breakup is a reaction process where the projectile splits into two or more fragments, due to the Coulomb and/or nuclear interactions with the target [6, 21]. The non-capture breakup processes are those where none of the breakup fragments are captured by the target. When the target remains in its ground state, such non capture breakup processes are referred as elastic breakup. The target nucleus remains spectator during the elastic breakup process. The breakup of the nuclei could be possible from the continuum states as well as from the resonance states. A typical strength distribution of breakup from continuum and resonance states is shown in figure 1.5.
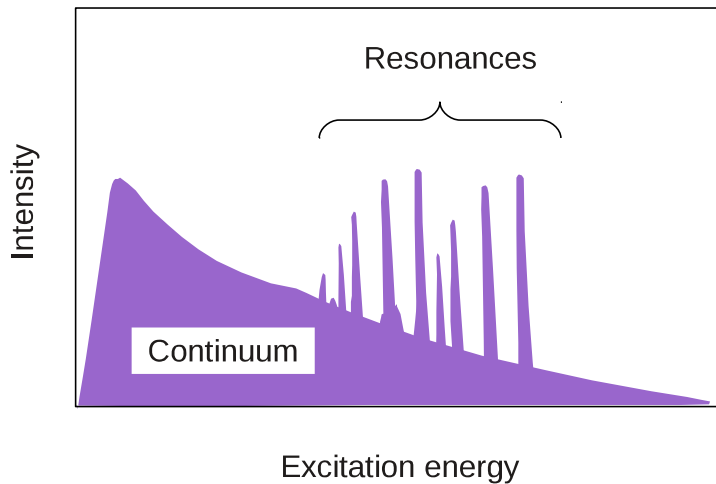


Figure 1.5: A typical strength distribution of breakup from continuum and resonance states.

The breakup processes occurring in the nuclear reaction time scale are called direct-breakup or prompt-breakup. Whereas in case of sequential or resonance breakup, the time scale is relatively long and depends on the lifetime of the unstable system [21]. There is a strong coupling effect of the breakup channels on the elastic

(3) Nucleon transfer leading to the unbound state of the ejectile,

(4) Mechanism of fragment capture reaction, where part of the projectile is captured by the target nuclei,

(5) Time scale of the breakup processes, etc.

Some of the possible dominant reaction processes in case of reactions involving low energy weakly bound nuclei with only two clusters are shown in Fig. 1.4. Now we discuss the details of the reaction mechanisms displayed in the figure.
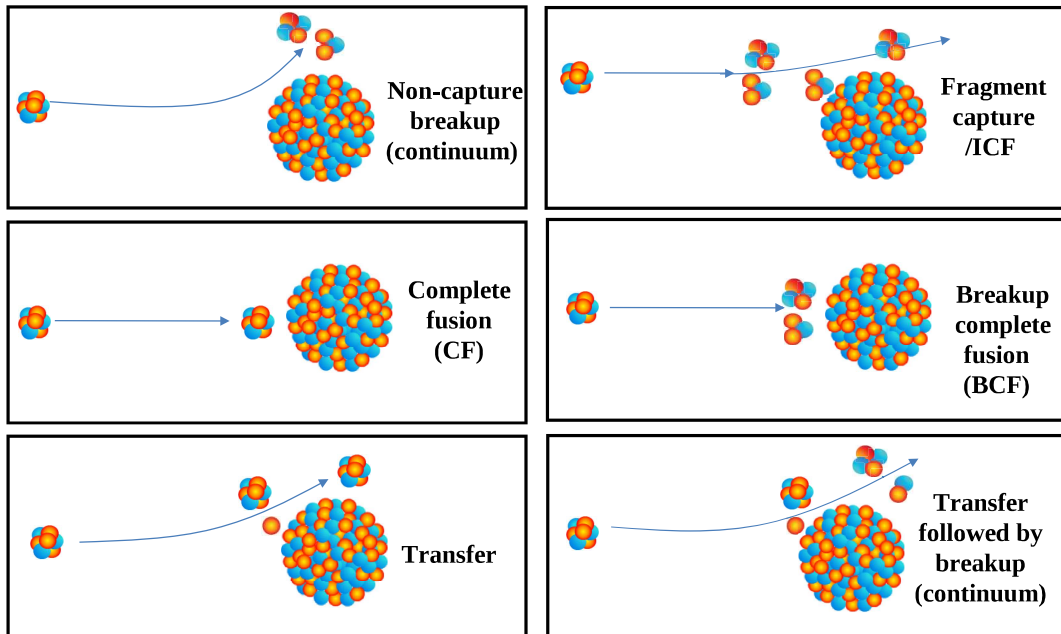


Figure 1.4: Some of the possible dominant reactions induced by low energy weakly bound nuclei.

nucleus is compared with the heavier nuclei in Fig. 1.3(b). The rms matter radius of $^{11}$Li is as large as that of $^{48}$Ca, and the radius of the halo neutrons as large as for the outermost neutrons in $^{208}$Pb [15, 20]. In this context, nuclei having same mass but different charges such as $^{6}$He, $^{6}$Li; $^{11}$Li, $^{11}$Be etc. are the suitable candidates to study the isospin dependence in the nucleon-nucleon interaction [18].
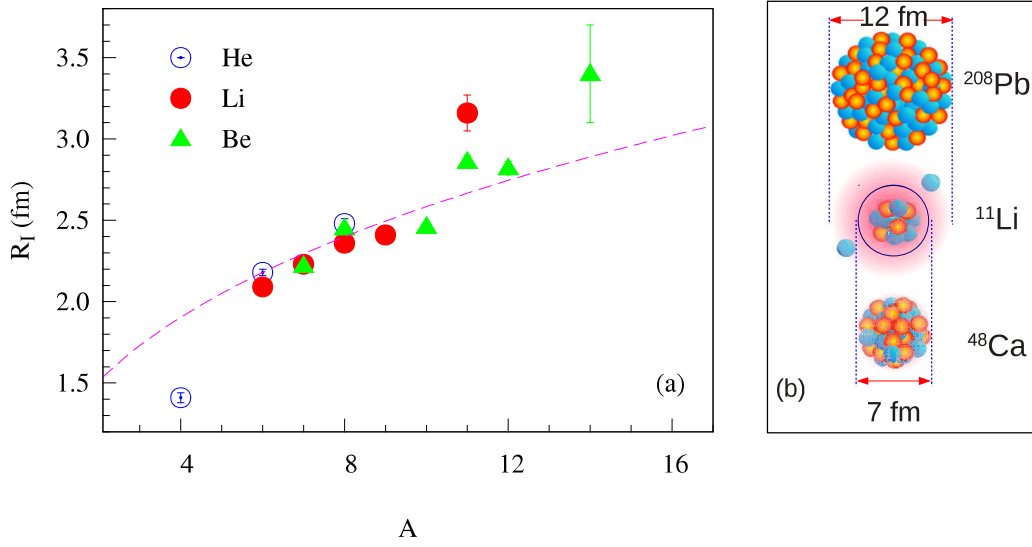


Figure 1.3: (a) Measured interaction radii of He, Li and Be isotopes. The line is corresponding to $R_I = 1.2A^{\frac{1}{3}}$. (b) Comparision of spatial extention of $^{11}$Li nucleus with $^{48}$Ca and $^{208}$Pb nuclei.

## 1.3 Reactions involving weakly bound nuclei

To understand the reaction dynamics of the weakly bound nuclei at energies near the Coulomb barrier, the topics required to be discussed are:

(1) Coupling effects due to the population of the low lying continuum on elsatic scattering and fusion,

(2) Role of cluster structure of the nuclei involved in the reaction,
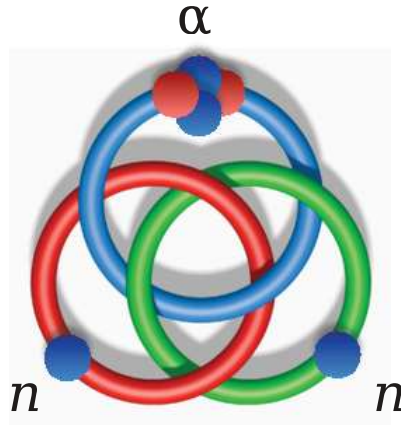
Figure 1.2: Schematic illustration of the $^6$He nucleus with $\alpha + n + n$ Borromean structure.

also display the properties of the Borromean nuclei. The nucleus $^8$He is also known as double Borromean, as its one of the constituent cluster $^6$He is a Borromean nucleus [16]. The nucleus $^8$He, having the highest N/Z ratio, is a suitable candidate to study neutron correlations at low densities [17].

### 1.2.3 Extended matter distribution

The measured charge and matter radii of nuclei are nearly equal for nuclei near the line of stability. Both the radii show $1.2A^{\frac{1}{3}}$ fm dependence. Surprisingly the scenario is not same for some of the weakly bound nuclei. The extracted matter radius of He, Li and Be isotopes from the interaction cross sections are shown in Fig. 1.3(a) [7, 18]. A deviation from $R = 1.2A^{\frac{1}{3}}$ behaviour is clearly observed for $^{11}$Li and $^{14}$Be nuclei [19]. It suggests the existence of a large deformation and/or of a long tail in the matter distribution due to the weakly bound nucleons. A nucleus, having a core surrounded by a "halo" of orbiting protons or neutrons, which makes the radius of the nucleus appreciably larger than the root mean square (rms) radius of the nuclei, is called halo nucleus. For an example, the spatial extension of $^{11}$Li

formation has also been observed.

Some of the weakly bound nuclei e.g. $^{6,8}$He, $^{6,7}$Li, and $^{7,9}$Be have predominant $\alpha$+x cluster structure. The breakup threshold of the predominant cluster structure for these nuclei is tabulated in Table 1.1. In addition to the predominant cluster structure of $\alpha + t$ ($E_{\text{th}} = 2.47$ MeV) the $^7$Li nuclei may also be considered as $^6$He $+ p$, $^6$Li $+ n$, and $^5$He$+d$ cluster configurations with relatively large breakup thresholds of 6.03, 7.25, and 9.52 MeV, respectively [12, 13]. The breakup threshold of $^6$Li is 1.47 MeV and 3.70 MeV for $^6$Li$\rightarrow \alpha + d$ and $^6$Li$\rightarrow \alpha + p + n$ breakup mode, respectively. The $^9$Li isotopes has $^6$He $+ t$ cluster structure [14].

Table 1.1: Breakup threshold of the predominant cluster structure for some of the stable and unstable weakly bound nuclei.

| nuclei | $^6$He | $^6$Li | $^7$Li | $^7$Be | $^9$Be |
|---|---|---|---|---|---|
| Cluster structure | $\alpha + 2n$ | $\alpha + d$ | $\alpha + t$ | $\alpha+^3$He | $^8$Be $+ n$ |
| Breakup threshold $E_{\text{th}}$ (MeV) | 0.98 | 1.47 | 2.47 | 1.59 | 1.66 |

## 1.2.2  Borromean structure

Borromean structure is also an equally interesting phenomenon observed in light weakly bound nuclei [15]. In analogy to Borromean rings, Borromean nuclei consists of three clusters in such a way that if any one is removed, the remaining two become unbound. The lightest Borromean nucleus is $^6$He, which has $\alpha + n + n$ configuration as shown in Fig. 1.2. The possible combination using any two among $\alpha$, $n$ and $n$ are $^5$He($^4$He$+n$) and dineutron ($n + n$) are unstable. The nucleus $^9$Be is the lightest *stable* nuclei with $\alpha + \alpha + n$ Borromean structure. Here $^5$He($\alpha + n$) and $^8$Be($\alpha + \alpha$) are unbound. Similarly, $^{11}$Li ($^9$Li $+n +n$) and $^8$He ($^6$He $+ n + n$)

typical comparison of the energy levels of tightly and weakly bound nuclei is shown in Fig. 1.1. The nucleon separation energy for tightly bound nuclei is ~8 MeV, whereas in case of the weakly bound nuclei breakup threshold is relatively very small (~1 MeV). Now we will discuss some of the special features of the weakly bound nuclei.
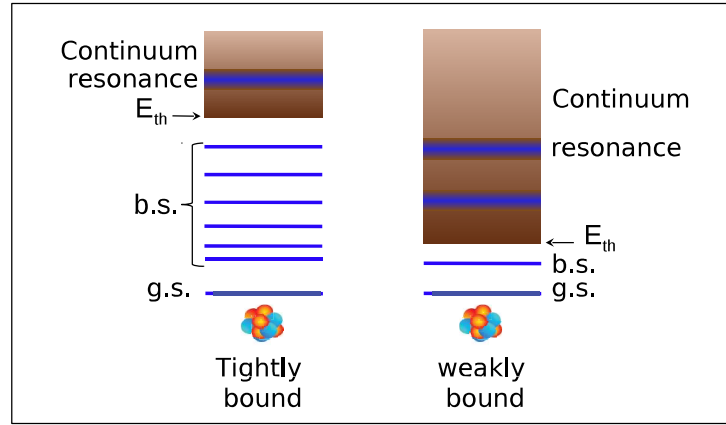


Figure 1.1: A typical comparison of energy levels of tightly and weakly bound nuclei.

## 1.2.1 Cluster structure

Clustering is a general phenomenon that is observed over a wide range of physical scales and in diverse fields such as the aggregation of galaxies in the universe or the existence of gene clusters in complex biological systems [1, 5, 9]. In the nuclear domain, clustering observed in light nuclei elucidates on their structure that leads to a greater understanding of the underlying correlations of nucleons. The $\alpha$-cluster structure has been observed in case of tightly bound stable nuclei e.g. $^{12}$C, $^{16}$O, $^{20}$Ne, $^{24}$Si, etc. [10, 11]. In case of weakly bound stable nuclei, other type of cluster

The conditions of these methods are only suitable with the weakly bound nuclei.

The radioactive ion beam (RIB) facilities provide a scope to study the new features e.g. extended matter distribution in halo nuclei, and the effect of those features on reaction dynamics [3, 5, 6, 7, 8]. The study with RIB is important, as some of the observables which are not visible in case of tightly bound nuclei, may get magnified and provide a more correct description of nucleon-nucleon interaction. In studies related to RIB, special care in experimental methods as well as in theoretical formulations are required. The available RIB facilities are very less in number worldwide and the beam current of such radioactive nuclei is also very low. Hence, it is wise to develop the required measurement techniques by studying the weakly bound stable nuclei, that are easily available with respect to the beam current and energy resolution. The similar kind of physics is expected from weakly bound nuclei due to the low breakup threshold. The measured various observables involving weakly bound nuclei in the context of continuum states, can be used to develop, modify and constrain the theoretical models also.

## 1.2 Weakly bound nuclei

Exploring the properties of weakly bound stable/unstable nuclei is a topic of current interest [3, 4, 5, 6] and also a focus of the next generation of high-intensity isotope-separator on-line (ISOL) radioactive ion beam facilities. Due to the low breakup threshold of such nuclei, population of the states in continuum is probable and consequently a large coupling effect is expected at energies around the Coulomb barrier. The weakly bound stable ($^{6,7}$Li and $^{7,9}$Be) and $\beta$-unstable (e.g. $^{6,8}$He, $^{8-11}$Li, $^{11}$Be etc.) nuclei have exhibited remarkably distinct features with respect to the tightly bound nuclei owing to the low lying continuum states. A

# 1

# Introduction

## 1.1 Preamble

In recent times, the study of reaction dynamics of weakly bound stable nuclei has received much attention due to its implication on research related to exotic nuclei and astrophysics [1, 2, 3, 4, 5, 6]. The understanding of the nucleosynthesis of chemical elements is required to explain the relative elemental abundances of our planetary system [1, 2]. The nucleosynthesis processes in stellar burning astrophysical sites depends on the radiative capture reactions in light nuclei at very low relative energies. However, the measurements of radiative capture cross sections at such low energies under laboratory conditions are very difficult. The difficulties are not only due to the required sensitivity for very low value of cross section measurements, but it is almost impossible to collide two nuclei at such very low relative energies as well. As a consequence, the cross sections of radiative capture processes at energies of astrophysical interest can only be determined from the indirect methods. Those are surrogate method and Trojan Horse Method (THM) [1].

### 2.9.4   Possible uncertainties and their estimation

In case of cross section extraction from the in-beam and off-beam method, the possible sources of uncertainty in addition to those discussed in Sec. 2.8.4 are (a) detection efficiency of $\gamma$-ray and (b) available spectroscopic information of the residues. Both of them have also been included in the uncertainty estimation.

to the normalization constant, the diffuseness of the $J$ distribution, and the value of $J$ at which $\sigma_\gamma(J)$ becomes $a/2$, respectively.

For the odd-even and odd-odd nuclei, due to fragmented transitions, the decay scheme is complicated [59]. In this case, the cross sections have been obtained by adding the $\gamma$-ray transitions, feeding directly to the ground state.

### 2.9.3   Cross section extraction from off-beam measurements

The nuclei, which are not stable and have measurable half life ($T_{1/2}$), were identified by measuring the characteristic $\gamma$-ray transitions employing the off-beam $\gamma$-counting method. The cross sections of each residue have been obtained using the formula

$$\sigma_\gamma = \frac{Y_\gamma \lambda}{N_t \epsilon_\gamma I_\gamma k}, \tag{2.15}$$

where

$$k = \sum_{n=1}^{m} I_n (1 - e^{\lambda t_{step}})(e^{-\lambda[t_1 + (n-1)t_{step}]} - e^{-\lambda[t_2 + (n-1)t_{step}]}), \tag{2.16}$$

In Eq. 2.15, $Y_\gamma$ is the yield of the $\gamma$-line of interest; $\lambda$ is the disintegration constant of the nuclei of interest; $N_t$ is the number of target nuclei/cm$^2$, $\epsilon_\gamma$ is the efficiency of the detector for that $\gamma$-line; $I_\gamma$ is the absolute intensity of that $\gamma$-line; $t_1$ and $t_2$ start and stop times of counting for the irradiated samples; and $t_{step}$ is the step size in which the current was recorded in the scaler. In Eq. 2.16, $I_n$ is the current recorded by the scaler at the n$^{th}$ interval, and m is the total number of intervals of irradiation.
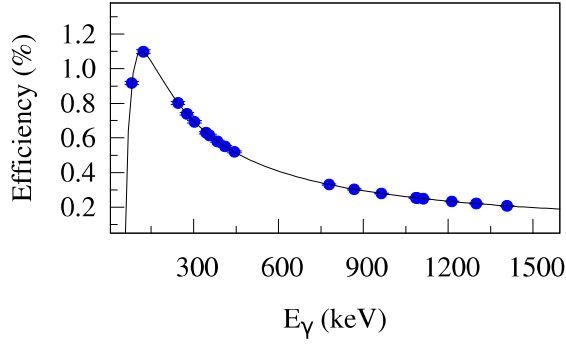
Figure 2.17: The measured efficiency ($\epsilon$) of the HPGe detector for a distance of 10 cm.

The function used to fit the efficiency is $f(x) = a + bE_\gamma + (c/E_\gamma)$. The $\chi^2$ minimized values for $a$, $b$, and $c$ are found to be 0.000415641, 2.43215, and -139.545, respectively.

## 2.9.2 Cross section extraction from in-beam measurements

The cross sections for the even-even residues were extracted from the yrast $\gamma$-ray transitions built on the ground state. Individual cross sections for each $\gamma$-ray transition of the cascade, were extracted using the relation

$$\sigma_\gamma(J) = \frac{Y_\gamma(J)}{Y_M} \frac{d\Omega_M}{\epsilon_\gamma} d\sigma_M, \qquad (2.14)$$

where, $Y_\gamma(J)$ is the yield and $\epsilon_\gamma$ is the absolute efficiency of the $\gamma$-ray transition. $Y_M$ and $d\Omega_M$ are yield and the solid angle of the monitor detector respectively. $d\sigma_M$ is the Rutherford cross section estimated at the angle of the monitor detector ($\theta_M$ = 20°). To extract the cross sections, the $\sigma_\gamma(J)$ values were extrapolated up to the value corresponding to $J = 0$ using the expression, $\sigma_\gamma(J) = a/\{1 + \exp[(J - J_0)/b]\}$, as discussed in references [57, 58]. In this expression $a$, $b$, and $J_0$ correspond
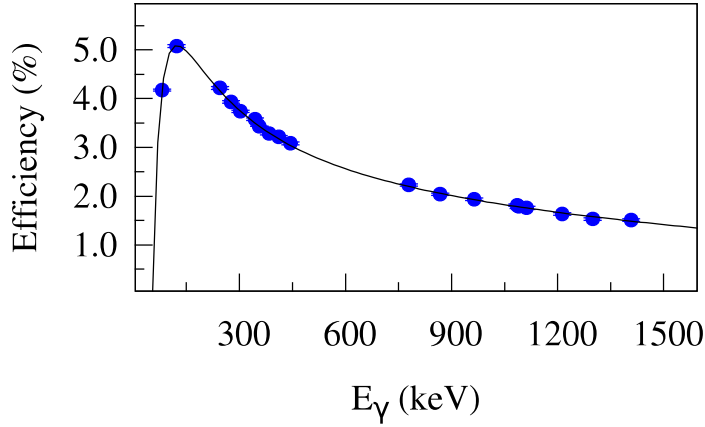
Figure 2.15: The efficiency ($\epsilon$) of the INGA setup having 18 clovers detectors used for in-beam $\gamma$-activity measurements.

having energies in the range 81 keV to 1408 keV and used for in-beam $\gamma$-activity measurements.
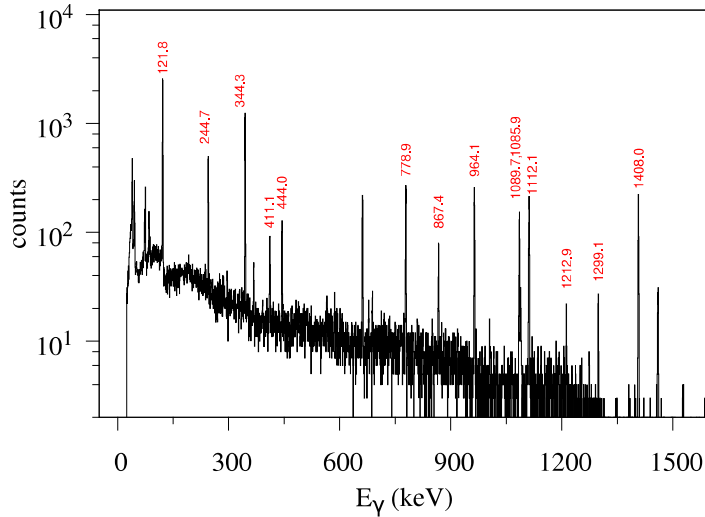


Figure 2.16: The measured $\gamma$-ray spectrum of a calibrated $^{152}$Eu source in HPGe detector.

The efficiency of the HPGe detector, which was used for offline $\gamma$-activity measurements, has been carried out by keeping the calibrated mixed source at distance of 10 cm, 5 cm and on face of the detector. The measured calibrated energy spectrum of $^{152}$Eu source is shown in Fig. 2.16. The energy resolution the HPGe detector was ~1.5 keV for $E_\gamma = 778$ keV and ~ 1.9 keV for $E_\gamma = 1408$ keV. The efficiency values at a distance of 10 cm from the detector are shown in Fig. 2.17.

## 2.9.1   Calibration and efficiency measurements

The efficiency and energy calibration of the Clover detectors and HPGe detector were carried out using standard calibrated $^{152}$Eu and $^{133}$Ba $\gamma$-ray sources. The calibrated energy spectrum of the mixed source measured in INGA setup is shown in Fig. 2.14. The typical energy resolution of a single crystal of a Clover detector was ~1.9 keV for $E_\gamma$ = 778 keV and ~2.3 keV for $E_\gamma$ = 1408 keV.
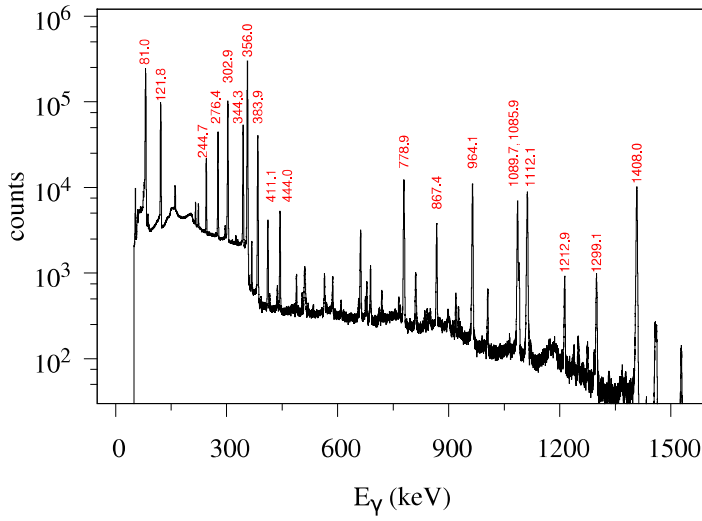
Figure 2.14: A typical add-back $\gamma$-ray spectrum of a calibrated Eu-Ba mixed source from INGA setup.

The total efficiency of INGA setup having 18 Clover detectors is shown in Fig. 2.15 and has been fitted by the function

$$f(x) = a + bE_\gamma + (c/E_\gamma) + (d/E_\gamma^2) + (e/E_\gamma^3), \qquad (2.13)$$

where, a, b, c, d, e are constants. After $\chi^2$ minimization, the constants were found to be a=1.3138, b=-0.000351238, c=988.734, d=-69027.1, and e=638824. The fitted function was used to estimate the efficiency of the setup for the $\gamma$-rays

(b) The uncertainties arise due to the target thickness, beam current fluctuation and the dead time in the acquisition system were eliminated by normalizing the yield by the corresponding yield of the monitor detectors.

(c) Uncertainty in the measurement of beam energy is negligible as the pelletron energies are well calibrated.

(d) Uncertainty due to the loss of the energy in the target.

(e) Uncertainty due to extraction of the yield by fitting the peak area.

(f) Uncertainty in the estimation of the positions and angles of the detectors.

In our results, all these errors were taken into account.

## 2.9 Analysis method to study fragment capture mechanism

In this section, we will discuss the analysis method for both in-beam and off-beam measurements. In case of in-beam measurement, the acquired time-stamped data were first aligned in increasing time format and then any firing in any crystal of the 18 clover detectors or the silicon detectors within the 200 ns time interval were considered as the part of a single event. All the crystals were calibrated using standard calibrated $\gamma$-ray sources and discussed in the next Sec.2.9.1. The gain drift throughout the experiment was checked and corrected. In a single event, if more than one crystal of the same clover detector were fired, those signals were added up to get an add-back spectrum of that detector.

### 2.8.4   Possible uncertainties and their estimation

The estimation of the uncertainty in any measured observable is essential to determine the accuracy of the measurement. There are two types of uncertainty possible in this kind of measurements. Those are discussed below.

1. Statistical uncertainties : The statistical uncertainties arise from random fluctuations in a measurement. These random fluctuations of an experimental setup are directly related to the repeatability of the measurements. Statistical uncertainties are described by the normal distribution. These uncertainties for a large collection of normally distributed measurements can be estimated by calculating the standard deviation $\sigma$. The statistical uncertainty goes as $\sqrt{n}$, where $n$ is the total number of events detected by the detector. In the present cross section measurements three parameters, yields $(Y)$ of the reaction process, corresponding elastically scattered counts in the monitor detector $(Y_m)$, and the detection efficiency estimated by Monte Carlo simulation, contribute to the statistical uncertainty. The contribution from the last one was minimized to negligible relative to the others by running the simulation code for a large number of events. In the estimation of the uncertainties, only the contribution from $Y$ and $Y_m$ are taken into account.

2. Systematic uncertainties :

   (a) Uncertainty involved in measurements of distances from the target and diameters of the collimator lead to uncertainty in the detector solid angle. In our present measurements, the solid angles of all pixels were measured accurately by measuring the elastic scattering from $^{209}$Bi target, details are discussed in the chapter 4.

where, $N_T$ is the target thickness, in terms of number of target nuclei per unit area and $N_P$ is the number of incident nuclei. The elastically scattered yields ($Y_m$) in the monitor detector having the solid angle $d\Omega_m$ is

$$Y_m(\theta_m) = \frac{d\sigma_{\text{Ruth}}}{d\Omega}(\theta_m) \times N_P \times N_T \times d\Omega_m \qquad (2.9)$$

where, $\sigma_{Ruth}$ is the Rutherford cross section. The monitor detector kept at angle $\theta_m$ such that the corresponding elastic cross section will be equal to Rutherford cross section. Using equation 2.8 and 2.9 the relation for the cross section extraction obtained as follows:

$$\frac{d\sigma}{d\Omega}(\theta) = \frac{dY}{d\Omega}(\theta) \times \frac{d\sigma_{\text{Ruth}}}{d\Omega}(\theta_m) \times \frac{d\Omega_m}{Y_m(\theta_m)} \qquad (2.10)$$

$$\frac{d\sigma}{d\Omega}(\theta) = \frac{dY}{d\Omega}(\theta) \times 1.296 \left(\frac{Z_P Z_T}{E}\right)^2 \times \frac{1}{sin^4(\frac{\theta_m}{2})} \times \frac{d\Omega_m}{Y_m(\theta_m)} \qquad (2.11)$$

$$\frac{d\sigma}{d\Omega}(\theta) = \frac{dY}{d\Omega}(\theta) \times \left(\frac{Z_P Z_T}{E}\right)^2 \times \frac{1.296}{Y_m(\theta_m)} \times \frac{1}{K} \qquad (2.12)$$

where, $K = \frac{sin^4(\frac{\theta_m}{2})}{d\Omega_m}$ is a constant of this measurement setup. The value of $K$ was obtained from the elastic scattering cross section measurements for $^7$Li+$^{209}$Bi system as discussed in chapter 4 and found to be 25.3. The relation is given in Eq. 2.12 for the extraction of the cross section, automatically remove the uncertainty arises due to beam currents, target thickness, energy loss in target thickness and dead time in the data acquisition modules.

$$Q = E_{\text{K.E.}}(1 + \frac{m_3}{m_4}) - E_{\text{lab}}(1 - \frac{m_1}{m_4}) - \frac{2}{m_4}(m_1 E_{\text{lab}} m_3 E_3)^{1/2} cos(\theta_3), \qquad (2.5)$$

where, $m_3$ is the mass of the ejectile ($m_3 = m_1 + m_2$) prior to breakup, $m_4$ is the mass of the target like nuclei, $E_{\text{lab}}$ is the energy of the incident projectile, and $\theta_3$ is the scattering angle of the ejectile prior to breakup. The excitation energy of the target like nuclei were determined from the relation

$$E^*_{\text{target}} = Q_{\text{gg}} - E^*_{\text{ejectile}} - Q, \qquad (2.6)$$

### 2.8.3 Extraction of cross section

The yields ($Y$) of reaction products for a selected channel were obtained as a function of c.m. angle ($\theta_{c.m.}$), considering event-by-event mode of analysis as shown in Fig. 2.12. The detection efficiency (solid angle) of that corresponding reaction channel was estimated as a function of $\theta_{c.m.}$ using a Monte Carlo technique of three body kinematics. The angular distribution of the events related to that particular reaction was extracted by taking the ratio of these two quantities as

$$\frac{dY}{d\Omega}(\theta) = \frac{dY}{d\theta} / \frac{d\Omega}{d\theta} \qquad (2.7)$$

The cross section of the corresponding reaction channels were obtained as

$$\frac{d\sigma}{d\Omega}(\theta) = \frac{dY}{d\Omega}(\theta) \times \frac{1}{N_P \times N_T} \qquad (2.8)$$
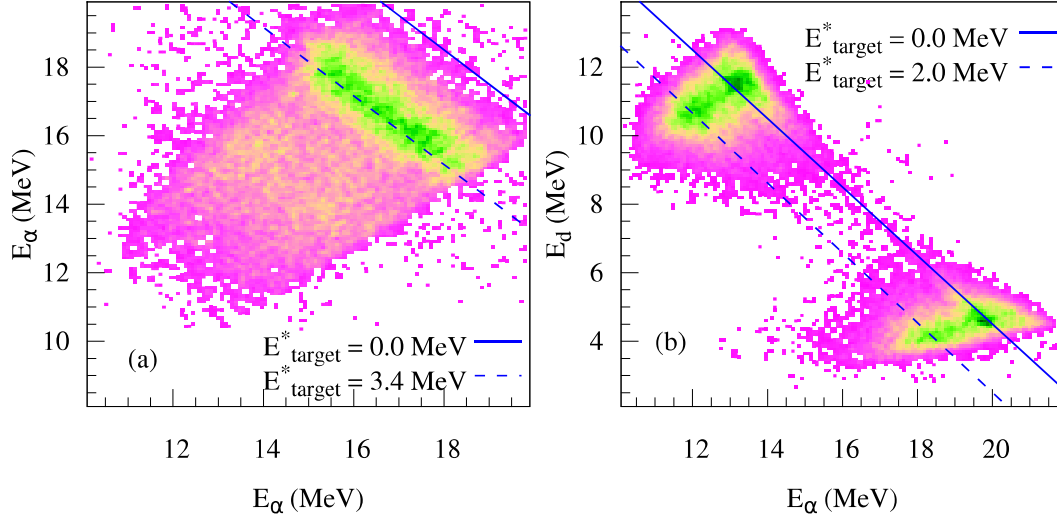
Figure 2.13: Measured energy correlation spectra of breakup fragments in coincidence for $^7$Li + $^{89}$Y reaction at $E_{\mathrm{lab}}$ = 27.7 MeV and $\theta_{\mathrm{lab}}$ = 60°. (a) $1p$-pickup followed by breakup of $^8$Be leading to two $\alpha$-particles. (b) $1n$-stripping followed by breakup of $^6$Li leading to $\alpha$ and $d$-particles.

$$E_{\mathrm{K.E.}} = E_1 + E_2 - E_{\mathrm{rel}}, \tag{2.3}$$

$$E^*_{\mathrm{ejectile}} = E_{\mathrm{rel}} + E_{\mathrm{th}}, \tag{2.4}$$

The excitation energy ($E^*_{\mathrm{ejectile}}$) of the ejectile prior to breakup was obtained by adding the breakup threshold to the measured $E_{\mathrm{rel}}$. The $^8$Be nuclei is particle unbound and breaks into two $\alpha$ particles from its ground state itself. Where as the breakup threshold ($E_{\mathrm{th}}$) of $^6$Li→ $\alpha + d$ and $^7$Li→ $\alpha + t$ are 1.47 and 2.47 MeV, respectively. The reaction Q-value calculated using the relation

other side of the detector. Taking care of those events is suppose to improve the statistics but could lead to more uncertainties in terms of spurious coincidences. We have rejected those events and same was taken care in the simulation to extract absolute cross sections. The spurious coincidences may also occur due to (i) random coincidences of true events with detector noise or an elastically scattered event, (ii) cross-talk across adjacent sectors, and (iii) charge sharing of a scattered projectile that hit the inter-strip partition. Contributions to the source (i) were removed by applying cuts in the singles energy spectrum as well as 2-dimensional gate in energy-energy correlation spectra. Sources (ii) and (iii) can only originate from coincidences within a single detector, and to remove them always correlated events detected in adjacent strips were rejected.

In the Fig. 2.13, the measured correlation spectra of the energies of the $\alpha$-$\alpha$ and $\alpha$-$d$ coincidence events for the $^7$Li + $^{89}$Y reaction at $E_{\text{lab}}$ = 27.7 MeV and $\theta_{\text{lab}}$ = 60° is presented.

The relative angles ($\theta_{\text{rel}}$) between the fragments were calculated from the measured scattering angles ($\theta_1$, $\phi_1$; $\theta_2$, $\phi_2$) using the relation

$$\theta_{\text{rel}} = cos(\theta_1)cos(\theta_2) + sin(\theta_1)sin(\theta_2)cos(\phi_1 - \phi_2), \tag{2.1}$$

The relative energy ($E_{\text{rel}}$) between the fragments was calculated from their masses ($m_1, m_2$), kinetic energies ($E_1, E_2$) and $\theta_{\text{rel}}$ using the relation

$$E_{\text{rel}} = \frac{m_2 E_1 + m_1 E_2 - 2(m_1 E_1 m_2 E_2)^{1/2} cos(\theta_{\text{rel}})}{m_1 + m_2}, \tag{2.2}$$

The kinetic energy $E_{\text{K.E.}}$ and the excitation energy $E^*_{\text{ejectile}}$ of the ejectile prior to breakup were calculated using the following relations
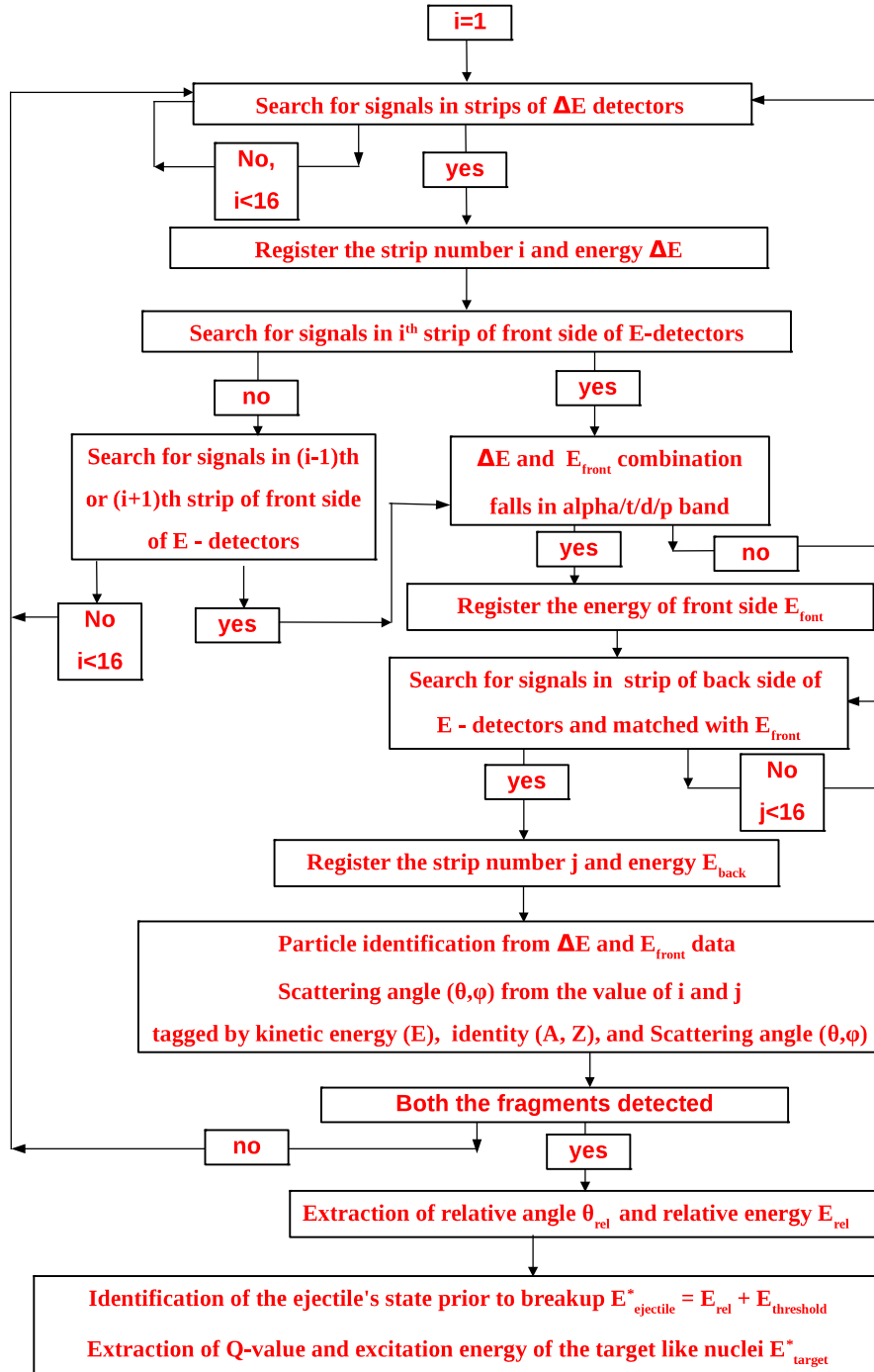
Figure 2.12: The flow chart for the analysis using event by event method.

## 2.8.1 Energy calibration

In order to get the accurate energy information of the reaction products, the energy signals of $\Delta E$ and $E$ detectors are first gain matched and added to get $E_{total}$. All the strips of both $\Delta E$ and $E$ detectors are calibrated using the known $\alpha$ energies from a $^{239}$Pu-$^{241}$Am-source and the $^7$Li + $^{12}$C reaction. A typical $\Delta E$ vs. $E_{total}$ plot for $^7$Li + $^{12}$C reaction carried out using 18 MeV $^7$Li beam is shown in Fig. 2.11(a). The projection of the $\alpha$-band of the figure is shown in Fig. 2.11(b). The identified various discrete states of $^{15}$N* are labeled, which are used for the calibration. This leads to a calibration of the $\alpha$-particles for an energy range of 5-22 MeV. The calibrated energies have been used for further analysis.

## 2.8.2 Identification of reaction channels

A flow chart for analyzing the coincidence data on an event by event basis, to identify various reaction channels is given in Fig.2.12. The scattering angle ($\theta$, $\phi$) of the detected fragment was extracted from the vertical and horizontal strip numbers of the double-sided $E$ detector. Detected particles were tagged by kinetic energy ($E$), mass number ($m$) and scattering angle ($\theta$, $\phi$). The energy and scattering angle were converted from laboratory frame to the c.m. frame of the target-projectile in event-by-event mode. By this method of analysis, the Jacobian of the transformation was taken care automatically. The pairs of particles observed in the coincident events were $\alpha$-$\alpha$, $\alpha$-$d$ and $\alpha$-$t$. The $\alpha$-$\alpha$ event rate was found to be highest and that for $\alpha$-$t$ was lowest. Identification became complicated only when the coincident pair hit the same strip of a given detector. These events could have been recovered by matching their energy to the sum of signals measured on the

the essential part of the measurements. The accurate distances of the detectors from the centre of the target have been measured from the angle information of the centre, left and right edges of the detectors obtained using a theodolite and rotating the arm, on which they were mounted. The exact distance and the dimension of the detectors were used to get the exact angles of the pixels. The method of energy calibration is discussed in the next subsection 2.8.1.
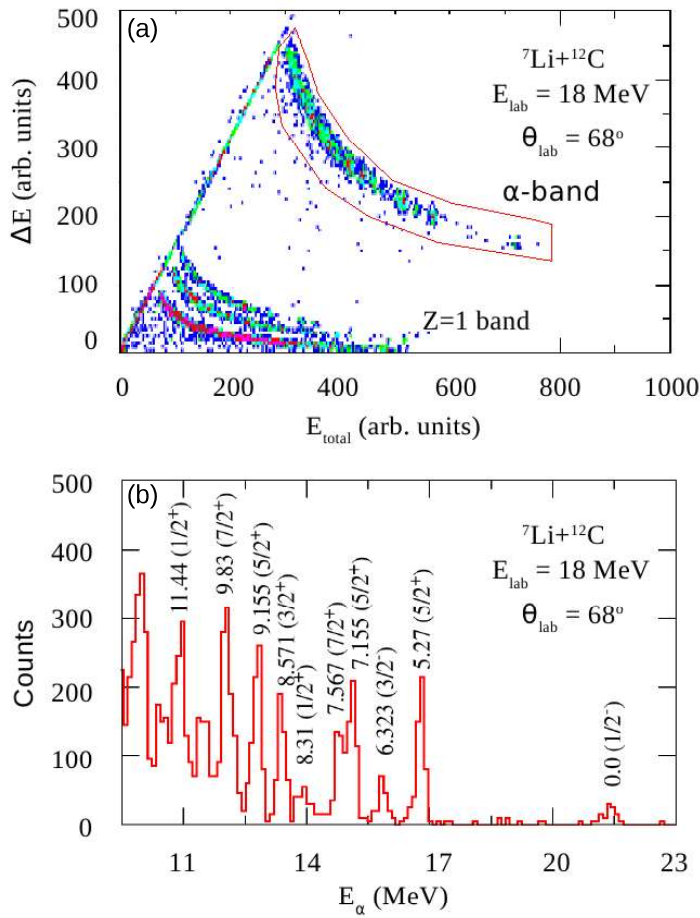


Figure 2.11: (a) A typical gain matched two dimensional $\Delta E$ vs. $E_{total}$ plot for $^7$Li + $^{12}$C reaction at 18 MeV, showing the different reaction products of Z = 1 and 2. (b) The projected energy spectra of the $\alpha$-band of (a).

time stamp will be latched and the event header information will be written. All the modules are required to synchronize clocks for the coincidence measurement.

## 2.8 Analysis method for breakup fragments in coincidence

Particles were identified using energy loss information from $\Delta E$ and $E$ detectors. A typical two dimensional spectrum of $\Delta E$ vs $E_{\text{tot}}$ for $^7$Li on $^{93}$Nb at beam energy $E_{beam}$=28 MeV and $\theta_{\text{lab}} = 60°$ is shown in Fig. 2.10. A good charge and mass resolution has been achieved which allowed the separation of all the isotopes of Z = 1, 2, and 3 nuclei.
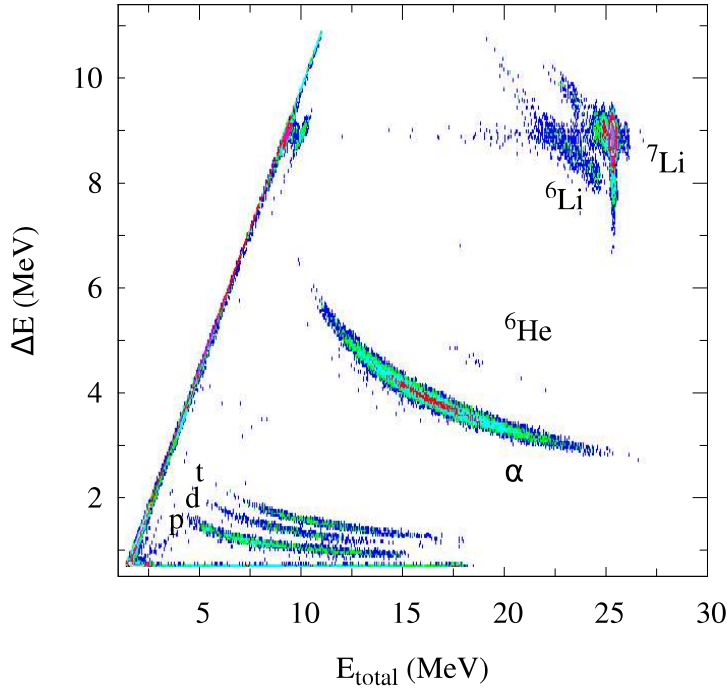


Figure 2.10: A typical two dimensional spectrum of $\Delta E$ vs $E_{\text{tot}}$ for $^7$Li on $^{93}$Nb at beam energy $E_{beam}$=28 MeV and $\theta_{\text{lab}} = 60°$.

To extract the accurate information, the energy and the angle calibration are
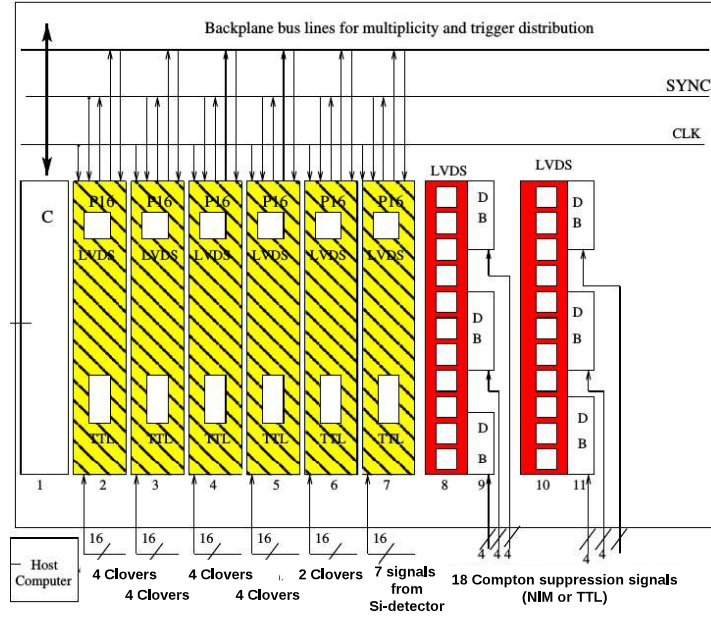
Figure 2.9: Block diagram for the digital DAQ for 16 Compton suppressed clover detectors, 3 telescope consists of Si $\Delta E$ and $E$ detectors, and one single Si detector. It has six Pixie-16 modules, two LVDS level translator modules and one controller arranged in a single compactPCI/PXI crate.

a trigger through a fast filter for total multiplicity computation in the on board FPGA. The fast trigger is generated when the fast trapezoid filter output crosses the defined threshold. The fast triggers generated from any of the 16 channels of a Pixie-16 module can be distributed to its adjacent modules through the PXI back plane for generation of global trigger. In the present configuration, of the six cards in a single crate one card named as Director receives and distributes the triggers among all the channels. The Director computes the multiplicity and opens the coincidence window with a defined length. The veto signal of the BGO shield is given via the front panel LVDS I/O port. A valid fast trigger is generated in absence of the veto pulse in a specific time window. For a given channel the fast trigger validated by the external trigger and not vetoed by channel veto signal, the

## 2.7   Electronics and data acquisition for the measurements of particle-$\gamma$ in coincidence

The signals from each crystal of the clover detectors were amplified by a low temperature FET coupled with the resistive charge sensitive preamplifier. The preamplifier has a gain of 200 mV/MeV and the decay time constant of the output is 50 ms. The Compton suppressed BGO shield has 16 photo multiplier and operates at 950 V. A NIM logic signal was generated by amplifying the sum of the 16 photo multipliers using a timing filter amplifier and a analog constant fraction module. This logic signal was used as veto to the signals from the clover detectors. The signals from silicon detectors were amplified by a low noise preamlifier. All the amplified signals of clover and Si detectors using respective preamplifier were acquired. PCI-PXI based digital data acquisition (DDAQ) system was used to acquire the data. The DDAQ consists of six Pixie-16 modules, two LVDS level translator modules, and one controller arranged in a single compact PCI/PXI crate. The crate is connected to a windows PC via a MXI-4 PXI-PCI optical bridge. Each Pixie-16 card has 16 channels. The block diagram of the system is shown in Fig. 2.7. Elaborate technical information about digitizer Pixie-16 modules can be found in Ref. [56].

Only, the complex triggering capability of the Pixie-16 modules adopted for the present experimental set-up will be briefly described in the following. The clover produces four signals from the core of the four crystals. Therefore, each Pixie-16 card supports four clover detectors. The preamplifier signal is digitized with a 12-bit 100 MHz Flash Analog to Digital Converter (FADC). The digitized data stream of the incoming analog pulse enters the signal processing circuitry. This generates
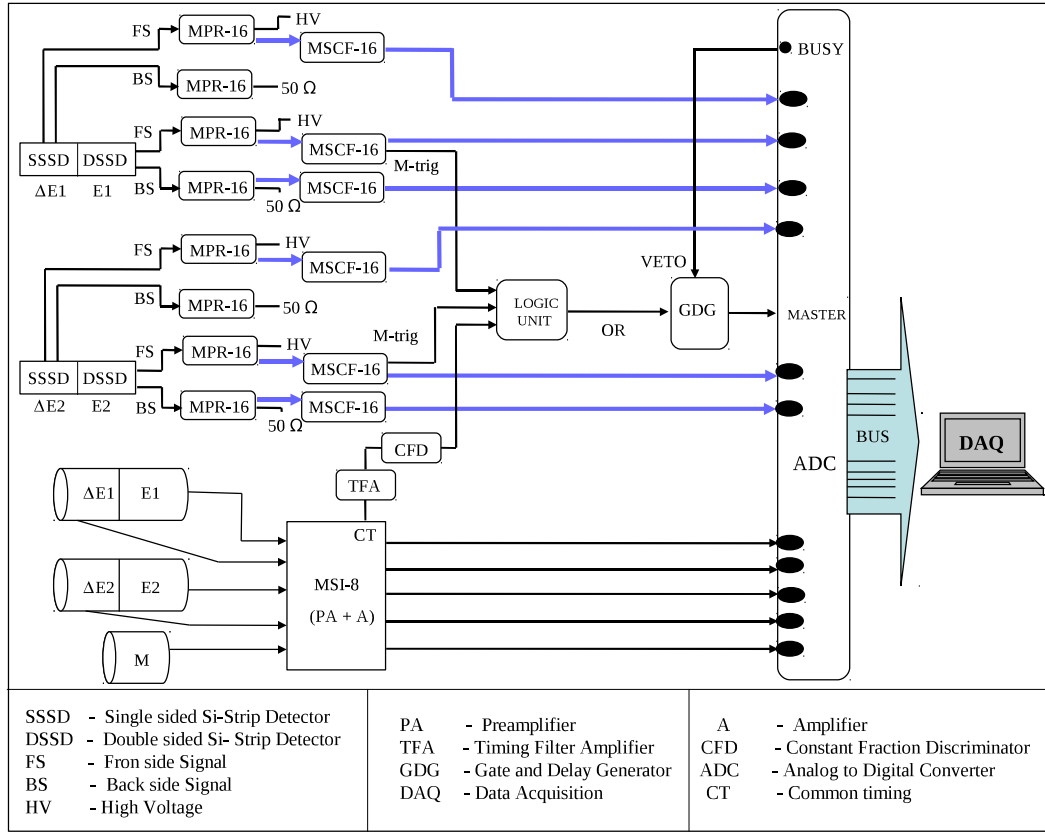
Figure 2.8: Electronics block diagram for the measurements of breakup fragments in coincidence.

The width of the busy signals was kept 6-12 $\mu$s, depending on count rates. Data acquisition is based on VME standard cards, manufactured by Caen SpA, peak-sensing analog-to-digital converters (mod. V785), time-digital- converters (mod. V778) and digital counters/latching-scalers (mod. V830). All these cards are daisy-chained connected and fired simultaneously by the actual master. This trigger is also used for starting the analog-to-digital conversion, the time-to-digital conversion process, and the general system data readout.

Gmbh & Co. KG. These compact modules are having 16 channels, specially designed and suitable for segmented silicon detectors. Signals from detectors were taken outside the chamber using suitable detector adapters, vacuum cables and vacuum feedthrough of socket-socket type. These signals were fed to the MPR-16, sixteen channel preamplifier. The output signals from MPR-16 modules are differential. The advantage of the differential signal is that by further processing, the noise can be reduced. The output signals from MPR-16 module were processed by MSCF-16 amplifier. MSCF-16 is a shaping / timing filter amplifier with constant fraction discriminator and multiplicity trigger. The shaper output signal that contain the energy information, were digitized by CAEN-v785 peak sensing analog to digital converters (ADC). The multiplicity trigger signals were used to make the master gate as discussed in the next paragraph. The signals from silicon surface barrier detectors have been processed using the MSI-8 module, which is a compact 8-channel preamplifier shaper box with integrated timing filter amplifiers. This module gives preamplifier as well shaper outputs. The shaper outputs were digitized. The common timing signal was used to generate the master gate.

The block diagram of the electronic setup is shown in Fig. 2.8. The multiplicity trigger output from MSCF-16 module, corresponding to the front side of the $E$-detectors, was used to make the master gate. The value of lower multiplicity threshold was kept one and two for singles and coincidence measurements, respectively. While the value of upper multiplicity threshold was set to infinite. The OR of these multiplicity trigger output and the common timing signals from MSI-8 module were stretched to 6 $\mu$s by using gate and delay generator module. This signal is specified as raw-master. The busy signals from ADCs were stretched and used to VETO the raw-master to generate actual master.

ments with regard to purity, composition, thickness etc. Many techniques are used for target preparation. These include (a) chemical techniques: Electro-deposition, electrophoresis, vapour deposition, electrical discharge, electro-polishing etc. (b) Mechanical techniques: compacting, rolling, settling of powders from suspension. (c) Physical techniques: Direct deposition using an isotope separator, electrospraying, sputtering and high vacuum deposition.

For our experimental measurements, we have used four targets $^{89}$Y, $^{93}$Nb, $^{12}$C, and $^{209}$Bi which were made in the following ways:-

1. The target of $^{89}$Y and $^{93}$Nb were made by rolling technique using respective natural metallic foils. The thickness of $\sim$ 2.0 mg/cm$^2$ of $^{89}$Y and $\sim$ 1.75 mg/cm$^2$ of $^{93}$Nb were used in experiment.

2. The target of $^{12}$C having thickness of $\sim$ 50 $\mu$g/cm$^2$ was prepared by the carbon arc method.

3. The target of $^{209}$Bi was made by vacuum deposition (evaporation) technique. The thickness of $\sim$ 500 $\mu$g/cm$^2$ of $^{209}$Bi was monitored by the quartz crystal.

These targets were then mounted on the target ladder of scattering chamber.

## 2.6 Electronics and data acquisition for measurements of breakup fragments in coincidence

The processing of the signals from the segmented Si-detectors was carried out by MPR-16 multichannel preamplifier and MSCF-16F shaping-timing filter amplifier modules. Both MPR-16 and MSCF-16 modules are manufactured by Mesytec

5% at $E_\gamma = 1$ MeV. INGA at Mumbai, is having a PCI-PXI based digital data acquisition (DDAQ) system.

### 2.4.3  High purity germanium detector (HPGe)

A high-purity germanium (HPGe) detector with a graded shielding (Cu, Cd sheets of thickness $\sim 2$ mm followed by 5 cm Pb) shown in Fig. 2.7 was used for the off-beam $\gamma$-ray measurements. The energy resolution of the HPGe detector was $\sim$ 1.5 keV for $E_\gamma = 778$ keV and $\sim 1.9$ keV for $E_\gamma = 1408$ keV.
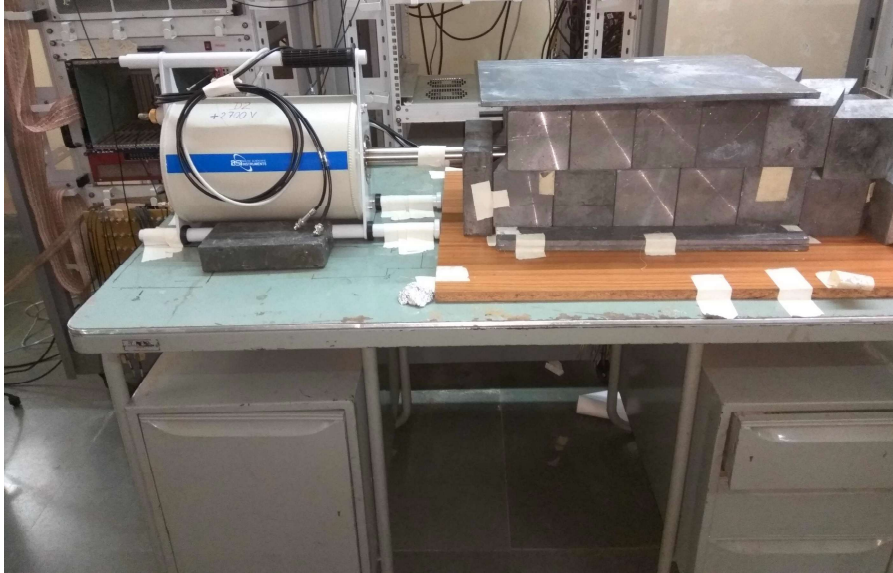


Figure 2.7: Low background off beam $\gamma$-ray counting setup with the shielded HPGe detector.

## 2.5  Target preparation

Target preparation is often crucial to the success of an experiment and it is therefore of the utmost importance that the target confirms to the experimental require-
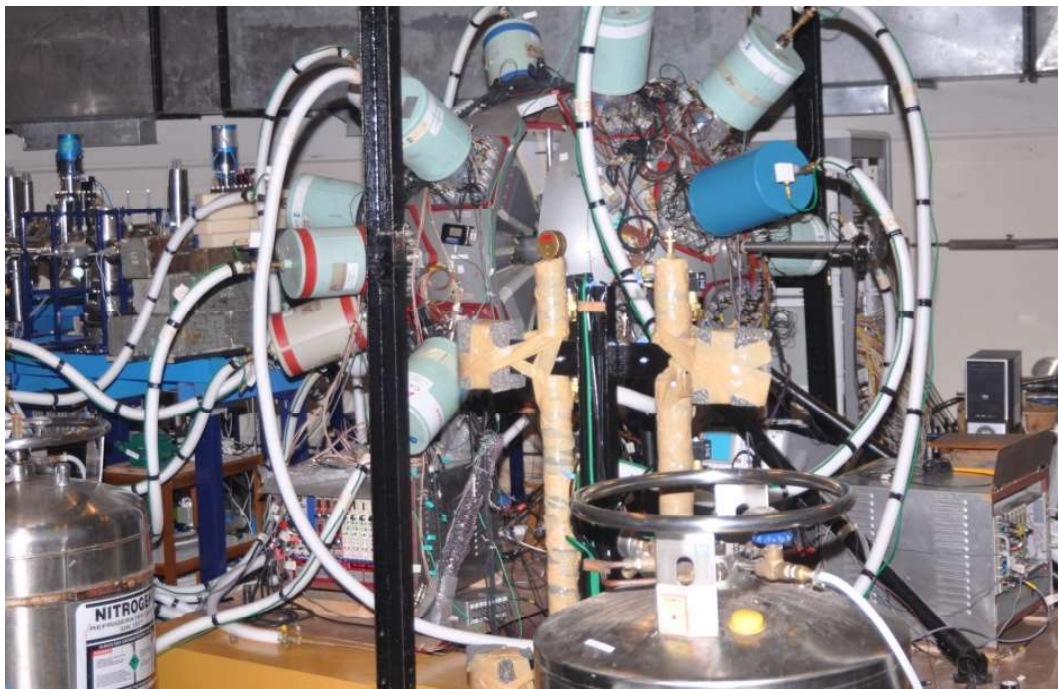
Figure 2.6: Indian National Gamma Array, consists of 18 clover detectors.

Centre, UGC-DAE-Consortium for Scientific Research, and many Universities in India [56]. INGA consists of a large number of Compton suppressed clover detectors. Each of the clovers consists of four n-type high purity germanium (HPGe) crystals kept in a single cryostat. Each crystal is connected to a low-temperature FET coupled with the resistive charge sensitive preamplifier. The sum of the 16 photo multipliers is given to a timing filtering amplifier and then to the analog constant fraction module which generates a NIM logic signal. This goes as an input to the digital data acquisition system for the veto of the clover signals. The detector array is designed for 24 Compton suppressed clover detectors arranged in a spherical geometry with six detectors at 90$^o$ and three detectors each at 23°, 40°, 65°, 115°, 140° and 157° with respect to the beam direction. The distance from the target to crystal is 25 cm and the overall photo peak efficiency is around
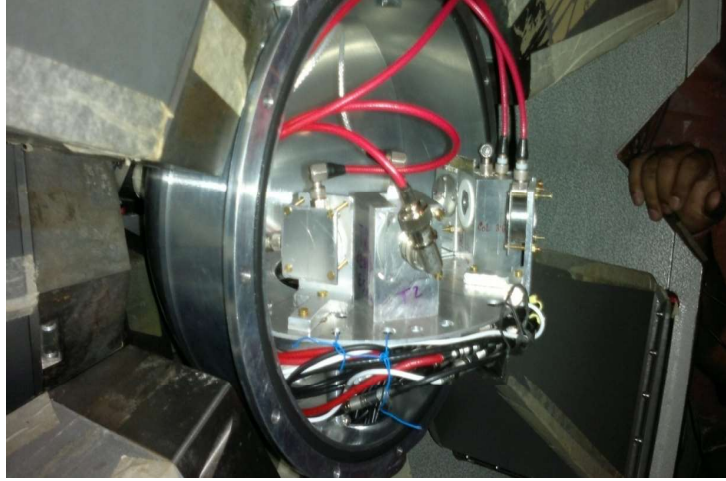
Figure 2.5: Schematic diagram of the scattering chamber used for fragment capture measurements. Three Si surface barrier telescopes (thicknesses $\Delta E \sim$ 15-30 $\mu$m, $E \sim$ 300-5000 $\mu$m), were kept inside the scattering chamber at 35°, 45° and 70° for the detection of charged particles. One Si surface-barrier detector (thickness $\sim$ 300 $\mu$m) was kept at 20° to monitor beam current for absolute normalization.

intersecting areas of both side's segments form pixels. Single sided detectors are having segments only in the junction side. Signals from individual strips were collected using multichannel preamplifier. These detectors are used to obtain position and energy-loss informations. Particles are identified using energy loss information from $\Delta E$ and $E$ detectors of the telescopes. The typical energy resolution of individual strips are $\sim$70 keV for the measurements of $\alpha$-particles from a $^{239}$Pu-$^{241}$Am-source. Si-surface-barrier detectors have also been used in the experimental setup.

## 2.4.2   Indian National Gamma Array

Indian National Gamma Array (INGA) is a collaborative research facility of Bhabha Atomic Research Centre, Tata Institute of Fundamental Research, Inter University Accelerator Center, Saha Institute of Nuclear Physics, Variable Energy Cyclotron
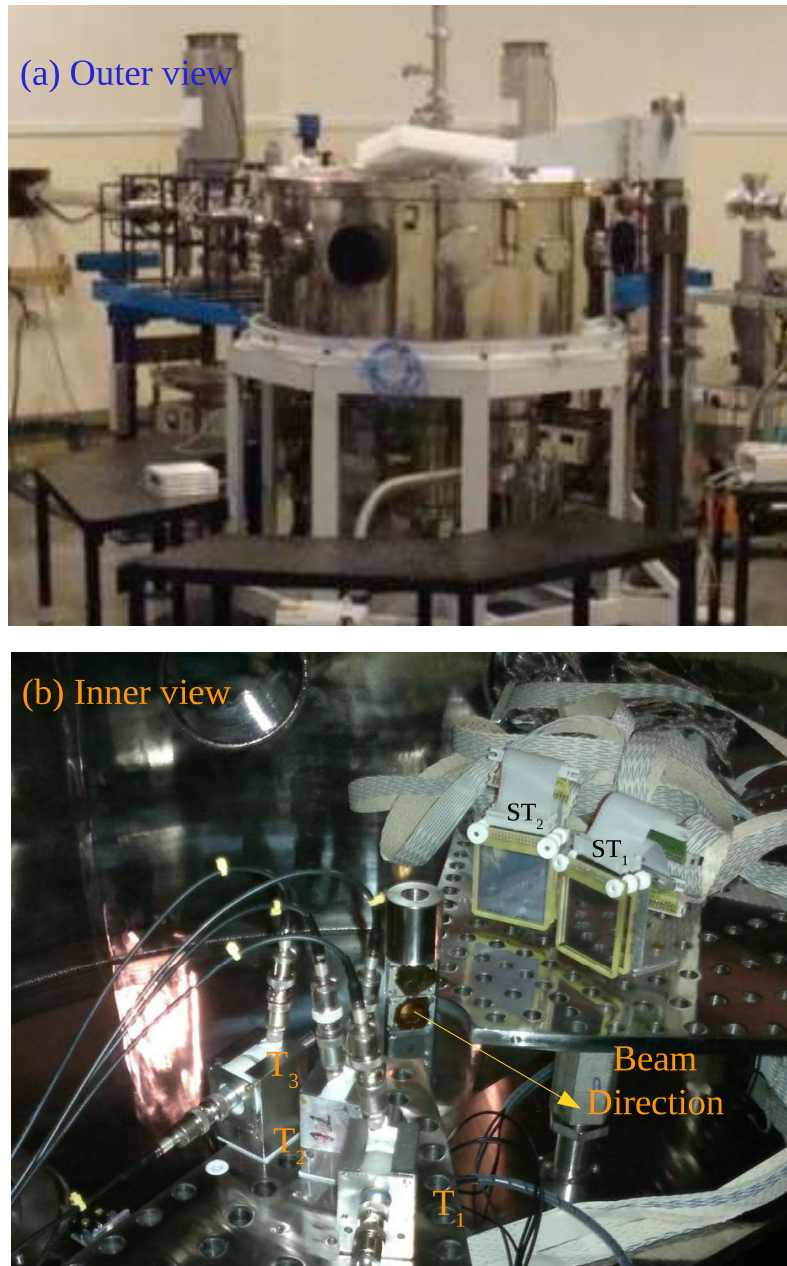
Figure 2.4: Schematic diagram of the 1.5 m diameter scattering chamber used for the measurements of the breakup fragments in coincidence. (a) Outer view of the chamber. (b) the inner view of chamber: two telescope consists of Si-strip detectors, three telescopes consists of Si-surface barrier detectors, and target ladder.

cation without interrupting beam using ferrofluidic seals and PLC (Programmable Logic Controller) are available. The schematic diagram of scattering chamber is shown in Fig. 2.4.

The fragment capture measurements have been carried out in a scattering chamber of diameter 24 cm. This chamber was designed very compact and made of aluminum alloy, to reduce attenuation of the $\gamma$-ray flux. This chamber contains the charged particle detectors and a target assembly. Before its entry into the scattering chamber, the beam was defined by two square collimators of 3 x 3 and 2 x 2 mm$^2$, respectively, separated by a distance of 1 meter. The target was located 1.9 meter downstream from the last collimator. A schematic illustration of the experimental setup is shown in Fig. 2.5.

## 2.4    Detection setup

The details of the detection techniques for the charged particles and gamma-rays are discussed in the following sections.

### 2.4.1    Silicon strip detector telescope

The requirements of high granularity to detect low-lying resonant states and large solid angle to measure low cross section events have been achieved using segmented large area Si-telescopes of active area $5 \times 5$ cm$^2$. Silicon strip detectors are widely used for charged particle detection in nuclear and particle physics experiments. They are constructed as large area silicon detectors with segmented p-side and n-side contacts. Both single sided and double sided detectors are available. In case of double sided detectors, both junction and Ohmic sides are segmented. The

and are therefore accelerated to the ground potential. This results in an energy gain of qV$_T$ MeV for an ion with charge q. Thus, the total energy gain of the ions becomes $E = (q + 1)V_T$ MeV. At the end of the accelerating tube, an analyzing magnet is placed which serves the purpose of charge and energy selection of the ions. The energy of the analyzed ions of mass number $A$ and charge state $q$ in this accelerator is given by the relation $B = 720.76\frac{\sqrt{AE}}{q}$. Where $B$ is the magnetic field in Gauss and $E$ is the energy in MeV. This analyzed beam of ions is then transported to the experimental setup with the help of switching magnet. There are five beam lines 0°, 15°N, 15°S, 30°N, and 30°S in the Pelletron beam hall, three beam lines 15°, 30°, and 45° in LINAC Hall-1, and three beam lines 15°, 30°, and 45° in LINAC Hall-2. The pictures of Linac Beam Halls are shown in Fig. 2.3.

The breakup and transfer-breakup reaction measurements have been carried out at 30° beam line in LINAC Hall-1 using a 1.5 general purpose scattering chamber. The measurements of fragment-capture reactions were performed at 15° beam line in LINAC Hall-2 using the Indian National Gamma Array setup. For off-beam $\gamma$-activity measurement, targets were irradiated in a small chamber situated at 30°N beam line in the Pelletron beam hall.

## 2.3   Scattering chamber

The exclusive measurements, to detect the breakup fragments in coincidence, have been carried out in a 1.5 meter diameter general purpose scattering chamber. The scattering chamber has been installed in 30$^o$ beam line of LINAC Hall-1. This chamber has two independently rotatable arms to mount detectors and a target ladder with the provision to mount 6 targets. Facility of rotation of the detectors arms and rotation as well as height adjustment of target ladder from a remote lo-

**LINAC Beam Hall-1**



**LINAC Beam Hall-2**
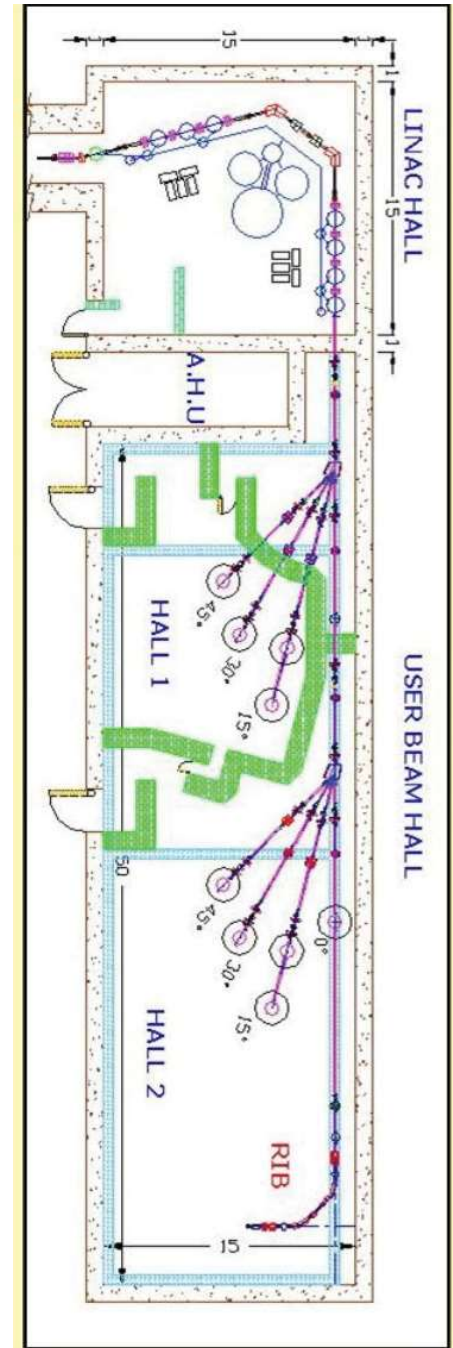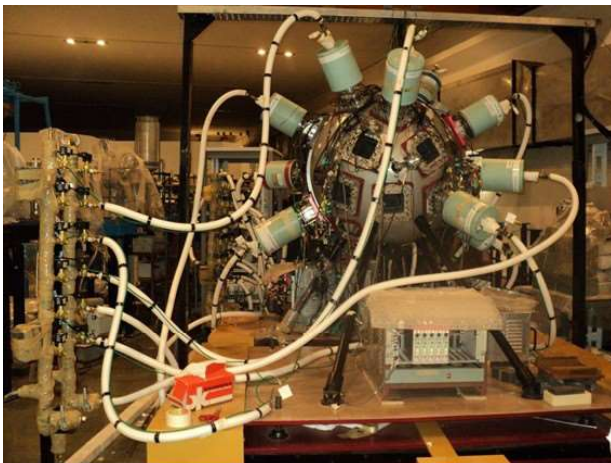




Figure 2.3: A schematic layout of Mumbai Pelletron Linac Facility.

used for the basic research in the fields of nuclear, atomic and condensed matter physics as well as accelerator based applications. The main purpose of the LINAC is to boost the energy of the heavy ion beams so that the scope of research in nuclear physics can be extended to heavier projectile which is unexplored by the Pelletron energy. Fig. 2.2 shows the schematic layout of the Mumbai Pelletron Linac facility (PLF). PLF has a 14 UD Pelletron tandem accelerator procured from NEC, USA [53] and an indigenously developed superconducting linear accelerator (LINAC) [54, 55] based on lead plated copper quarter wave resonators. The source of negative ions from cesium sputtering 'SNICS' situated at the top of the accelerator tower generates negative ions, which are initially accelerated to low energies (150-250 keV) in a short horizontal section. These low energy negative ions are then mass analyzed using a 90° magnet (injector magnet) before entry into the vertical accelerator column. These injected ions get accelerated towards the positively charged high voltage terminal situated in the middle. Due to this acceleration, negative ions gain an energy of $V_T$ MeV, where $V_T$ is the terminal voltage in MV (million volts). For the present accelerator, the maximum terminal voltage is 14 MV. This high electric potential at the terminal is achieved by means of the chain of steel pellets separated by insulators and hence the name **pelletron accelerator**. This method leads to more uniform charging compared to moving charging belt and hence less ripple on the HV terminal. Inside the terminal, the ions pass through a thin carbon foil ($\sim 5 \ \mu g/cm^2$) or a small volume of a gas, where they lose several electrons resulting in a distribution of positively charged ions.

This distribution depends on the type and velocity of the ions. These positively charged ions at the terminal are repelled by the positive voltage at the terminal
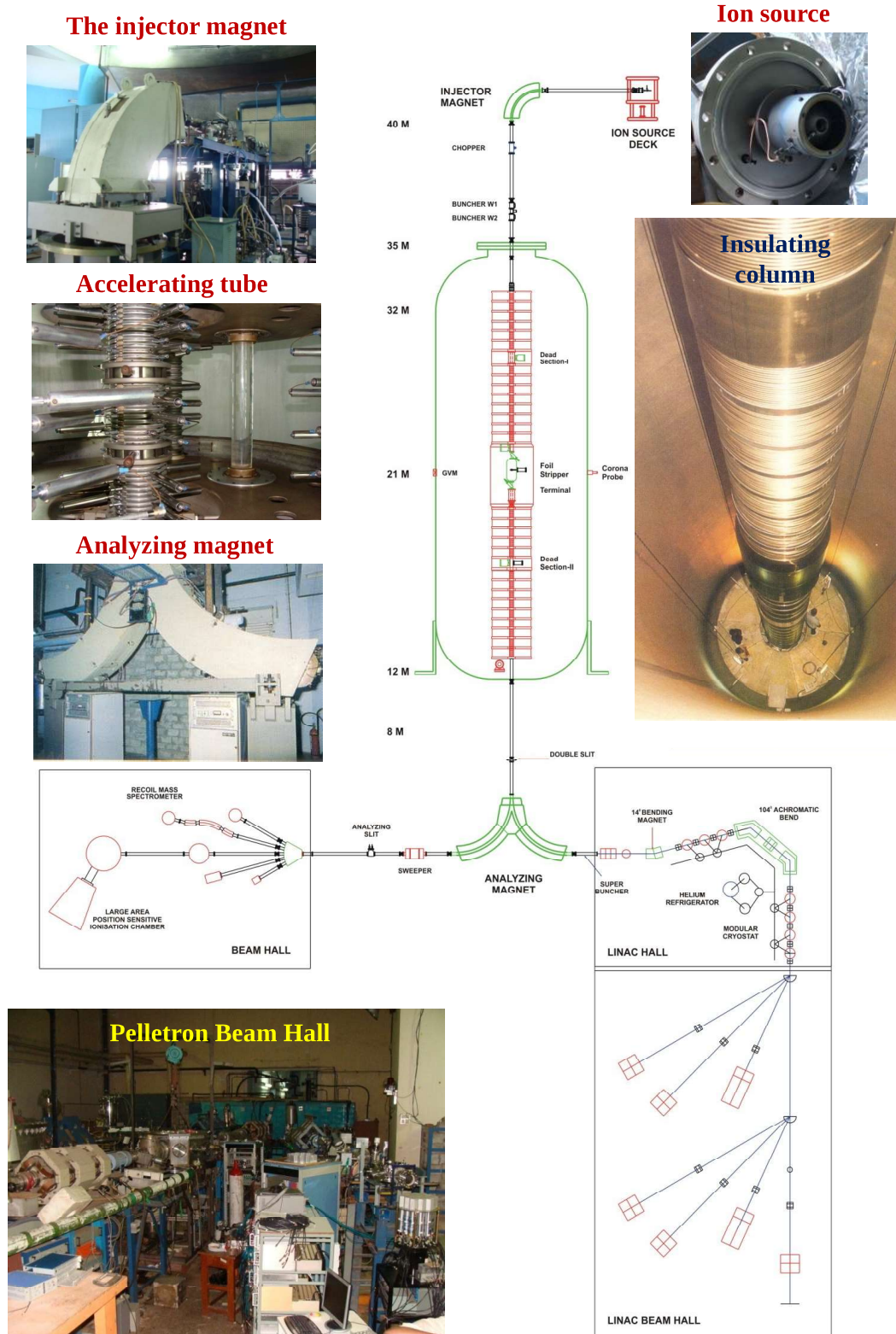
Figure 2.2: A schematic layout of Mumbai Pelletron Linac Facility.

have been measured from inclusive $\gamma$-ray counting method.

### 2.1.3   Off-beam $\gamma$-activity measurement

Residues, that have isomeric states and incomplete knowledge of decay scheme, can not be measured using in-beam $\gamma$-ray counting method. The cross sections of those nuclei were measured using off-beam $\gamma$-activity method. This method is only applicable for $\beta$-unstable nuclei having suitable half-lives. The excitation functions for $\alpha$-capture and $2n$-stripping reactions have been carried out using this method. Irradiation of $^{93}$Nb foils have been carried out using $^{7}$Li beam of energies $E_{\mathrm{lab}} = 23.6,\ 25.6,\ 27.7$ and $28.7$ MeV [52]. Aluminum catcher foils of thickness $\sim 1$ mg/cm$^2$ were used along with each target foil to stop the recoiling residues. The target and catcher foil assemblies were irradiated for $\sim 6$ h (beam current $\sim 50$ nA) at each bombarding energies and counted together at a distance of 10 cm from the detector. To monitor beam current, a CAMAC scaler was utilized which recorded the integrated current in intervals of 1 min duration. The offline $\gamma$-ray counting was carried out using an efficiency calibrated high-purity germanium (HPGe) detector. Low background was achieved by using a graded shielding (Cu, Cd sheets of thickness $\sim 2$ mm each followed by 5 cm Pb).

## 2.2   Pelletron Linac Accelerator Facility

All the experiments documented in this thesis have been carried out at Pelletron Linac Facility (PLF), Mumbai. The PLF is a joint collaborative project between BARC and TIFR. Since the commissioning in 1988, these accelerators have been

Si surface-barrier detectors (thickness $\sim 300~\mu$m) were kept at $\pm 20°$ for absolute normalization.

## 2.1.2 Measurement of prompt $\gamma$-rays: inclusive and in coincidence with non captured fragment

The fragment capture reaction mechanisms have been studied for $^7$Li+$^{93}$Nb system. In the reactions involving $^7$Li, due to the predominant $\alpha + t$ cluster structure, $\alpha$-capture and $t$-capture are the main fragment capture reaction mechanisms. For the present system $^7$Li+$^{93}$Nb, $\alpha$-capture and $t$-capture lead to the composite system $^{97}$Tc and $^{96}$Mo, respectively. Exclusive particle-$\gamma$ coincidences have been carried out to uniquely identify the various fragment capture mechanisms. Prompt $\gamma$-ray measurements have been carried out at energies $E_{\text{lab}} = 23.6, 25.6, 27.7$ and 28.7 MeV, of which some are the overlapped energy of the breakup and transfer-breakup measurements [52]. Self-supporting $^{93}$Nb foils of thickness $\sim 1.6$ mg/cm$^2$ were used as targets. The in-beam $\gamma$-ray measurements have been performed using Indian National Gamma Array (INGA). In this particular array configuration, the detectors are arranged in six different angles with three detectors at 23°, six detectors at 40°, five detectors at 65°, and four detectors at 90° with respect to the beam direction. Three Si surface barrier telescopes (thicknesses: $\Delta E \sim 15$-30 $\mu$m, $E \sim 300$-5000 $\mu$m) were kept inside the scattering chamber at fixed angles $35^o$, $45^o$, and $70^o$ for the detection of charged particles. One Si surface-barrier detector (thickness $\sim 300~\mu$m) was kept at 20° to monitor Rutherford scattering for absolute normalization. The time stamped data were collected using a digital data acquisition system with a sampling rate of 100 MHz. The absolute cross sections of most of the residues populated in the $t$-capture and complete fusion reactions

complete fusion.

### 2.1.1 Measurement of breakup fragments in coincidence

Measurements of cross section of the breakup and nucleon transfer followed by breakup (transfer-breakup) reaction have been carried out for $^7$Li + $^{89}$Y system at energies $E_{\text{lab}}$ = 22.6, 27.7 and 28.7 MeV, and for $^7$Li + $^{93}$Nb system at energies $E_{\text{lab}}$ = 23.6, 27.7 and 28.7 MeV [50, 51]. Self-supporting $^{89}$Y foil of thickness $\sim 2.0$ mg/cm$^2$ and $^{93}$Nb foil of thickness $\sim 1.75$ mg/cm$^2$ have been used as targets. The breakup events from low lying states of ejectile lead to a very small relative angle between the breakup fragments. The cross sections of these reaction channels are also very small compared to the elastic scattering cross sections around the grazing angle. These difficulties are overcome by using highly granular and segmented large area Si-detectors. The active area of these Si-detectors is $5 \times 5$ cm$^2$. Particles are identified by energy loss technique using Si-telescopes consisting of $\Delta E$ and $E$ detectors. The thicknesses of the $\Delta E$ and the $E$ detectors used in the experiment are 50 $\mu$m and 1.5 mm, respectively. The $\Delta E$ detectors are single-sided and the $E$ detector are double-sided with 16 strips allowing a maximum of 256 pixels. Two such telescopes have been used in the experiments. These telescopes, set 30° apart, were mounted at a distance of 16 cm from the target on a movable arm in a scattering chamber. In this geometry, the cone angle between the two detected fragments ranged from 1° to 24°. The angular range 30°-130° (around the grazing angle) was covered by measurements at different angle settings. Three Si surface-barrier detector telescopes (thicknesses: $\Delta E \sim$ 20-50 $\mu$m, $E \sim$ 450-1000 $\mu$m) were used to obtain the elastic scattering angular distribution at forward angles (25°-40°) where the count rate is too high for the strip detectors to cope with. Two
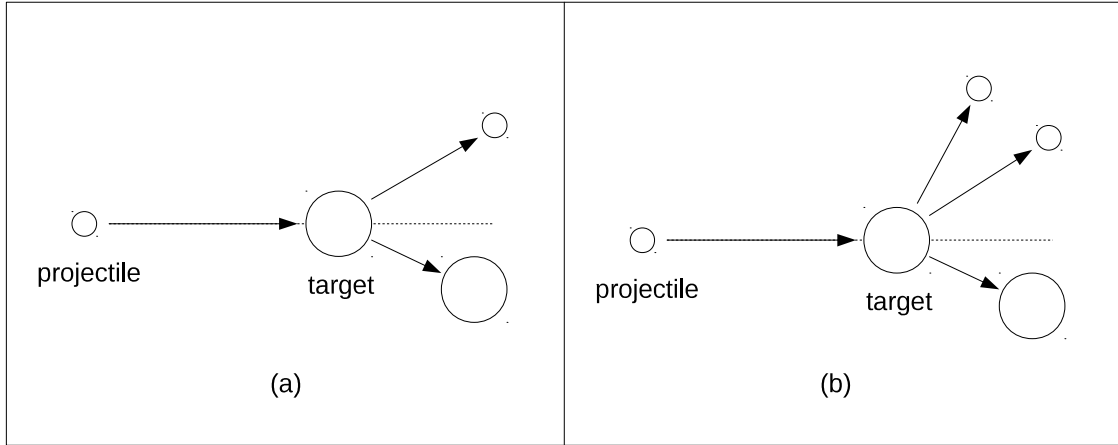
Figure 2.1: Nuclear reactions: (a) two particles in the outgoing channel, (b) three particles in the outgoing channel.

## 2.1 Experimental Details

A complete measurement of the breakup, transfer-breakup and fragments capture reaction channels along with elastic scattering and fusion reactions have been carried out in this thesis work. Two sets of measurements have been performed.

(a) To study the breakup and transfer-breakup reaction mechanisms, breakup fragments have been measured in coincidence.

(b) The fragments capture mechanism has been studied by measuring $\gamma$-rays, emitted from the composite systems in coincidence with the non-captured fragments. Inclusive measurements employing in-beam and off-beam methods have been performed to obtain cross sections of the residues from fragment capture and

# 2

# Experimental Aspects

The detection and identification of the particles and $\gamma$-rays originating due to collision of two nuclei are basic tools to study various aspects of nuclear reactions. Here identification corresponds to the details of mass, charge, energy, and angle of scattering of the particle. In case of nuclear reactions, as shown in Fig. 2.1(a), that have only two particles in the outgoing channels, the kinematic details of the reaction process can be extracted by identifying any one of the particles. The situation becomes complicated when more than two particles are emitted in the outgoing channels. Breakup, nucleon transfer followed by breakup etc. are the example of these type of reactions. Reaction processes that have three particle in the outgoing channels, as shown Fig. 2.1(b), can be studied by measuring atleast any two of the particles in coincidence. From the experimental point of view, coincidence method is very sensitive to the excitation energy of the ejectile prior to breakup and therefore to the state involved in the two-step processes.

formalism and Monte Carlo procedure. This follows the decay of individual compound nuclei in an initial ensemble by Monte Carlo technique until the residual nucleus can no longer decay by fission, particle emission or gamma decay.

In this thesis work, the statistical model code PACE (Projection Angular-momentum Coupled Evaporation) has been used to do the statistical model calculations [78]. This code has been used to understand the measured cross sections of the residues populated due to compound nuclear reactions.

$$P_{BU}(R_{\min}) = 2 \int_{R_{\min}}^{\infty} P_{BU}^{L}(R)dR = A exp(-\alpha R_{\min}) \qquad (3.48)$$

where, $A$ and $\alpha$ are the amplitude and slope of the breakup probability function. The location $(R)$ of the breakup are determined by Monte Carlo sampling of the breakup function up to $R_{\max}$ (typical value of $R_{\max} = 50$ fm). The angular momentum $L$ are also sampled between zero and maximum value $(L_{\max})$ using Monte Carlo method. In this model, the excitation energy $E^{*}$ of the projectile $(E_{\min} \leq E^{*} \leq E_{\max})$, the distance of separation between the fragment and their orientations, are also Monte Carlo sampled. In common practice, the $E_{\min}$ is considered as equal to breakup threshold $E_{\text{th}}$. In the model framework, ICF occurs when any of the breakup fragment penetrates the Coulomb barrier between the fragment and the target and CF occurs when the entire projectile or both the fragments get captured inside the interaction barriers.

The code PLATYPUS is the available computer code for the classical dynamical trajectory model calculation. The code calculates (i) integrated complete and incomplete fusion cross sections and their angular momentum distribution, (ii) the excitation energy distribution of the primary incomplete-fusion products, (iii) the asymptotic angular distribution of the incomplete-fusion products and the surviving breakup fragments, and (iv) breakup observables, such as angle, kinetic energy and relative energy distributions.

## 3.5 Statistical model

In the statistical model calculation for compound nuclear evaporation, the decay sequence of an excited compound nucleus determined using the Hauser-Feshbach
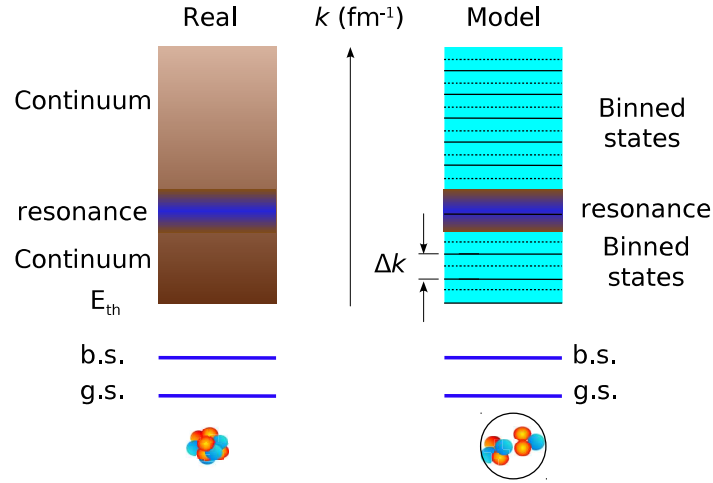
Figure 3.7: The modeled continuum and resonance states used in CDCC formalism.

## 3.4   Classical dynamical trajectory model

The continuum discretized coupled channels (CDCC) method [35] provides good results concerning certain observables such as the total fusion (TF) (i.e., the sum of ICF and CF), the elastic, breakup and transfer-breakup cross sections. This method can not separate the CF and ICF. A three-dimensional classical dynamical reaction model with stochastic breakup has been developed to estimate the relative contribution of CF and ICF [31, 36]. In the model calculations, the weakly bound projectile is considered to have a two body cluster structure. The classical trajectories of the projectile prior to breakup are calculated by numerical solution of the classical equations of motion in the presence of the Coulomb and nuclear potentials between projectile and target. The breakup probability $P_{BU}^L(R)$, corresponding to the incident particle of energy $E_0$ and angular momentum $L_0$, are calculated using the function

of the bound and continuum states wave functions of the weakly bound nuclei simultaneously. The ground state spin and parity of the core is coupled with spin and parity of the valence particle using a suitable relative angular momentum to reproduce the exact spin and parity of the ground state as well as continuum states wave functions. The Woods-Saxon type of potential is used as binding potential and well depth is adjusted to reproduce the binding energy.

The continuum is discretised into a series of momentum bins with respect to the momentum $\hbar k$ of the core-valence relative motion as shown in Fig. 3.7. In the coupled-channels calculations, each momentum bin shown as dashed lines in the Fig. 3.7, are treated as the excited state with excitation energy $E^* = \frac{\hbar^2 k^2}{2\mu}$. Here $\mu$ is the reduced mass of the core-valence system. The wave function $\phi(r, k)$ for the continuum bins are averaged over the bin width $\Delta k$ and normalized to unity using the definition

$$\psi(r) = \frac{1}{\sqrt{N\Delta k}} \int_{\Delta k} \phi(r, k) dk, \tag{3.47}$$

where $N$ is the normalization factor and $r$ is the radial separation between the core and valence.

In this thesis work, the CDCC, CCBA, DWBA calculations have been carried out using the code FRESCO, which was developed by I. J. Thompson for coupled channel calculations [35]. This code is capable to calculate the cross sections of elastic scattering, inelastic scattering, total fusion, nucleon transfer, breakup, and transfer-breakup. In addition to the measurable quantities, the code also provide the polarization potential due to the couplings.
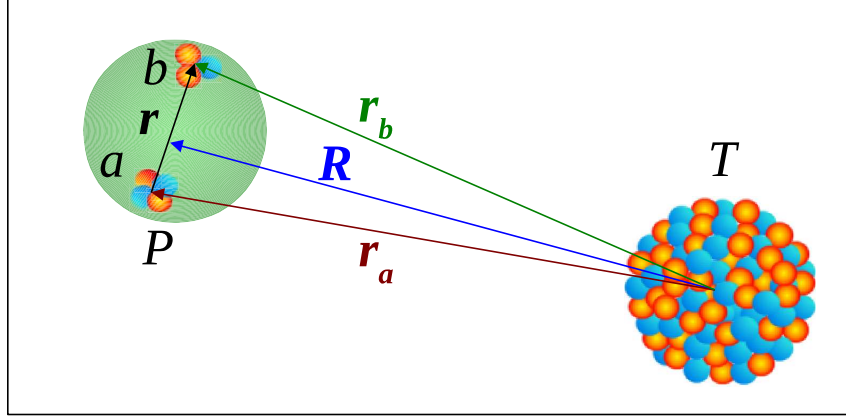
Figure 3.6: Schematic sketch of the weakly-bound projectile $P$ composed of two cluster $a$ and $b$ interacting with the target $T$.

other loosely bound nuclei, such as $^{6,7}$Li, $^{9}$Be etc. Several formalisms have been developed to account for the effects of the coupling to breakup channels on reaction observables [35, 71, 72, 73, 74, 75, 76]. One of the difficulties in CDCC formalism is dealing with more than two bodies. Even though weakly bound nuclei may consist of more than two clusters, for simplicity we concentrate in weakly bound nuclei composed of a core plus a valence particle as shown in Fig. 3.6. In this case, the interaction between target and projectile are usually calculated using cluster folding model [76, 77]. According to the cluster folding model, the interaction potential can be calculated as

$$V_{CF}(\mathbf{R}) = \langle \Psi_f(\mathbf{r}) \mid V_a(\mathbf{r_a}) + V_b(\mathbf{r_b}) \mid \Psi_i(\mathbf{r}) \rangle \tag{3.46}$$

where, $V_a$ and $V_b$ are the individual interaction potential of cluster $a$ and $b$ with the target $T$.

Another challenging task in the CDCC formalism is the precise construction

belonging to $P$ channels. The states that belong to $P\Psi$ can be written as

$$P\Psi \equiv \Psi(P) = \sum_i^N \chi_i \Phi_i \tag{3.43}$$

where $\Phi_i$ are the intrinsic bound states of the system and $\chi_i$ are the wave function describing relative motion. There are $N$ number of finite set of square-integrable basis states, which lead to a finite set of equations coupling the channel wave functions $\psi_i$. For several mass partitions the wave function $\Psi(P)$ can be written as

$$\Psi(P) = \Psi_\alpha = \sum_{\alpha'} \chi_{\alpha'}^\alpha \Phi_{\alpha'} + \sum_{\beta'} \chi_{\beta'}^\alpha \Phi_{\beta'} \tag{3.44}$$

and the solvable coupled equations are

$$(E_{\alpha'} - T_{\alpha'} - U_{\alpha'})\chi_{\alpha'}^{\alpha(+)} = \sum_{\alpha''} U_{\alpha'\alpha''} \chi_{\alpha''}^{\alpha(+)} + \sum_{\beta'} (\Phi_{\alpha'} \mid V_\alpha - \hat{U}_\alpha \mid \chi_{\beta'}^{\alpha(+)} \Phi_{\beta'}) \tag{3.45}$$

The coupled equation can be solved by N-step DWBA approximation or by iteration approaches given in Ref. [35].

### 3.3.5 Continuum Discretized Coupled Channels (CDCC) formalism

In case of weakly bound and unbound nuclei, reaction dynamics are influenced by continuum or positive-energy states. Collisions of these systems with stable nuclei will also be influenced by the coupling to the unbound states. This effect was first noticed in deuteron-induced reactions and later observed in the scattering of
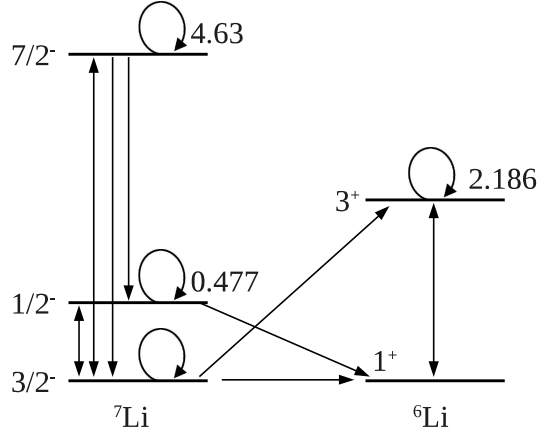
Figure 3.5: Reduced coupling scheme of the CCBA calculation for $1n$-stripping followed by breakup ($^{7}$Li,$^{6}$Li$\rightarrow \alpha + d$) reaction.

coupling scheme in the entrance and exit partitions is shown in Fig. 3.5 for $1n$-stripping followed by breakup ($^{7}$Li,$^{6}$Li$\rightarrow \alpha + d$) reaction.

## 3.3.4 Coupled Reaction Channels (CRC) formalism

The CCBA formalism can be used for the cases, where transfer processes are very weak relative to the inelastic transitions. Whereas, for strong transfer processes the CCBA is inadequate and coupled reaction channels (CRC) formalism is useful. In this section, we will discuss the CRC approximation. The CRC model of direct reactions in nuclear physics proceeds by constructing a model of the system wave function, and solving Schrödinger's equation as accurately as possible within that model space [35, 65, 66, 67, 69]. As mentioned in Sec. 3.1, the Eq. 3.5 contains all the information required to calculate transitions probability among states

$$\mathcal{J}_{\beta\alpha} = \langle \Psi_\beta^{(-)} \mid V_\beta - \hat{U}_\alpha \mid \chi_\alpha^{(+)} \rangle = \langle \chi_\beta^{(-)} \mid V_\beta - \hat{U}_\beta \mid \Psi_\alpha^{(+)} \rangle \qquad (3.38)$$

This is an exact result. Now, if $\chi_\beta^{(-)}$ is the solution of Schrödinger equation containing $\hat{U}_\beta^\dagger$, then

$$(E - H_\beta - T_\beta - \hat{U}_\beta^\dagger)\hat{\chi}_\beta^{(-)}(\mathbf{r}_\beta, \mathbf{B}, \mathbf{b}) = \mathbf{0} \qquad (3.39)$$

and

$$\hat{\chi}_\beta^{(-)}(\mathbf{r}_\beta, \mathbf{B}, \mathbf{b}) = \sum_{\beta'} \chi_{\beta'}^{\beta(-)}(\mathbf{r}_\beta)\mathbf{\Phi}_{\beta'}(\mathbf{B}, \mathbf{b})) \qquad (3.40)$$

where, the superscript in $\chi_{\beta'}^\beta$ denotes the original state of the system as being the channel $\beta$ of the partition $B+b$, and the subscript $\beta'$ denotes the possible other channels in the same partition. The state corresponding to $\beta'$ can be reached by the interaction $\hat{U}_\beta$. The CCBA transition matrix can be obtained solving the inelastic transitions within the $\alpha$ and $\beta$ partitions from coupled channels frame work and DWBA prescription for transfer process. The CCBA transition matrix will be

$$\mathcal{J}_{\beta\alpha(post)}^{CCBA} = \sum_{\alpha'\beta'} \langle \chi_{\beta'}^{\beta(-)} \mid V_\beta - \hat{U}_\beta \mid \chi_{\alpha'}^{\alpha(+)}\Phi_{\alpha'} \rangle \qquad (3.41)$$

and

$$\mathcal{J}_{\beta\alpha(prior)}^{CCBA} = \sum_{\alpha'\beta'} \langle \chi_{\beta'}^{\beta(-)} \mid V_\alpha - \hat{U}_\alpha \mid \chi_{\alpha'}^{\alpha(+)}\Phi_{\alpha'} \rangle \qquad (3.42)$$

The CCBA calculations have been carried out for $1n$-stripping followed by breakup ($^7$Li,$^6$Li$\rightarrow \alpha + d$) and $1p$-pickup followed by breakup ($^7$Li,$^8$Be$\rightarrow \alpha + \alpha$) reactions. A pictorial description of the CCBA calculations employing a reduced
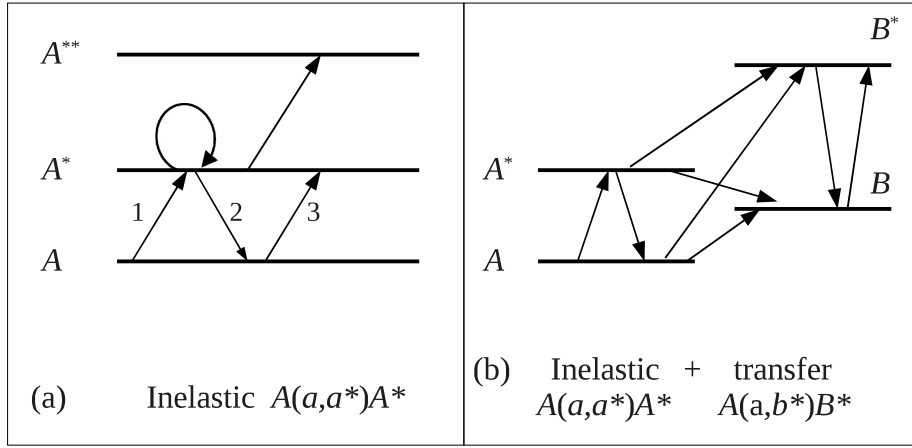
Figure 3.4: Various types of multi-step processes.

element of $V$. The number of arrows included equals the number of steps in this multi-step contribution. The first arrow 1 corresponding to the Born approximation is described above. However, $A^*$ can also be populated by de-exciting back to the ground state $A$ and re-exciting to $A^*$ (arrow 1 and arrow 2 followed by arrow 3), which is a three step process. The de-excitation step to the ground state $A$ represents a second-order contribution to the elastic scattering. If the diagonal matrix-element $\langle A^*|V|A^* \rangle$ is non vanishing, this leads to a second-order contribution to the inelastic scattering. This is known as re-orientation. Another type of multi-step processes is shown in Fig. 3.4(b). In this processes, inelastic excitation of the projectile or target could take place before the transfer reaction. The transfer process could be sufficiently weak for the DWBA description, but the inelastic events could be strong and have to be calculated by solving the corresponding coupled equation. This method is known as coupled channel Born approximation (CCBA) [65, 66, 67].

The non elastic part of Eq. 3.26 and 3.27 can be expressed with operator form of optical potential $\hat{U}_\alpha$ and $\hat{U}_\beta$ as

to the corresponding experimental separation energy. Now, from Eq. 3.14, 3.15 and 3.34 the DWBA formalism leads to the cross section of the transfer reaction

$$\left(\frac{d\sigma}{d\Omega}\right)_{DWBA} = \frac{1}{(2J_a + 1)(2J_A + 1)} \sum_{M_a M_A M_b M_B} \frac{m_a m_b}{(2\pi\hbar^2)^2} \frac{k_b}{k_a} |\mathcal{J}_{ba}(\theta)|^2 \qquad (3.36)$$

Here, $k_a$ and $k_b$ are the relative momenta of the entrance and exit channels, respectively. A comparison between the experimentally measured cross section and the DWBA calculated cross section for a transfer reaction between two well-defined states gives the factor called '*Spectroscopic Factor*' which is a structural property of the nucleus studied. The experimental cross section is related to the calculated cross section by,

$$\left(\frac{d\sigma}{d\Omega}\right)_{ex} = \left(C^2 S_1\right) \left(C^2 S_2\right) \left(\frac{d\sigma}{d\Omega}\right)_{DWBA} \qquad (3.37)$$

where the factors $C^2 S_1$ and $C^2 S_2$ describes the overlap of initial and final bound state wave functions in the projectile and target respectively. Here, the $S$'s are the spectroscopic factors and the $C$'s are the relevant isospin Clebsh-Gordan coefficients. We have used the code 'FRESCO [35]' for the Finite Range DWBA calculations.

### 3.3.3 Coupled Channels Born Approximation (CCBA)

Till now we have discussed the calculations for interaction with weak coupling potential and DWBA description is good enough to explain the measured data. Whereas for sufficiently strong couplings, only the first order consideration is inadequate and the coupled-channel formalism is required. For an example, inelastic scattering $A(a, a^*)A^*$ shown in Fig. 3.4(a), where each arrow indicates a matrix
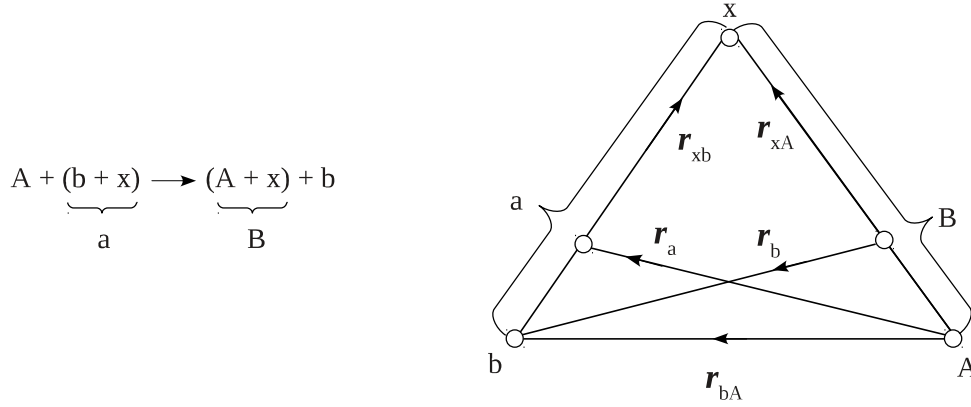
Figure 3.3: Vector diagram relating the position vectors which are involved in the DWBA amplitude. The projectile 'a' is described as composed of the core 'b' and the transferred nucleon 'x' separated by the vector $r_{xb}$. The residual nucleus 'B' is described as composed of the target 'A' and the transferred nucleon 'x' separated by the vector $r_{xA}$. The displacement vector in the incoming channel joins the centre-of-mass of 'A' to that of 'a' and in the outgoing channel, joins the centre-of-mass 'B' to that of 'b'.

$$\mathcal{J}_{ba} = \int dr_a \int dr_b \chi_b^{(-)*}(k_b, r_b) \, \langle Bb \mid V \mid Aa \rangle \, \chi_a^{(+)}(k_a, r_a) \qquad (3.34)$$

where,

$$\langle Bb \mid V \mid Aa \rangle = \int \Phi_B^* \Phi_b^* V \Phi_A \Phi_a d\xi \qquad (3.35)$$

Here, $V$ is the interaction potential responsible for the transfer of the nucleon and $\xi$ represents all the coordinates independent of $r_a$ and $r_b$. The Eqn. 3.34 is a six-dimensional numerical integral over $r_a$ and $r_b$. In case of zero range (ZR) approximation, the particle 'b' is assumed to be emitted at the same point at which particle 'a' is absorbed, so that $r_b = (M_A/M_B)r_a$. The finite range (FR) approximation (six-dimensional integration) is more accurate. The bound state wave functions are usually calculated assuming the transferred nucleon both before and after the transfer, bound in a Woods-Saxon well with a binding energy equal

$$\mathcal{J}^{DWBA}_{\beta\alpha(post)} = \langle \chi^{(-)}_{\alpha} \mid U_{\alpha} \mid \phi_{\alpha}\rangle\delta_{\alpha\beta} + \langle \chi^{(-)}_{\beta} \mid V_{\beta} - U_{\beta} \mid \chi^{(+)}_{\alpha}\rangle \tag{3.30}$$

and

$$\mathcal{J}^{DWBA}_{\beta\alpha(prior)} = \langle \chi_{\alpha} \mid U_{\alpha} \mid \chi^{(+)}_{\alpha}\rangle\delta_{\alpha\beta} + \langle \chi^{(-)}_{\beta} \mid V_{\alpha} - U_{\alpha} \mid \chi^{(+)}_{\alpha}\rangle \tag{3.31}$$

These two terms $\mathcal{J}^{DWBA}_{\beta\alpha(post)}$ and $\mathcal{J}^{DWBA}_{\beta\alpha(prior)}$ are the post and prior form of the distorted wave Born approximation. It can be easily shown that the post and prior terms are equal to each other. Hence, any one of the approaches can be considered to calculate the transition matrix. In case of nonelastic amplitudes, the first term of Eq. 3.30 and 3.31 are absent and the $\mathcal{J}^{DWBA}_{\beta\alpha(post)}$ and $\mathcal{J}^{DWBA}_{\beta\alpha(prior)}$ can be written as

$$\mathcal{J}^{DWBA}_{\beta\alpha(post)} = \langle \chi^{(-)}_{\beta} \mid V_{\beta} - U_{\beta} \mid \chi^{(+)}_{\alpha}\rangle \tag{3.32}$$

and

$$\mathcal{J}^{DWBA}_{\beta\alpha(prior)} = \langle \chi^{(-)}_{\beta} \mid V_{\alpha} - U_{\alpha} \mid \chi^{(+)}_{\alpha}\rangle \tag{3.33}$$

The wave functions $\chi^{(+)}_{\alpha}$ and $\chi^{(+)}_{\beta}$ are separable in terms of internal coordinates and relative coordinates.

Let us now calculate the $\mathcal{J}^{DWBA}_{\beta\alpha}$ for a transfer reaction shown in Fig. 3.3. The distorted wave $\chi^{(+)}_{a}$ is a function of $r_a$, displacement of 'a' from 'A' and $\chi^{(-)}_{b}$ is a function of $r_b$, displacement of 'b' from 'B' (see Fig. 3.3). The wave functions $\chi^{(+)}_{a}$ and $\chi^{(-)}_{b}$ are generated from optical model potentials which are chosen to give a best fit to the observed elastic scattering data in the entrance and exit channels respectively. The Eq. 3.32 in terms of $r_a$ and $r_b$ is written as,

Using the Eq. 3.16 and 3.25, the $T$-matrix in terms of distorted waves $\chi$ can be written as,

$$\mathcal{J}_{\beta\alpha} = \langle \phi_\beta \mid V_\beta - V_\alpha + U_\alpha \mid \chi_\alpha^{(+)} \rangle + \langle \Psi_\beta^{(-)} \mid V_\alpha - U_\alpha \mid \chi_\alpha^{(+)} \rangle \qquad (3.26)$$

In similar way using the $\beta$-partition of Eq. 3.18, it can be shown that

$$\mathcal{J}_{\beta\alpha} = \langle \chi_\beta^{(-)} \mid V_\alpha - V_\beta + U_\beta \mid \phi_\alpha \rangle + \langle \chi_\beta^{(-)} \mid V_\beta - U_\beta \mid \Psi_\alpha^{(+)} \rangle \qquad (3.27)$$

The results derived above is true for the potential $U$, which can reproduce the elastic and inelastic scattering angular distribution. In general when $U$ is considered as optical potential then the Eq. 3.26 and 3.27 can be rewritten as

$$\begin{aligned}
\mathcal{J}_{\beta\alpha} = {}& \langle \chi_\alpha^{(-)} \mid U_\alpha \mid \phi_\alpha \rangle \delta_{\alpha\beta} \\
&+ \langle \chi_\beta^{(-)} \mid (V_\beta - U_\beta) + (V_\beta - U_\beta) \frac{1}{E - H + i\epsilon} (V_\alpha - U_\alpha) \mid \chi_\alpha^{(+)} \rangle
\end{aligned} \qquad (3.28)$$

In similar way using the $\beta$-partition of Eq. 3.18, it can be shown that

$$\begin{aligned}
\mathcal{J}_{\beta\alpha} = {}& \langle \phi_\alpha \mid U_\alpha \mid \chi_\alpha^{(+)} \rangle \delta_{\alpha\beta} \\
&+ \langle \chi_\beta^{(-)} \mid (V_\alpha - U_\alpha) + (V_\beta - U_\beta) \frac{1}{E - H + i\epsilon} (V_\alpha - U_\alpha) \mid \chi_\alpha^{(+)} \rangle
\end{aligned} \qquad (3.29)$$

The approximation made by neglecting the second and higher-order terms in Eq. 3.28 and 3.29 is known as the first distorted wave Born approximation. In case of second order distorted wave Born approximation upto second-order terms are considered in the calculations. The first order distorted wave Born approximation simplified the Eq. 3.28 and 3.29 to

corresponds to a rearrangement of terms in the Hamiltonian and does not exist with the auxilliary Hamiltonians that contains only optical potential $U$

$$H \neq H_\alpha + T_\alpha + U_\alpha \neq H_\beta + T_\beta + U_\beta \tag{3.19}$$

Let us assume $\chi_\alpha$ is the distorted wave solution to

$$(E - H_\alpha - T_\alpha - U_\alpha)\chi_\alpha = 0 \tag{3.20}$$

It can also be written

$$(E - H_\alpha - T_\alpha - V_\alpha)\Psi_\alpha = 0 \tag{3.21}$$

From Eq. 3.20 and Eq. 3.21,

$$(E - H_\alpha - T_\alpha - V_\alpha)\Psi_\alpha = (E - H_\alpha - T_\alpha - U_\alpha)\chi_\alpha \tag{3.22}$$

Now, using $V_\alpha = U_\alpha + (V_\alpha - U_\alpha)$ and rearranging we can write

$$(E - H_\alpha - T_\alpha - U_\alpha)\Psi_\alpha = (V_\alpha - U_\alpha)\Psi_\alpha + (E_\alpha - H_\alpha - T_\alpha - U_\alpha)\chi_\alpha \tag{3.23}$$

Or,

$$\Psi_\alpha^{(+)} = \chi_\alpha^{(+)} + \frac{1}{E - H_\alpha - T_\alpha - U_\alpha + i\epsilon}(V_\alpha - U_\alpha)\Psi_\alpha^{(+)} \tag{3.24}$$

here an infinitesimal small term $i\epsilon$ is added to maintain the boundary condition of the outgoing waves at infinity. The Eq. 3.24 can be further simplified to

$$\Psi_\alpha^{(+)} = \chi_\alpha^{(+)} + \frac{1}{E - H + i\epsilon}(V_\alpha - U_\alpha)\chi_\alpha^{(+)} \tag{3.25}$$

## 3.3.2   Distorted Wave Born Approximation (DWBA)

The Distorted Wave Born Approximation (DWBA) is the most useful formalism to describe the direct nuclear reactions [65, 66, 67, 68, 69]. In the DWBA formalism, the direct nuclear reactions are assumed as being caused by weak interaction that induces a transition to occur between two channels. The relative motion of incoming and out going nuclei are described by optical potential. The principal assumptions in DWBA formalism are

1. The transition takes place directly from the initial to final states.

2. Most of the nucleons of the projectile as well as the targets remain effectively passive. For an example, all the nucleons except those actually transferred are assumed to remain in their original states for the calculations of nucleon transfer reactions.

3. The reaction is assumed to be sufficiently weak that it can be treated in lowest order.

The interaction potential is separated into two parts $V = U + (V - U)$ such that the optical potential $U$ is responsible for the elastic and inelastic transitions. This part of the problem can be solved exactly using the Gell-Mann-Goldberger transformation [70]. The remaining interaction $(V - U)$ is regarded as weak and responsible for direct reactions e.g., nucleon transfer. In this formalism the equality

$$H = H_\alpha + T_\alpha + V_\alpha = H_\beta + T_\beta + V_\beta \qquad (3.18)$$

spin of orientations of ejectile and target like nuclei are not measured. The spins of the nuclear states of all the nuclei $a$, $A$, $b$, and $B$ are suppose to contribute to the total cross section. Hence, the cross section is an average of the preceding one over the initial angular momentum projections of $J_a$ and $J_A$, and a sum over the final projections of $J_b$ and $J_B$. The average cross section

$$\frac{d\sigma}{d\Omega} = \frac{1}{(2J_a + 1)(2J_A + 1)} \sum_{M_a M_A M_b M_B} \left( \frac{d\sigma}{d\Omega} \right)_{\beta\alpha} \tag{3.15}$$

The $T$ matrix of Eq. 3.14 can be derived as,

$$\mathcal{J}_{\beta\alpha} = \langle \phi_\beta \mid V_\beta \mid \Psi_\alpha^{(+)} \rangle \tag{3.16}$$

where, $\phi_\beta = \Phi_\beta e^{(i\mathbf{k}_\beta \cdot \mathbf{r}_\beta)}$ is the outgoing total wave function in the $\beta$-partition, and $\Psi_\alpha^{(+)}$ is the asymptotic form of $\Psi_\alpha$, which is defined in Eq. 3.9-3.12. It is not possible to calculate the exact value of $T$ matrix due to the presence of unknown complete wave function $\Psi_\alpha^{(+)}$ in the expression of $\mathcal{J}_{\beta\alpha}$ in Eq. 3.16. However, this problem can be solved after considering certain approximations. The available mathematical models along with respective approximations will be discussed now.

### 3.3.1   Plane Wave Born Approximation (PWBA)

In the plane wave Born approximation (PWBA), the effect of the scattering is considered as negligible. Hence, from the Eq. 3.9-3.12 the wave function can be assumed as $\Psi_\alpha^{(+)} \simeq \phi_\alpha = \Phi_\alpha e^{(i\mathbf{k}_\alpha \cdot \mathbf{r}_\alpha)}$, and consequently

$$\mathcal{J}_{\beta\alpha} = \langle \phi_\beta \mid V_\beta \mid \phi_\alpha \rangle \tag{3.17}$$

$$\Psi_{el} = \Phi_\alpha [e^{(i\mathbf{k}_\alpha \cdot \mathbf{r}_\alpha)} + f_{\alpha\alpha}(\theta)\frac{e^{(ik_\alpha r_\alpha)}}{r_\alpha}], \tag{3.10}$$

$$\Psi_{inel} = \sum_{\alpha' \neq \alpha} \Phi_{\alpha'} f_{\alpha'\alpha}(\theta)\frac{e^{(ik_{\alpha'} r_{\alpha'})}}{r_{\alpha'}}, \tag{3.11}$$

$$\Psi_{transfer} = \sum_\beta \Phi_\beta f_{\beta\alpha}(\theta)\frac{e^{(ik_\beta r_\beta)}}{r_\beta}, \tag{3.12}$$

where, $\Phi$'s, k's, and r's are the intrinsic bound states, momentum vector, and relative coordinate between the two nuclei, respectively for the corresponding partitions. The summation in Eq. 3.11 and 3.12 are to take into account all possible inelastic and nucleon transfer reaction processes. The function $f(\theta)$'s are amplitude of the scattered waves in the corresponding partition. The differential cross section of particles scattered in the direction $\theta$ is defined as the flux of scattered particles through the area $dA = r^2 d\Omega$ in the direction $\theta$, per unit incident flux [67]. From the quantum mechanical current it can be shown that, the differential cross sections at $r_\beta \rightarrow \infty$

$$\left(\frac{d\sigma}{d\Omega}\right)_{\beta\alpha} = \frac{m_\alpha}{m_\beta}\frac{k_\beta}{k_\alpha}|f_{\beta\alpha}(\theta)|^2 \tag{3.13}$$

where, $m_\alpha, m_\beta, k_\alpha$, and $k_\beta$ are the reduced masses and relative momenta of the corresponding partition $\alpha$ and $\beta$, respectively [67]. In terms of $T$ matrix,

$$\left(\frac{d\sigma}{d\Omega}\right)_{\beta\alpha} = \frac{m_\alpha m_\beta}{(2\pi\hbar^2)^2}\frac{k_\beta}{k_\alpha}|\mathcal{J}_{\beta\alpha}(\theta)|^2 \tag{3.14}$$

This is the differential cross section for the transition $\alpha \rightarrow \beta$. In a typical measurements, the projectile is unpolarized and the target is unaligned. The final

a particle cluster. In the following sections, the theoretical formalism to calculate the cross sections of the direct nuclear reactions are discussed.

In the direct reaction, the incident particle interacts with the target nucleus only several times at most. Therefore the change produced in the target must be a simple rearrangement of one or several nucleons or collective degrees of freedom. Because of the conservation laws, the change produced in the nucleus must be reflected in the energy and angular momentum carried by the outgoing particle [65, 66, 67].

The possible direct nuclear reactions due to collision of two nuclei $a$ and $A$ can be divided into three parts to solve the problems in simpler way.

$$a + A \rightarrow a + A, \text{ elastic scattering and labeled as } \alpha\text{-partition}$$
$$a + A \rightarrow a^* + A^*, \text{ inelastic scattering and labeled as } \alpha'\text{-partition}$$
$$a + A \rightarrow b^* + B^*, \text{ transfer reaction and labeled as } \beta\text{-partition}$$

The complete wave functions $\Psi_\alpha$ must contain the description of all the above discussed events. Hence, $\Psi_\alpha$ can be written as

$$\Psi_\alpha = \Psi_{el} + \Psi_{inel} + \Psi_{transfer} \tag{3.9}$$

where, the three terms correspond to the elastic, inelastic, and transfer channels, respectively. The exact knowledge of $\Psi_\alpha$ is very important for the estimation of cross section of any reaction channels. For a large relative coordinate in any two-body partition, the behavior of the three terms for large value of $r \rightarrow \infty$ can be expressed as

reactions. In such small time interval only few degrees of freedom are excited and the other degrees of freedom of the many-body system remain effectively passive. At the opposite extreme are compound nuclear reactions, for which the reaction time scale is almost 100 times more than the time scale of the direct reaction processes. In case of the compound nuclear reactions, the incident particle interacts successively with a number of nucleons of the target nuclei until most of its energy has been shared among many nucleons. In this case a large number of degrees of freedom get excited. Hence, different types of model frame work is required to understand the direct and compound nuclear reactions. A nuclear interaction with a given impact parameter $b$, which is defined as the perpendicular distance between the center of the colliding nuclei at infinity, will experience different regions of the inter-nuclear interaction as the nuclei approach and recede. Hence, different reaction outcomes can occur, depending on $b$, which is illustrated in Fig. 3.2(a). The typical cross section of direct and compound nuclear reaction as a function of angular momentum are shown in Fig. 3.2(b).

## 3.3 Direct nuclear reactions

Inelastic scattering, nucleon transfer, breakup etc are few examples of the direct nuclear reactions [65, 66, 67]. Inelastic excitation may occur, for example, when one or both of the nuclei are deformed or deformable, with the result that higher energy states of the nuclei may become populated. Single particle excitation is another kind of inelastic process, where a particle in any one of the colliding nuclei is excited during the reaction from its initial bound state to another state which may be bound or unbound. Nucleons may also get transferred from one nucleus to the other, either singly, or as the simultaneous transfer of more than one nucleons as

coefficients that enter the statistical model of compound nucleus evaporation, the distorted wave functions that are used for the description of direct inelastic scattering to discrete states as well as in evaluations of multi step direct transitions to the continuum and nucleon transfer channels.
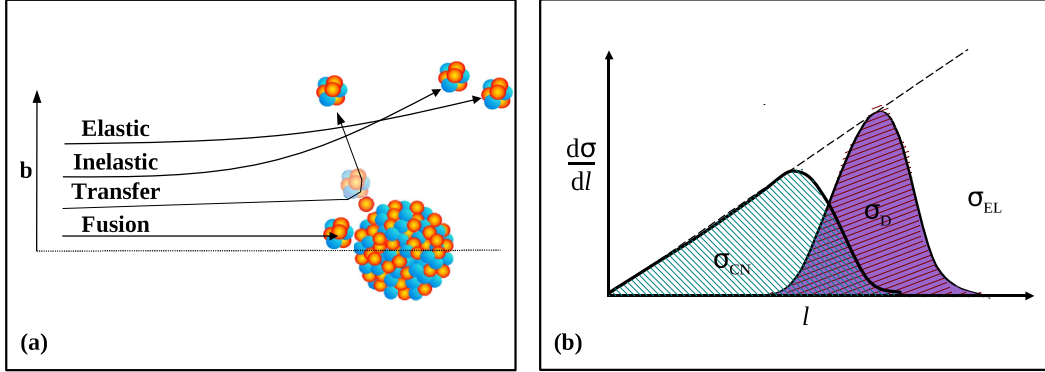


Figure 3.2: (a) Schematic illustration of different processes as a function of impact parameter $b$. (b) Reaction classification by angular momentum ($\ell$). Schematic decomposition of total cross section into the cross section of compound nuclear formation ($\sigma_{CN}$) and direct reaction ($\sigma_D$) along with the elastic scattering ($\sigma_{EL}$).

## 3.2   Direct and compound nuclear reaction

As discussed in the previous section, the cumulative contribution of all the non-elastic reaction channels can be accounted using the absorbing imaginary potential in the optical model [65, 66, 67]. The non-elastic reactions channels can be divided into two categories on the basis of the reaction time scales. The reaction processes that have time scale of the same order of the nuclear reaction time are called direct

where,

$$\mathscr{V} = V_{PP} + V_{PQ}\frac{1}{(E - H_{QQ} + i\epsilon)}V_{QP}. \tag{3.7}$$

If our interest is only on the elastic channel, $P$ contains only elastic channels and all other inelastic channels will be absorbed in $Q$. The complicated potential in Eq. 3.7 can be represented by a complex mean-field potential $U(r)$:

$$U(r) = (V_0 + iW_0)f(r) \tag{3.8}$$

where $f(r) = [1 + \exp(\frac{r-R}{a})]^{-1}$ and $V_0$, $W_0$, $R$ and $a$ are the optical model parameters [60, 63, 64]. The purpose of using this type of potential is to divide the reaction flux into two parts, one of them representing the elastic scattering and the other one describing all competing non-elastic channels. The real part $V_0$ represents the strength of potential which causes the elastic scattering and the imaginary part $W_0$ gives the strength of absorptive potential through all non-elastic channels. The solution of Schrödinger equation with this complex potential gives the estimation of the elastic scattering angular distribution and total reaction cross sections, which accounts for the loss of incident flux. This absorption may be of different kinds depending upon the energy and the structure of the interacting particles. In some cases, the absorption is of surface type while in other cases of volume type or a combination of both. The other two parameters $R$ and $a$ are called as half value radius and the diffuseness respectively.

This model is useful to predict the elastic scattering angular distribution for energies and nuclides for which no experimental measurement data exist. The optical model is useful to evaluate the various non-elastic channels, e.g. transmission

$$(E - H)(P + Q)\Psi = 0 \tag{3.1}$$

Projecting from the left with $Q$ leads to

$$(E - H_{QQ})(Q\Psi) = H_{QP}(P\Psi) \tag{3.2}$$

where, $H_{QP} = QHP$ and $H_{QQ} = QHQ$. The solution of Eq. 3.2 can be written as

$$(Q\Psi) = \frac{1}{(E - H_{QQ} + i\epsilon)} H_{QP}(P\Psi) \tag{3.3}$$

where, as usual, $i\epsilon$ yields the asymptotic boundary condition on the Green's functions that there are outgoing waves. Now, projecting from left side of Eq. 3.1 with $P$

$$(E - H_{PP})(P\Psi) = H_{PQ}(Q\Psi) \tag{3.4}$$

Substituting Eq. 3.3 in Eq. 3.4 leads to

$$\left[ E - H_{PP} - H_{PQ} \frac{1}{(E - H_{QQ} + i\epsilon)} H_{QP} \right](P\Psi) = 0 \tag{3.5}$$

The above equation is satisfied by that part of $\Psi$ in which we are only interested, namely, $P\Psi$. It contains all the necessary information required to calculate transitions probability among states belonging to $P$. Now, considering $H_{PP} = H_\alpha$ - $T$ - $V_{PP}$, the Eq. 3.4 can be written as

$$(E - H_\alpha - T - \mathscr{V})\Psi(P) = 0 \tag{3.6}$$

energies near the Coulomb barrier and non-relativistic formalism is good enough in this energy zone. Hence, the discussion on theoretical formalism will be limited to only non-relativistic treatment in this thesis work.

A nucleus represents a finite self-bound fermionic many-body quantum mechanical system. In priciple, all possible mutual two-body interactions should be considered to understand the properties of nuclei. At the same time it has been observed that, similar to the atomic physics, many properties such as spin, parity, nucleon separation energies, etc depend only on the outer shell nucleons. Eventually this leads to the concept of mean field theory, where all the individual two-body interactions are replaced by an average or mean-field potential. The models, used in this thesis, are based on the mean field approximation.

## 3.1   Optical model

The optical model is a very useful method to estimate the scattering as well as absorption cross sections simultaneously. The concept of the optical model has come from the similar approach of treatment used for the scattering of light by a refracting and absorbing medium. The optical model has been developed using the unified nuclear reaction formalism of Feshbach [60, 61]. In the unified nuclear reaction theory, the direct interaction treatment of elastic and inelastic scattering with an $n$-state approximation for compound nucleus effects are combined [62]. Two projection operator $P$ and $Q$ are defined such that, $P + Q = 1$, $P^2\Psi = P\Psi$, $Q^2\Psi = Q\Psi$, and $PQ\Psi = QP\Psi = 0$. $P\Psi$ asymptotically contains only the $P$ channels, which are opened and resolved channels. Similarly, the projections $Q\Psi$ leads to the $Q$ channels, which are referred to the unknown or unresolved channels. The Schrödinger's equation can be written as

# 3

# Theoretical models

The nucleus-nucleus interaction is a very complex phenomena. To understand this subject requires dealing with many body problem. At the same time normal statistical mechanics is not applicable as nuclei consist of very less number of nucleons (max $\sim 300$). There are certain number of models available to interpret the measured observables. Before going to start the discussion on different nuclear models, let us look at some of the features of a nucleus. The average binding energy of a nucleon in stable nuclei is $\sim 8$ MeV and the kinetic energy $\sim 40$ MeV, while the nucleon mass is mc$^2$ $\sim 938$ MeV. Hence, the kinetic energy is negligible compared to the mass, leading to the assumption of non-relativistic theory to be able to describe the nucleus. But the scenario will be different, if we look deep inside. The estimated velocity of such nucleon will be 0.3c and corresponding de Broglie wavelength will be $\sim 4.5$ fm, which is not small compared to nuclear radius whose range is from 1.2 fm up to 8 fm, leading to the fact that quantum effect must not be negligible in case of nuclei.

In this thesis, the collision of two nuclei have been studied at the bombarding

of $\alpha - \alpha$ events. The asymmetry arises due to the different kinematic focusing for the coincident fragments. It is also found that the asymmetry depends on the difference in mass of the two fragments, relative energy, relative angle and the scattering angle of the ejectile. The asymmetry is defined as the ratio of yields of the high energy (forward going) and low energy (backward going) groups of the fragment. The dependency of asymmetry as a function $E_{\mathrm{rel}}$ and $\theta_{\mathrm{rel}}$ are shown in Fig. 4.6(a) and (b), respectively for the breakup of $^7$Li in $^7$Li+$^{93}$Nb reaction at $E_{\mathrm{lab}}$ = 28 MeV. The validity of the simulation has also been checked by reproducing the asymmetry of $\alpha - d$ coincidence events for $^6$Li + $^{209}$Bi reaction of Ref. [39].

### 4.1.4 Asymmetry of yields in correlated energy spectra

Depending on the orientation of the breakup relative to the velocity of the ejectile prior to breakup and detection conditions, two types of coincidence events of high (low) energy $\alpha(d)$ and low (high) energy $\alpha(d)$ have been observed, as shown in Fig. 2.13(b) and Fig. 5.3. The yields corresponding to the high and low energy $\alpha$ particle are found to be asymmetric. Such an asymmetry was also observed in Ref. [39] and different cross sections for the high and low energy fragments were reported. However, in the present work, the observed asymmetry has been reproduced by the simulation and consequently consistent cross sections for the high and low energy $\alpha$ particles have been obtained.
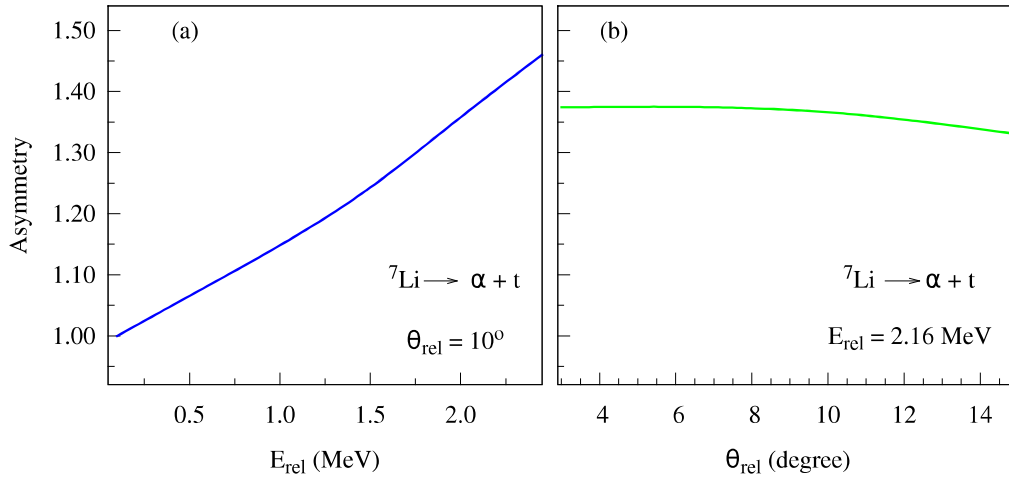


Figure 4.6: Simulated asymmetry of $\alpha - t$ events due to the breakup of $^7$Li in $^7$Li+$^{93}$Nb reaction at $E_{\mathrm{lab}} = 28$ MeV. Dependency of asymmetry as a function of (a) $E_{\mathrm{rel}}$ and (b) $\theta_{\mathrm{rel}}$.

The simulated energy spectra of breakup fragments $\alpha - d$, $\alpha - t$, and $\alpha - \alpha$, due to the breakup of $^6$Li, $^7$Li, and $^8$Be, respectively are shown in Fig. 4.5. Although the asymmetry is observed in $\alpha - d$ and $\alpha - t$ events, it is not present in energy spectra
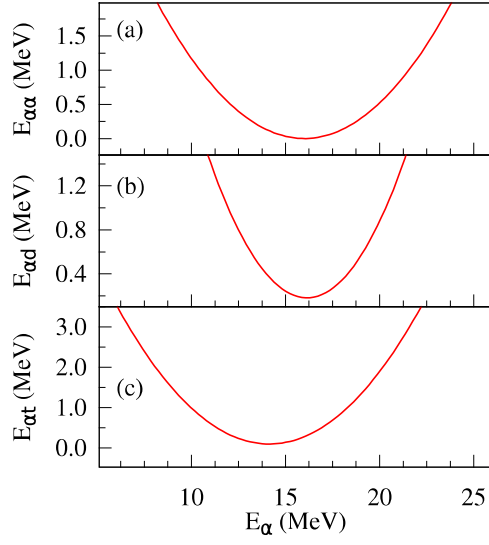
Figure 4.4: Simulated energy correlation spectra for $^7$Li on $^{93}$Nb at $E_{lab} = 28$ MeV. (a) $E_\alpha$ vs. $E_{\alpha\alpha}(^8\text{Be} \rightarrow \alpha + \alpha)$ corresponding to $\theta^{\alpha\alpha}_{rel} = 3°$. (b) $E_\alpha$ vs. $E_{\alpha d}(^6\text{Li} \rightarrow \alpha + d)$ corresponding to $\theta^{\alpha d}_{rel} = 10°$. (c) $E_\alpha$ vs. $E_{\alpha t}(^7\text{Li} \rightarrow \alpha + t)$ corresponding to $\theta^{\alpha t}_{rel} = 15°$.
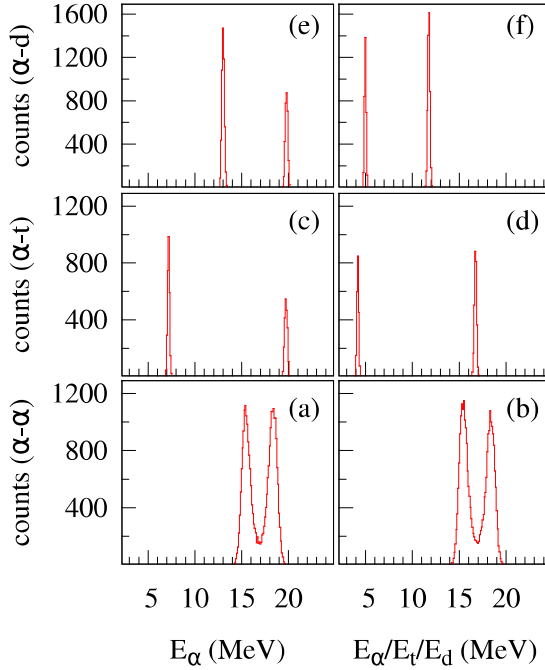


Figure 4.5: The simulated energy spectra of each of the breakup fragments for $^7$Li+$^{93}$Nb at $E_{lab} = 28$ MeV. The energy spectra of the two $\alpha$ particles due to the $1p$-pickup followed by breakup of $^8\text{Be}_{g.s.}$ are shown in (a) and (b). (c), (d) and (e), (f) correspond to the direct breakup of $^7\text{Li}_{\frac{7}{2}+}$ and $1n$-stripping followed by breakup of $^6\text{Li}_{3+}$, respectively.
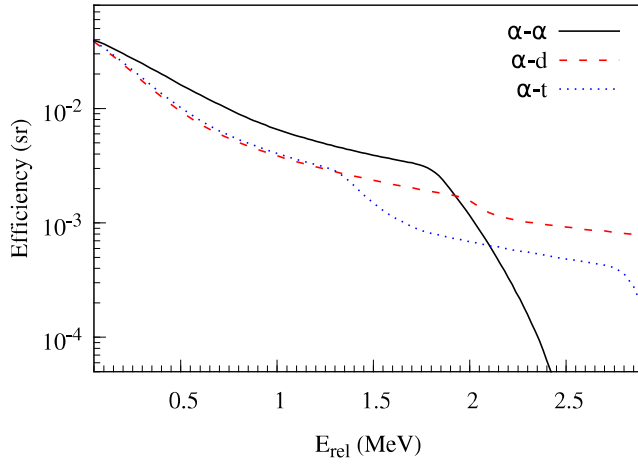
Figure 4.3: The estimated detection efficiency of $\alpha$-$\alpha$, $\alpha$-$d$ and $\alpha$-$t$ events as a function of relative energy.

fragments, correlation of relative energy and energy of individual fragment, and energy angle correlations have been reproduced considering different excited states of the target like nuclei and other parameters discussed above. The detail interpretation of the measurements for $^7$Li + $^{89}$Y, $^{93}$Nb systems has been discussed in chapter 5.

### 4.1.3   Correlated energy spectra

The simulated energy correlation spectra for various breakup processes are shown in Fig. 4.4. The relative energy between the breakup fragments are plotted as a function of energy of the outgoing $\alpha$-particle, for the the breakup of $^8$Be, $^7$Li and $^6$Li in Fig. 4.4(a), (b) and (c), respectively. For all the three cases the correlation follows a parabolic trend.

## 4.1.2   Interpretation of the measured observables

In this thesis, three types of coincidence events, $\alpha$-$\alpha$, $\alpha$-$d$ and $\alpha$-$t$ have been studied with reaction involving $^7$Li nuclei on $^{89}$Y and $^{93}$Nb targets. To explain the $\alpha$-$\alpha$ and $\alpha$-$d$ coincidence events, two step processes $1p$-pickup and $1n$-stripping reaction mechanisms followed by breakup of $^8$Be and $^6$Li have been considered, respectively. Whereas the $\alpha$-$t$ events have been reproduced from the direct breakup of $^7$Li due to inelastic excitation to the continuum and resonance states. The ground state $Q$-value ($Q_{\mathrm{gg}}$) and the breakup threshold ($E_{\mathrm{th}}$) for all the three coincidence events are tabulated in Table 4.1 for both the system. The efficiency corresponding to these events are shown in Fig. 4.3 as a function of the relative energy of the breakup fragments. The sharp fall of the efficiency is due to the insufficient energy of any one of the breakup fragments to pass through the $\Delta E$ detector.

Table 4.1: Ground state $Q$-value $Q_{\mathrm{gg}}$ and breakup threshold $E_{\mathrm{th}}^{\mathrm{BU}}$ of the different coincident events.

| Coincident events | Reaction mechanism | | $Q_{gg}$ (MeV) | $E_{\mathrm{th}}^{\mathrm{BU}}$ (MeV) |
|---|---|---|---|---|
| $\alpha$-$\alpha$ | $1p$-pickup | $^{93}$Nb($^7$Li,$^8$Be$^*$) | 11.21 | 0.0 |
| | | $^{89}$Y($^7$Li,$^8$Be$^*$) | 10.18 | |
| $\alpha$-$d$ | $1n$-stripping | $^{93}$Nb($^7$Li,$^6$Li$^*$) | -0.02 | 1.47 |
| | | $^{89}$Y($^7$Li,$^6$Li$^*$) | -0.39 | |
| $\alpha$-$t$ | inelastic excitation | $^{93}$Nb($^7$Li,$^7$Li$^*$) | 0.0 | 2.47 |
| | | $^{89}$Y($^7$Li,$^7$Li$^*$) | 0.0 | |

The measured energies of the breakup fragments corresponding to the different states of the ejectile prior to breakup have been reproduced using simulation. Details are discussed in Sec. 5.1. The measured energy correlations of breakup

### 4.1.1 Determination of normalization constant

To extract the absolute cross sections of the various breakup processes, the normalization constant $K$ is an important parameter, discussed in Sec. 2.8.3. In case of pure Rutherford scattering, the Eq. 2.12 can be simplified and value of $K$ can be estimated as

$$K = \frac{dY_{el}(\theta)}{d\Omega} \frac{sin^4(\frac{\theta}{2})}{Y_m(\theta_m)} \tag{4.1}$$

We have chosen $^7$Li+$^{209}$Bi system, for which Coulomb barrier is $\sim$30 MeV. The measurement of elastic scattering at $E_{\text{beam}}$=28 MeV can be considered as absolute Rutherford scattering in the measured angular range. The measured $\frac{dY_{el}(\theta)}{d\Omega} \frac{sin^4(\frac{\theta}{2})}{Y_m(\theta_m)}$ is plotted in Fig. 4.2. The $\chi^2$ minimised fitted value is found to be 25.3, which is the value of normalization constant $K$ for the measurement setup and used to extract absolute cross section.
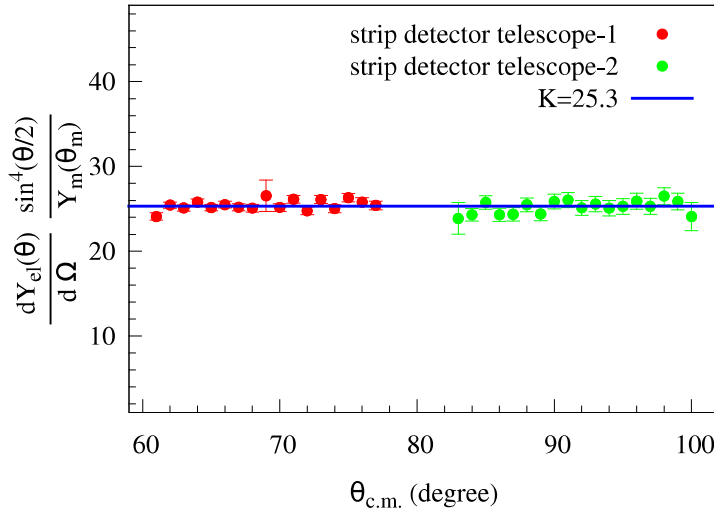


Figure 4.2: Measured ratio of elastic yields to monitor yields for $^7$Li on $^{209}$Bi at $E_{\text{beam}}$ = 28 MeV. The value of $K = 25.3$ correspond to the fitted value.
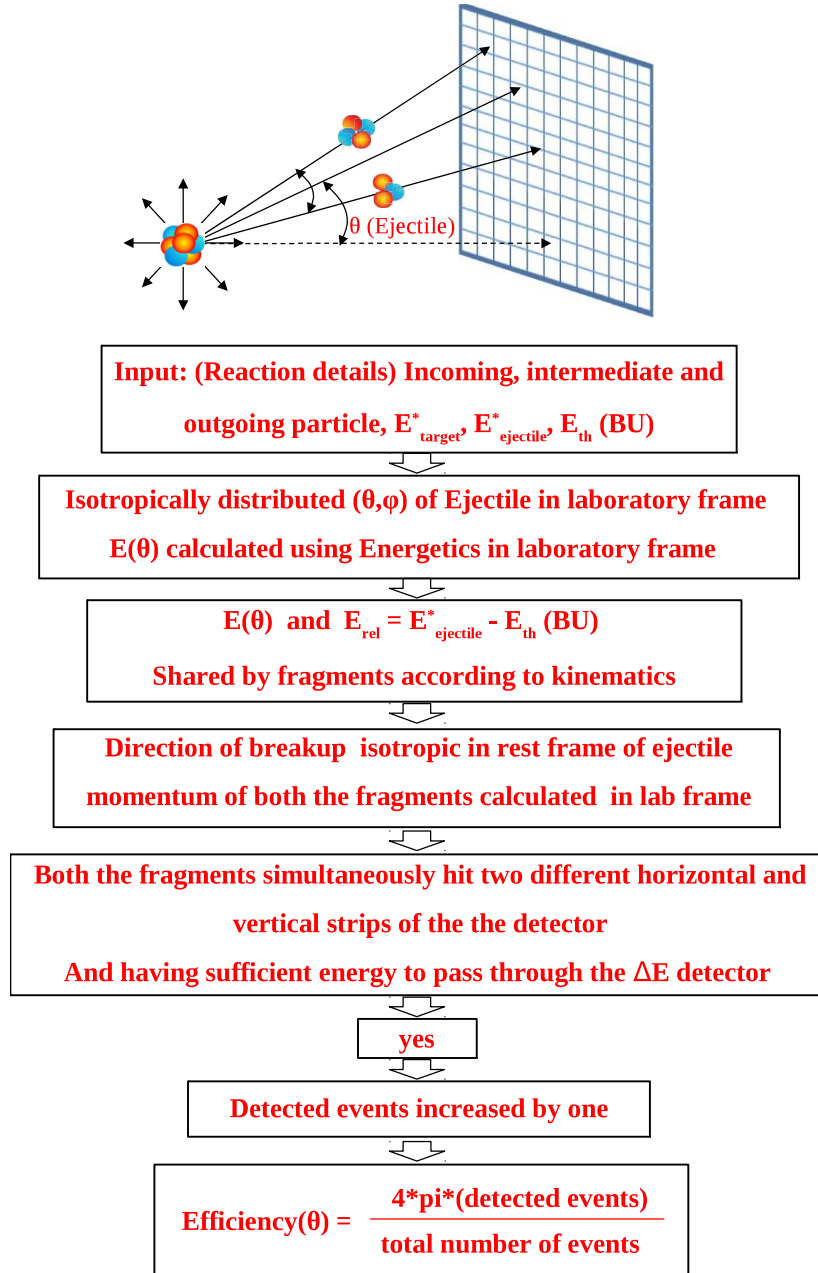
Figure 4.1: The flow chart for the simulation of 3-body kinematics using Monte Carlo technique.

two different vertical and horizontal strips of the $\Delta E$-detector and have sufficient energy to pass through. It was also confirmed that the residual energy after the loss in $\Delta E$ detector is more than the detection threshold of the $E$-detector. In the second step, it was checked whether both the fragments hit two different vertical and horizontal strips of $E$ detector. Events satisfying these conditions were considered as detectable events for estimation of the efficiency for coincident detection of the breakup fragments. Misalignment in $\Delta E$ and $E$ detector was also taken into account. The conversion of the energy and scattering angle from the laboratory frame to the c.m. frame of the target-projectile in event-by-event mode automatically takes care of the Jacobians of the transformation.

The estimated detection efficiency of different coincidence events varies due to kinematic focusing, which is found to depend on relative energy of the breakup fragments, energy of the ejectile prior to breakup, mass asymmetry of the breakup fragments, detection threshold, and geometric solid angle of the detection setup. Since energy of the ejectile prior to breakup is decided by the incident beam energy of the projectile, $Q$-value of the reaction, loss of kinetic energy due to the excitation of the ejectile as well as target like nuclei, detection efficiency is also affected by these parameters.

This code has also been used to get the efficiency for singles measurement by applying the conditions of zero breakup threshold and limiting the detection condition for a single fragment. The estimated efficiency was matching with the geometric solid angle calculated by the analytic formula.

statistical uncertainties for a limited data. In this thesis, we have also developed a Monte Carlo simulation code to interpret the observables of different breakup processes and to estimate the efficiency for coincident detection of the breakup fragments.

## 4.1 Monte Carlo simulation for coincidence efficiency using 3-body kinematics

The efficiency for the detection of fragments in coincidence was estimated using the Monte Carlo technique. The algorithm of the simulation is presented by a flow chart shown in Fig. 4.1. The scattering angle of the ejectile prior to breakup was generated by an isotropic distribution in a spherical coordinate system. The scattering angle $\theta$ and $\phi$ in centre of mass (c.m.) frame were generated by taking the cosine of a random number having values in between -1.0 to 1.0, and a random number having values in between 0.0 to $2\pi$, respectively. The scattered energy of the ejectile was calculated using kinematics taking into account the $Q$-value of the reaction and the excitation energies of the target as well as the ejectile. The coincidence efficiency depends on the velocity of the ejectile prior to breakup as well as the relative velocity of the fragments [81]. The breakup fragment emission in the rest frame of the ejectile was also considered to be isotropic. The velocities of each fragment in the rest frame of the ejectile were calculated using energy and momentum conservation laws. These velocities were added to the velocity of the ejectile prior to breakup to get their velocities in the laboratory frame. Checking of the events to be registered as 'the detected event' was carried out in two steps. In the first step, it was checked whether both the breakup fragments hit

# 4

# Simulations

In case of nuclear reactions involving three particles in the exit channel, coincidence measurements are unavoidable as discussed in chapter 2. Consequently, knowledge of accurate coincidence efficiency of the detection setup is crucial to deduce the absolute cross sections from the measured yields. Coordinate transformations and the resulting transformations of the cross sections using Jacobians are trivial and has been discussed for reactions with three particles in the exit channels by Fuchs [79]. Whereas, from an experimental point of view Monte Carlo simulation method is preferable over the Jacobians method [80]. A Monte Carlo simulation of the experiment is essential, not only to estimate the detection efficiency accurately for the extraction of cross sections, but also to account for detection threshold, energy and angular resolution of the detector, beam emittance, beam energy resolution, and multiple-scattering in a thick target foil etc. Although the results from both coordinate transformations with Jacobians and Monte Carlo method are expected to be same, it is not so obvious that the two methods lead to the same rest frame cross sections. In Ref. [80], authors show the equivalence of the two methods within

The calculated angular distributions from both CCBA and DWBA formalism along with the measured data are shown in Fig. 5.12. Although the shape of the angular distribution from both the formalism is found be similar, the estimated cross sections from CCBA calculations give better agreement with the measurements.

The $p$-stripping cross section is estimated through DWBA calculations. The entrance channel optical potentials used the global $^7$Li parameters of Ref. [88] which give a satisfactory description of the elastic scattering data. The exit channel potentials employed the global $^6$Li parameters of Ref. [88], the comparative study of Ref. [98] suggesting that for a $^{94}$Mo target at these energies the $^6$Li optical potentials should describe $^6$He elastic scattering equally well. The $\langle ^7$Li $| {}^6$He $+ p \rangle$ overlaps are calculated with the transferred $p$ bound in a Woods-Saxon well of radius $1.25 \times 6^{1/3}$ fm and diffuseness 0.65 fm with a spin-orbit term of Thomas form and depth 6 MeV, the depth of the central part being adjusted to give the correct binding energy. The spectroscopic factor is taken from Ref. [93]. The $\langle ^{94}$Mo $| {}^{93}$Nb $+ p \rangle$ overlaps are taken from the $^{93}$Nb($^3$He,$d$) study of Ref. [99] and transfers to all the $^{94}$Mo states in Table VIII of that work are included in the calculations. The estimated cross sections for $p$ stripping are $\sim 2$ mb at the incident $^7$Li energies studied here. This value will be something of a lower limit since the optimum $Q$ value for this reaction is about $-8$ MeV, favoring population of $^{94}$Mo levels at about 6.5 MeV, whereas the maximum excitation energy of the $^{94}$Mo states included in the calculations is $\sim 3$ MeV. We may estimate the actual values to be around a few mb (i.e. less than 10 mb).

agreement with the data. The calculated $0^+$ (g.s.) and $2^+$ (1.836 MeV) cross sections are shown in Fig. 5.8(a) and (b) respectively. The cumulative cross sections of $2^+$ (3.220 MeV), $1^+$ (3.488 MeV) and $2^+$ (3.634 MeV) states are compared with data in Fig. 5.8(c).

For $^7$Li + $^{93}$Nb system, the $0^+$ (g.s.), $5^-$ (2.45 MeV) and $4^-$ (2.74 MeV) states of $^{92}$Zr are included in the calculations. The spectroscopic factors for the $\langle ^{93}\text{Nb}|^{92}\text{Zr} + p\rangle$ overlaps are obtained by fitting the $^{93}$Nb($d$,$^3$He) data of Ref. [97], yielding values of C$^2$S = 1.4, 1.0 and 1.0 for the $0^+$, $5^-$ and $4^-$ states, respectively (N.B. the value of 10.8 in Ref. [97] for the $0^+$ state appears to be an error, since it is inconsistent with the data plotted on their Fig. 8). The results are compared to the data in Fig. 5.9 (b).

### 5.4.3 Distorted wave Born approximation (DWBA)

Distorted wave Born approximation (DWBA) calculations have also been performed to analyze the 1n-stripping $^{93}$Nb($^7$Li,$^6$Li*)$^{94}$Nb reactions. The cross sections have been estimated using the same optical potential and spectroscopic factors used in CCBA calculations and discussed in Sec. 5.4.2.
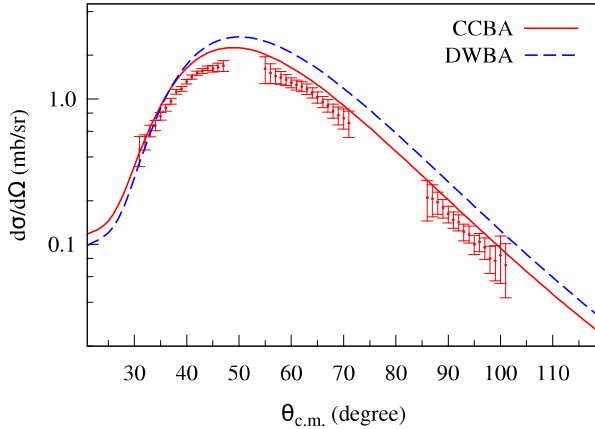


Figure 5.12: Comparison of estimated 1$n$-stripping cross sections for the $^7$Li+$^{93}$Nb system at E$_{\text{lab}}$ = 27.7 MeV from CCBA and DWBA formalisms.

of the $1_1^+$ ground state is omitted due to the very small quadrupole moment of this state. The exit channel optical potentials employed the $^6$Li global parameters of Ref. [88] with real and imaginary well depths adjusted to recover the same elastic scattering angular distributions at the appropriate energies when the $^6$Li excitations are included. Spectroscopic factors for the $\langle ^7\text{Li}|^6\text{Li} + n\rangle$, $\langle ^{89}\text{Y}|^{90}\text{Y} + n\rangle$ and $\langle ^{94}\text{Nb}|^{93}\text{Nb} + n\rangle$ overlaps are taken from Refs. [93], [94] and [95], respectively. In case of $^7$Li + $^{89}$Y system, transfers between the $^7$Li $3/2^-$ ground state and the $^6$Li $1_1^+$ and $3_1^+$ states, the $^7$Li $1/2^-$ state and the $^6$Li $1_1^+$ state, plus $2^-$ (g.s.), $3^-$ (0.203 MeV), $0^-$ (1.221 MeV), $1^-$ (1.376 MeV), $5^+$ (1.962 MeV), $6^+$ (2.245 MeV) and $2^-$ (2.475 MeV) states of $^{90}$Y are included. The cumulative cross sections of $2^-$ (g.s.) and $3^-$ (0.203 MeV) states are shown in Fig. 5.7(a) by dotted, dashed, and solid lines for energies 22.6, 27.7, and 29.7 MeV, respectively. The added cross sections of the remaining states are shown in Fig. 5.7(b). For $^7$Li + $^{93}$Nb system, a total of eight states in $^{94}$Nb (the most strongly populated according to Ref. [95]) are considered in the calculations. The results are compared to the data in Figs. 5.9(a).

Similar CCBA calculations have been performed for the $\alpha + \alpha$ coincidence data considering the $^{89}$Y($^7$Li,$^8$Be)$^{88}$Sr and $^{93}$Nb($^7$Li,$^8$Be)$^{92}$Zr $1p$-pickup processes. Entrance channel potentials are as described above. Exit channel optical potentials used $^7$Li global parameters [88] since no $^8$Be potentials are available. In case of $^7$Li + $^{89}$Y system, pickup to the 0.0 MeV $0_1^+$ resonance of $^8$Be and the $0^+$ (g.s.), $2^+$ (1.836 MeV), $2^+$ (3.220 MeV), $1^+$ (3.488 MeV) and $2^+$ (3.634 MeV) states of $^{88}$Sr are included. The spectroscopic factor for the $\langle ^8\text{Be}|^7\text{Li} + p\rangle$ overlap is taken from Ref. [93] and those for the $\langle ^{89}\text{Y}|^{88}\text{Sr} + p\rangle$ overlaps are obtained from Ref. [96]. The calculated $0^+$ (g.s.) cross sections are normalized by a factor of 0.35 to get a better

continuum bins are of width $\Delta k = 0.1$ fm$^{-1}$ with $k_{\max} = 0.8$ fm$^{-1}$ and $\alpha + t$ relative angular momenta of $L = 0$–4 and couplings up to multipolarity $\lambda = 4$ are included. The $\alpha + ^{89}$Y ($^{93}$Nb) and $t + ^{89}$Y ($^{93}$Nb) optical potentials required as input to the Watanabe-type folding potentials are taken from the global parameterizations of Refs. [86] and [87], respectively. To obtain the best fit to the elastic scattering data the real and imaginary depths of these potentials are renormalized by factors of 0.47 and 0.6, respectively for $^7$Li + $^{89}$Y system. In case of $^7$Li + $^{93}$Nb system, normalization factors of 0.6 and 0.8 are used for the real and imaginary depths, respectively. The results are compared to the elastic scattering and breakup data in Fig. 5.10 and Fig. 5.6, respectively.

## 5.4.2   Coupled channels Born approximation (CCBA)

The $\alpha + d$ coincidence data have been analyzed with CCBA calculations for the 1n-stripping $^{89}$Y($^7$Li,$^6$Li*)$^{90}$Y and $^{93}$Nb($^7$Li,$^6$Li*)$^{94}$Nb reactions. In addition to the transfer couplings, inelastic excitations of the $^7$Li($1/2^-$) and the $^6$Li($3^+_1$) excited states are included in the entrance and exit partitions, respectively. The entrance channel optical potentials are based on the global $^7$Li parameters of Ref. [88] with real and imaginary depths readjusted to fit the elastic scattering data after the inclusion of the $^7$Li couplings. The $3/2^-$(g.s.) and $1/2^-$(0.478 MeV) states of $^7$Li are treated as members of a $K = 1/2$ rotational band. The $B(E2; 3/2^- \rightarrow 1/2^-)$ is taken from Ref. [89] and the nuclear deformation length $\delta_2 = 2.4$ fm obtained by fitting the inelastic scattering data of Ref. [90]. The $^6$Li $B(E2; 1^+_1 \rightarrow 3^+_1)$ is taken from [91] and the nuclear deformation length $\delta_2 = 1.9$ fm obtained by fitting the sequential breakup data of Ref. [92]. The $^6$Li $1^+_1$ and $3^+_1$ states are assumed to be members of a $K = 1$ rotational band, with the exception that reorientation
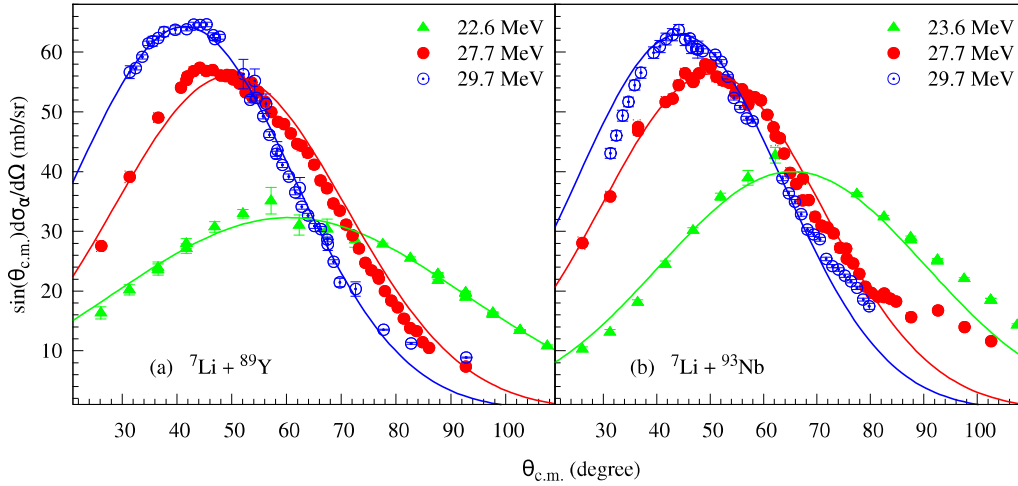
Figure 5.11: Measured angular distribution of $\alpha$-particle yield for the (a) $^7$Li+$^{89}$Y and (b) $^7$Li+$^{93}$Nb systems. The lines are corresponding to the Gaussian fit for respective energies.

$\sigma(^6\text{He}_{\text{g.s.}})$ is found to be larger than the $1p$-pickup cross section $\sigma(^8\text{Be}_{\text{g.s.}})$ by an order of magnitude.

## 5.4 Coupled channel calculations

Two sets of calculations have been performed to analyze the data. Calculations for elastic scattering and direct breakup are carried out within the CDCC formalism using the cluster folding model of $^7$Li. The CCBA formalism is employed for transfer-breakup processes, using potentials that describe the elastic scattering data. The code FRESCO [35] has been used in all cases.

### 5.4.1 Continuum-discretized coupled-channels (CDCC)

The $^7$Li $\rightarrow \alpha+t$ breakup data at $E_{\text{lab}} = 27.7$ MeV for both the system are analyzed with CDCC calculations, similar to those described in Ref. [85] except that the
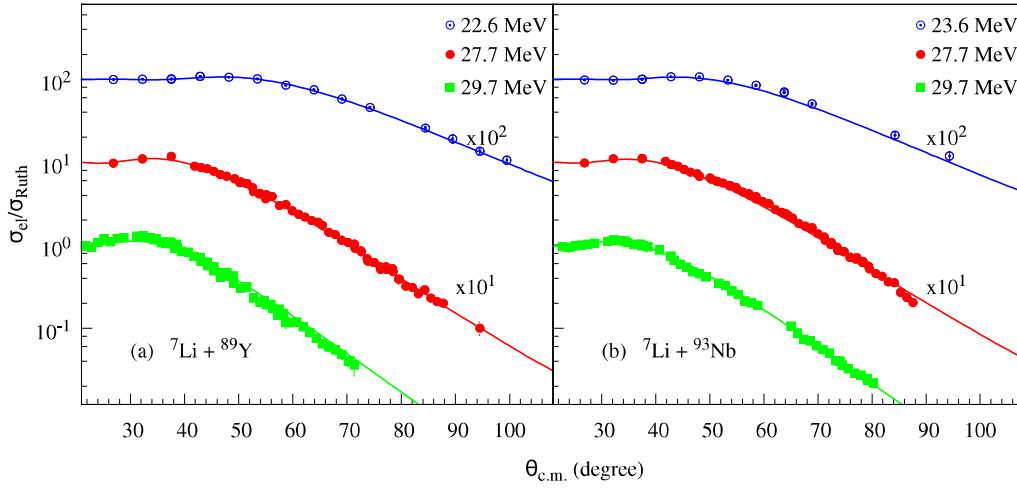
Figure 5.10: Measured elastic scattering angular distribution for the (a) $^7$Li+$^{89}$Y and (b) $^7$Li+$^{93}$Nb systems. The lines are corresponding to the CDCC calculation for respective energies.

Fig. 5.11. In this figure, the lines correspond to the Gaussian fit of the data to extract the angle integrated cross sections at respective energies. The integrated cross sections are tabulated in Table 5.1. The total exclusive cross sections for alpha production form a small fraction of the inclusive cross section, indicating that the main alpha production mechanism is due to other processes, most likely $t$-stripping/capture.

The differential cross sections of the production of $^6$He$_{g.s.}$ due to $1p$-stripping and $^6$Li$_{g.s.}$ due to $1n$-stripping have been measured. The shapes of both the cross sections are found to be bell shaped with peaks at grazing angle of the respective beam energies. The angle integrated cross sections are tabulated in  Table 5.1. The measured cross section values of $1p$-stripping reaction is found to be of similar order for both the systems.

The total $1n$-stripping cross section $\sigma(^6\text{Li}_{g.s.}) + \sigma(^6\text{Li}_{3+})$ is found to be largest among the other nucleon transfer cross sections. The $1p$-stripping cross section

kinematical matching condition [83, 84]. The total single particle strength for $(^{89}\text{Y},^{90}\text{Y})$ and $(^{93}\text{Nb},^{94}\text{Nb})$ are of same order due to the similar order of kinematical mismatch condition (optimum $Q$-value and angular momentum). Whereas, the less number of fragmented levels in $^{90}\text{Y}$ than $^{94}\text{Nb}$ nucleus, drives to more cross sections of $^{89}\text{Y}(^{7}\text{Li},^{6}\text{Li}_{3_1^+})^{90}\text{Y}$ than $^{93}\text{Nb}(^{7}\text{Li},^{6}\text{Li}_{3_1^+})^{94}\text{Nb}$ reaction for the consideration of excitation energy of the target like nuclei upto 1 MeV. The total $1n$-stripping cross sections $(\sigma(^{6}\text{Li}_{\text{g.s.}}) + \sigma(^{6}\text{Li}_{3_1^+}))$ for $^{7}\text{Li}+^{89}\text{Y}$ system is found to be $\sim$5 mb more than that for $^{7}\text{Li}+^{93}\text{Nb}$ system.

Similarly, $1p$-pickup reactions is also interesting as $^{89}\text{Y}$ has a $1p$ hole and $^{93}\text{Nb}$ has one extra proton relative to closed shell nucleus $^{90}\text{Zr}$. $1p$-pickup $(^{7}\text{Li},^{8}\text{Be}_{\text{g.s.}})$ cross sections are found to be of similar order of magnitude for both the systems for excitation energy of the target like nuclei upto 15 MeV. Which is also expected from the kinematical matching conditions. The $E^*$ $(Q - Q_{\text{opt}})$ are similar for both the systems.

## 5.3   Measured inclusive cross sections

Elastic scattering angular distributions have been measured at much above the Coulomb barrier ($\text{V}_B \approx$18 MeV) to constrain the optical model potentials, which are required for the calculations to understand the measured exclusive data. The measured elastic scattering angular distribution at different energies for $^{7}\text{Li}$ + $^{89}\text{Y},^{93}\text{Nb}$ systems are shown in Fig. 5.10(a) and (b), respectively. The plotted lines in this figure are corresponding to the CDCC calculations, details are given in Sec. 5.4.

The angular distributions of the inclusive-$\alpha$ have also been measured for both the systems $^{7}\text{Li}$ + $^{89}\text{Y},^{93}\text{Nb}$. The angular distribution of $\frac{d\sigma}{d\Omega}(\theta_{\text{c.m.}})sin(\theta_{\text{c.m.}})$ is shown

Table 5.1: Cross sections for various channels in the $^7$Li + $^{89}$Y,$^{93}$Nb systems; $\sigma_{\mathrm{cal}}$ denotes the results of CDCC ($^7$Li*(7/2$^-$)$\to \alpha + t$) and CCBA calculations for 1$n$-stripping and 1$p$-pickup reactions (see text).

| | $^7$Li+$^{89}$Y | | | | | |
|---|---|---|---|---|---|---|
| $E_{\mathrm{lab}}$ | 22.6 MeV | | 27.7 MeV | | 29.7 MeV | |
| Channel | $\sigma_{\mathrm{exp}}$ (mb) | $\sigma_{\mathrm{cal}}$ (mb) | $\sigma_{\mathrm{exp}}$ (mb) | $\sigma_{\mathrm{cal}}$ (mb) | $\sigma_{\mathrm{exp}}$ (mb) | $\sigma_{\mathrm{cal}}$ (mb) |
| $\alpha$-inclusive | $280 \pm 34$ | | $325 \pm 40$ | | $354 \pm 46$ | |
| $^8$Be$_{\mathrm{g.s.}}(\alpha+\alpha)$+$^{88}$Sr$_{\mathrm{g.s.}}$ | $0.06 \pm 0.02$ | 0.07 | $0.08 \pm 0.03$ | 0.08 | $0.10 \pm 0.03$ | 0.10 |
| $^8$Be$_{\mathrm{g.s.}}(\alpha+\alpha)$+$^{88}$Sr* ($E^* = 1.8$ MeV) | $0.28 \pm 0.03$ | 0.26 | $0.27 \pm 0.03$ | 0.29 | $0.28 \pm 0.02$ | 0.29 |
| $^8$Be$_{\mathrm{g.s.}}(\alpha+\alpha)$+$^{88}$Sr* ($2.5 \le E^* \le 5$ MeV) | $1.2 \pm 0.3$ | 1.10 | $1.3 \pm 0.3$ | 1.15 | $1.3 \pm 0.3$ | 1.16 |
| $^8$Be$_{\mathrm{g.s.}}(\alpha+\alpha)$+$^{88}$Sr* ($E^* \le 15$ MeV) | $1.8 \pm 0.4$ | | $1.9 \pm 0.5$ | | $2.0 \pm 0.4$ | |
| $^6$Li$^*_{3+}(\alpha+d)$+$^{90}$Y ($E^* \le 1$ MeV) | $9.1 \pm 0.8$ | 8.1 | $9.8 \pm 0.9$ | 9.0 | $10.3 \pm 1.0$ | 9.2 |
| $^6$Li$^*_{3+}(\alpha+d)$+$^{90}$Y ($E^* \le 4$ MeV) | | 11.1 | $14.6 \pm 1.3$ | 13.9 | $15.6 \pm 1.5$ | 14.4 |
| $^6$Li$_{\mathrm{g.s.}}$+$^{90}$Y | | 18.6 | $15.6 \pm 1.4$ | 17.0 | $16.1 \pm 1.7$ | 16.5 |
| $^7$Li$_{\frac{7}{2}^-}$+$^{89}$Y | | | $3.5 \pm 0.3$ | 3.9 | | |
| $^6$He$_{\mathrm{g.s.}}$+$^{90}$Zr | | | $7.8 \pm 1.0$ | | $9.4 \pm 1.2$ | |
| $\sigma$-reaction | | 856 | | 1252 | | 1368 |
| | $^7$Li+$^{93}$Nb | | | | | |
| Lab energy | 23.6 MeV | | 27.7 MeV | | 29.7 MeV | |
| Channel | $\sigma_{\mathrm{exp}}$ (mb) | $\sigma_{\mathrm{cal}}$ (mb) | $\sigma_{\mathrm{exp}}$ (mb) | $\sigma_{\mathrm{cal}}$ (mb) | $\sigma_{\mathrm{exp}}$ (mb) | $\sigma_{\mathrm{cal}}$ (mb) |
| $\alpha$-inclusive | $273 \pm 40$ | | $321 \pm 48$ | | $340 \pm 52$ | |
| $^8$Be$_{\mathrm{g.s.}}(\alpha+\alpha)$+$^{92}$Zr* ($E^* \le 3$ MeV) | $0.5 \pm 0.1$ | 0.36 | $0.7 \pm 0.1$ | 0.56 | $0.6 \pm 0.1$ | 0.53 |
| $^8$Be$_{\mathrm{g.s.}}(\alpha+\alpha)$+$^{92}$Zr* ($E^* \le 15$ MeV) | $1.5 \pm 0.2$ | | $2.0 \pm 0.3$ | | $2.3 \pm 0.3$ | |
| $^6$Li$^*_{3+}(\alpha+d)$+$^{94}$Nb ($E^* \le 1$ MeV) | $5.2 \pm 0.5$ | 5.5 | $5.8 \pm 0.4$ | 6.2 | $6.2 \pm 0.4$ | 6.2 |
| $^6$Li$^*_{3+}(\alpha+d)$+$^{94}$Nb ($E^* \le 4$ MeV) | $9.8 \pm 1.1$ | | $13.8 \pm 1.4$ | | $14.7 \pm 1.4$ | |
| $^6$Li$_{\mathrm{g.s.}}$+$^{94}$Nb | $9.9 \pm 1.0$ | 9.8 | $11.0 \pm 1.2$ | 10.9 | $11.2 \pm 1.5$ | 10.3 |
| $^7$Li$_{\frac{7}{2}^-}$+$^{93}$Nb | | | $3.3 \pm 0.6$ | 2.9 | | |
| $^6$He$_{\mathrm{g.s.}}$+$^{94}$Mo | | | $7.2 \pm 0.9$ | | $8.6 \pm 1.0$ | |
| $\sigma$-reaction | | 1121 | | 1310 | | 1489 |
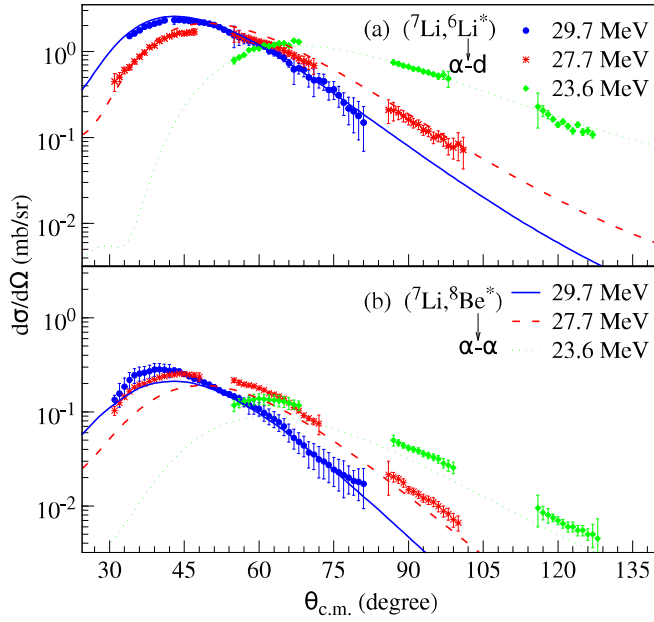
Figure 5.9: 1$n$-stripping and 1$p$-pickup cross sections for the $^7$Li+$^{93}$Nb system at 23.6, 27.7 and 29.7 MeV. (a) The $\alpha + d$ cross sections for the ($^7$Li,$^6$Li($3_1^+$)) reaction. (b) The $\alpha + \alpha$ cross sections for the ($^7$Li,$^8$Be($0_1^+$)) reaction. In both panels the dotted, solid and dashed lines correspond to the CCBA calculations at 23.6, 27.7 and 29.7, respectively.

tions for $\alpha+d$ events from the breakup of $^6$Li formed after 1$n$-stripping are larger than those for $\alpha+t$ events from the resonant breakup of $^7$Li. These results show the dominance of the $n$-stripping followed by breakup over the direct breakup of $^7$Li from the $\frac{7}{2}^+$ resonance state, in agreement with the results reported in earlier studies with $^7$Li+$^{65}$Cu system [23].

A comparative study of 1$n$-stripping reactions for $^7$Li+$^{89}$Y and $^7$Li+$^{93}$Nb systems is expected to be interesting as $^{89}$Y ($N$=50) is neutron closed nuclei and $^{93}$Nb ($N$=52) has two valance neutron. As shown in Table 5.1, the measured 1$n$-stripping ($^7$Li,$^6$Li$_{3_1^+}$) cross sections for the $^7$Li+$^{89}$Y reaction are found to be about ~2 times compared to that of $^7$Li+$^{93}$Nb reaction for excitation energy of the target like nuclei upto 1 MeV. However, after the consideration of the full excitation energy spectra of the target like nuclei, the cross sections are of similar order of magnitude for both the systems. This obsevation could be understood from the
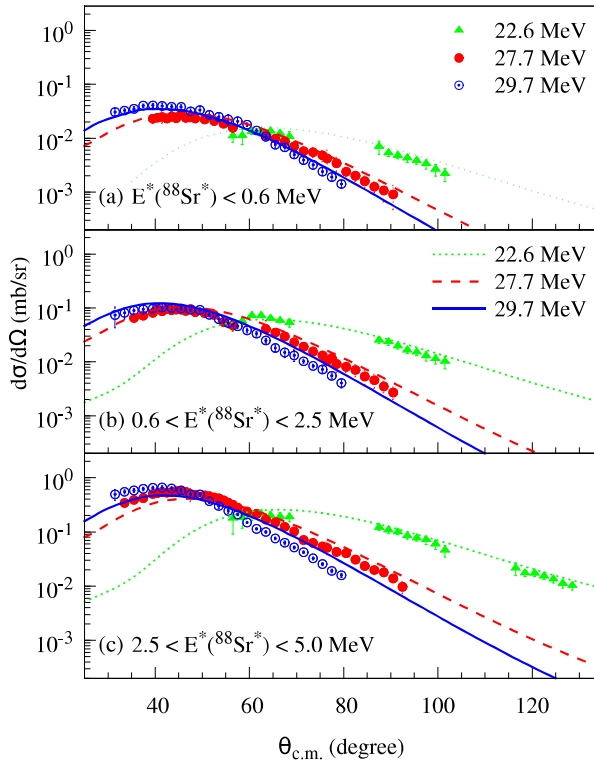
Figure 5.8: Cross sections of $1p$-pickup $^{89}Y(^{7}Li,^{8}Be)^{88}Sr^*$ channel at 22.6, 27.7 and 29.7 MeV. Panels (a), (b) and (c) are corresponding to the excitation energy of $^{88}Sr$ $E^* \leq 0.6$ MeV, $0.6 \leq E^* \leq 2.5$ MeV, and $2.5 \leq E^* \leq 5.0$ MeV, respectively. The CCBA calculations are presented by dotted, dashed, and solid lines for 22.6, 27.7, and 29.7 MeV energies, respectively.

energies up to 3.0 MeV, as information on the spectroscopic factors is available only in this energy range [50].

The measured angular distributions for both the reactions $1n$-stripping followed by breakup of $^{6}Li_{3_1^+}$ and $1p$-pickup followed by breakup of $^{8}Be_{g.s.}$ are bell shaped with peaks at the respective grazing angles for the different beam energies. A comparisons of cross sections for $^{7}Li + {}^{89}Y,^{93}Nb$ systems are presented in Table 5.1. Integrated cross sections listed in that table are obtained assuming a Gaussian shape of the angular distribution. The errors on the data points are due to statistics and the fitting of the angular distribution while obtaining the integrated cross section. For both the system, the cross sections for $1p$-pickup (with a large positive $Q_{gg}$) are smaller than those for $1n$-stripping at all energies, which could be attributed to poor kinematical matching [83]. The differential cross sec-
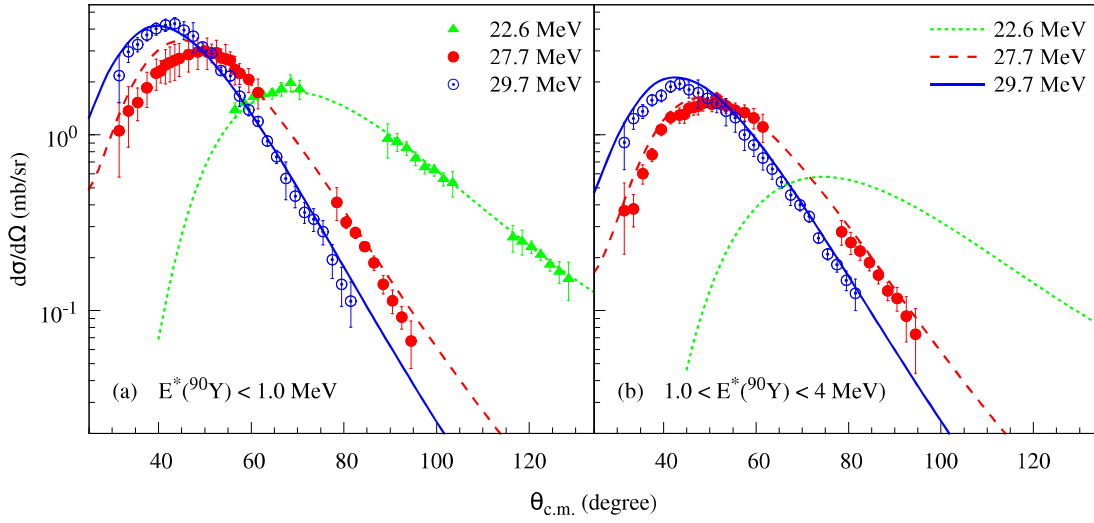
Figure 5.7: Cross sections for the 1$n$-stripping $^{89}$Y($^7$Li,$^6$Li*)$^{90}$Y* reaction at 22.6, 27.7 and 29.7 MeV. (a) Excitation energy of $^{90}$Y up to 1.0 MeV is shown. (b) Corresponding to the excitation energy of $^{90}$Y 1.0≤ $E^*$ ≤4.0 MeV. In both panels the dotted, dashed, and solid lines correspond to the CCBA calculations at energies 22.6, 27.7 and 29.7 MeV, respectively.

$^{88}$Sr, which is populated due to 1$p$-pickup $^{89}$Y($^7$Li,$^8$Be)$^{88}$Sr* reaction (Fig. 5.5(a)). The two low energy peaks are corresponding to the g.s. and 1$^{st}$ excited state of $^{88}$Sr. The higher energy peak is the admixture of the other excited states. The angular distribution of 1$p$-pickup leading to the $^8$Be(g.s.) are shown in Fig. 5.8(a), (b), (c) for the three range of excitation energy of $^{88}$Sr.

In case of $^7$Li+$^{93}$Nb system, due to the closely spaced states in $^{94}$Nb and $^{92}$Zr, the different excited states are not resolved in the measured excitation energy spectra as shown in Fig. 5.5(d) and (e). The 1$n$-stripping cross sections for $\alpha$+$d$ breakup events from the $^6$Li 3$^+_1$ (2.18 MeV) state are shown in Fig. 5.9(a). Excited states of $^{94}$Nb up to 1.0 MeV are considered due to lack of knowledge of spectroscopic factors beyond this energy. The cross sections of 1$p$-pickup leading to the $^8$Be(g.s.) are shown in Fig. 5.9(b). These data are restricted to $^{92}$Zr excitation
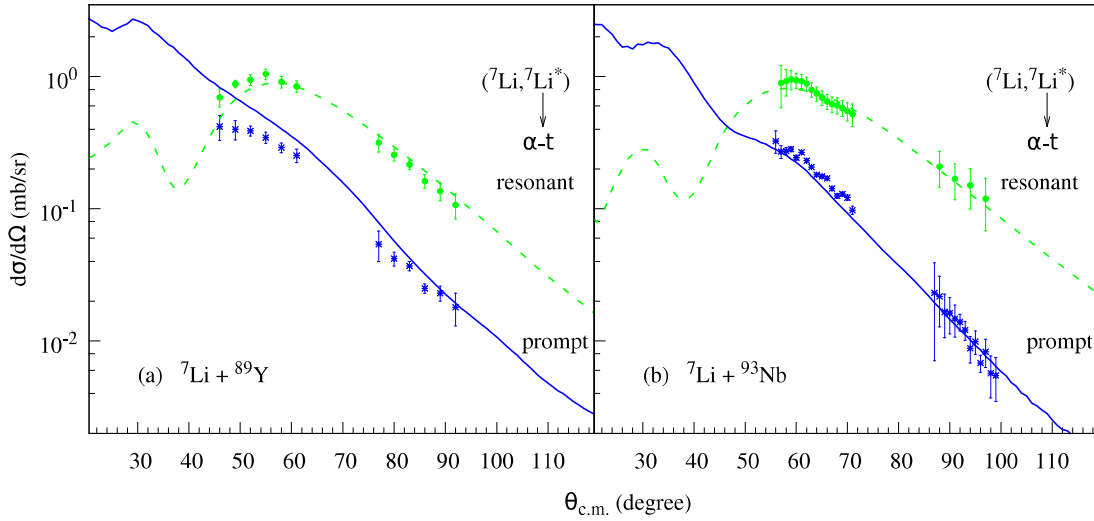
Figure 5.6: Prompt and resonant (from the $7/2^-$ state) breakup of $^7$Li, shown as asterisks and filled circles, respectively for (a) $^7$Li+$^{93}$Nb and (b) $^7$Li+$^{89}$Y systems at $E_{\text{lab}}$ = 27.7 MeV. The CDCC results for prompt and resonant breakup are denoted by solid and dashed lines, respectively.

the system and are found to be order of magnitude smaller than the resonant breakup. The angle integrated cross sections obtained assuming a Gaussian shape for resonant breakup are $3.5 \pm 0.5$ mb and $3.3 \pm 0.6$ mb for $^7$Li+$^{89}$Y and $^7$Li+$^{93}$Nb systems, respectively. The cross sections for prompt breakup are not quoted here as the peak positions are not known from the present measurement.

In case of $1n$-stripping $^{90}$Y($^7$Li,$^6$Li*)$^{90}$Y* reaction, the cross sections for $\alpha + d$ breakup events from the $^6$Li $3_1^+$ (2.18 MeV) state are extracted. In the excitation energy spectra of $^{90}$Y, as shown in Fig. 5.5(b), two distinct peaks are observed. The low energy peak is expected to be an admixture of the g.s. $(2^-)$ and $1^{st}$ excited state $(3^-)$. The extracted cross sections shown in Fig. 5.7 (a) and (b) are corresponding to the excitation energy $E^* \leq 1.0$ MeV and $1.0 \leq E^* \leq 4.0$ MeV, respectively. The angle integrated cross sections are tabulated in Table 5.1.

Three distinct peaks are found in the measured excitation energy spectra of
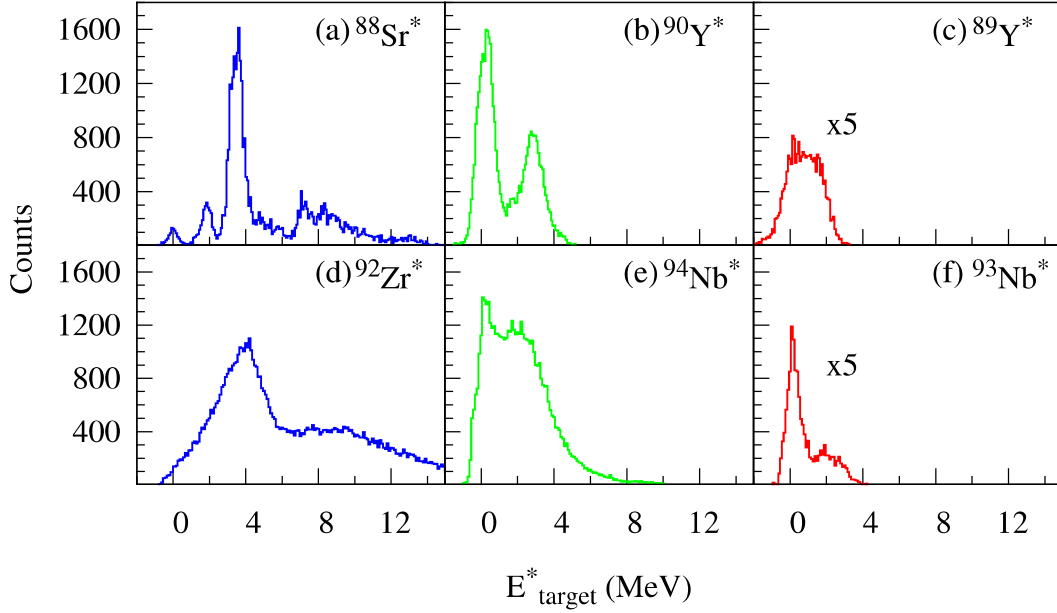
Figure 5.5: Measured excitation energy spectra of target like products for $^7$Li+$^{89}$Y, $^{93}$Nb reactions at energy $E_{\text{lab}}$ = 27.7 MeV. The excitation energy spectra of $^{88}$Sr ($^{92}$Zr), $^{90}$Y ($^{94}$Nb), and $^{89}$Y ($^{93}$Nb) nuclei populated due to 1$p$-pickup, 1$n$-stripping, and inelastic excitation reactions, respectively, are presented.

## 5.2   Measured exclusive cross sections

The angular distribution of $^7$Li* $\rightarrow \alpha + t$ breakup via the $\frac{7}{2}^-$ state (resonant breakup) and the continuum (prompt breakup) below this resonance for $^7$Li + $^{89}$Y, $^{93}$Nb systems at energy $E_{\text{lab}}$ = 27.7 MeV are shown in Fig. 5.6. The errors on the data points are due to statistics.

The cross section of breakup from 7/2$^-$ resonance state, as shown in Fig. 5.6 (a), has a peak around ∼55° for $^7$Li+$^{89}$Y system. Whereas, in case of $^7$Li+$^{93}$Nb system, there is an indication that, the angular distribution has a maximum around ∼60°, which is expected from the grazing angle concept. In case of prompt breakup ($E_{\text{rel}}$ < 1.7 MeV), no peak is observed in the measured angular range for both

The correlation plot of the measured energy of $\alpha$-particle $E_\alpha$ vs. the relative energy $E_{\alpha t}$ spectrum is shown in Fig. 5.4(a) for $\theta_{\mathrm{rel}} = 15°$. The corresponding projections of the $\alpha$-particle energy are denoted by the shaded area in Fig. 5.4(b). In this case, only the high energy $\alpha$ events could be detected. The low energy $\alpha$ particles are stopped in the $\Delta E$ ($\sim$50 $\mu$m) detectors. The arrow on the x-axis indicates the detection threshold of $\alpha$-particle energy in case of $\Delta E$ detector of thickness 50 $\mu$m. The simulated kinematical curves corresponding to excitation energy $E^\star(^{93}\mathrm{Nb}) = 0$, 1, and 2 MeV shown as dashed, solid, and dotted lines, respectively in Fig. 5.4(a) well explained the data.

### 5.1.4 Measured excitation energy of target like nuclei

The excitation energy of the target-like nuclei is determined using the missing energy technique. The measured excitation energy of the target-like nuclei $^{88}\mathrm{Sr}$, $^{90}\mathrm{Y}$, and $^{89}\mathrm{Y}$ produced due to 1$p$-pickup, 1$n$-stripping, and inelastic excitation in $^7\mathrm{Li} + ^{89}\mathrm{Y}$ reaction at $E_{\mathrm{lab}} = 27.7$ MeV and $\theta_{\mathrm{lab}} = 60°$ are presented in Fig. 5.5 (a), (b), and (c), respectively.

In case of $^7\mathrm{Li} + ^{93}\mathrm{Nb}$ system, 1$p$-pickup, 1$n$-stripping, and inelastic excitation lead to target like nuclei $^{92}\mathrm{Zr}$, $^{94}\mathrm{Nb}$, and $^{93}\mathrm{Nb}$ nuclei, respectively. The excitation energy spectra of $^{92}\mathrm{Zr}$, $^{94}\mathrm{Nb}$, and $^{93}\mathrm{Nb}$ nuclei are shown in Fig. 5.5 (d), (e), and (f), respectively. For transfer reactions, the excitation energy of the target like nuclei should peak around $E^* = Q_{\mathrm{gg}} - Q_{\mathrm{opt}}$, according to the semi-classical theory [83, 84]. Here $Q_{\mathrm{gg}}$ and $Q_{\mathrm{opt}}$ are the ground state and optimum $Q$-values, respectively. For 1p-pickup $E^*(^{92}\mathrm{Zr})$ and $E^*(^{88}\mathrm{Sr})$ peak $\sim$3.5 MeV and for 1n-stripping $E^*(^{94}\mathrm{Nb})$ and $E^*(^{90}\mathrm{Y})$ peak $\sim$0.0 MeV, following the semi-classical theory.

energy $E^\star(^{94}\mathrm{Nb}) = 0.0$, 0.5, and 1.0 MeV are plotted as dashed, solid, and dotted lines, respectively in Fig. 5.3(a). The yields corresponding to the high and low energy $\alpha$ particle are found to be asymmetric. The observed asymmetry has been reproduced by the simulation and consequently consistent cross sections for the high and low energy $\alpha$-particles have been obtained.

### 5.1.3 $\alpha$-$t$ coincidence events

Direct inelastic excitation of $^{7}\mathrm{Li}^*$ followed by breakup to $\alpha$-$t$ events are also seen. From the efficiency corrected $E_{\mathrm{rel}}$ spectrum, as shown in in Fig. 5.2(b), the prominent peak at $E_{\mathrm{rel}} = 2.16$ MeV reveals that, breakup of $^{7}\mathrm{Li}$ is mostly occurring from the resonance state $\frac{7}{2}^-$ (4.63 MeV) state. The maximum possible relative angle between $\alpha$ and $t$-particles for $^{93}\mathrm{Nb}(^{7}\mathrm{Li},^{7}\mathrm{Li}^*_{\frac{7}{2}^-} \to \alpha + t)$ is $\sim 26°$ at energy $E_{\mathrm{lab}} = 27.7$ MeV.
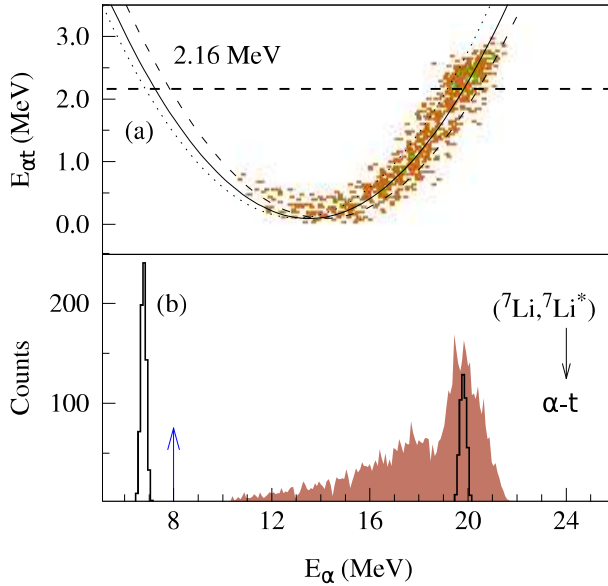


Figure 5.4: Measured energy correlation spectra of $\alpha$-$t$ for $^{7}\mathrm{Li}$ on $^{93}\mathrm{Nb}$ at $E_{\mathrm{lab}} = 27.7$ MeV and $\theta_{\mathrm{lab}} = 60°$. (a) $E_\alpha$ vs. $E_{\alpha t}$ corresponding to $\theta^{\alpha t}_{\mathrm{rel}} = 15°$. The kinematical curves plotted as dashed, solid and dotted lines correspond to $E^\star(^{93}\mathrm{Nb}) = 0$, 1, and 2 MeV. (b) The shaded distributions correspond to projections of the $\alpha$-particle energy for the data in (a). $E_\alpha$ resulting from Monte Carlo simulations is shown as solid line (see text for details).

$^6$Li is also observed in $^7$Li on $^{93}$Nb system. The peak at 710 keV in the $E_{rel}$ spectra of $\alpha$-$d$ as shown in Fig. 5.2 confirms the breakup of $^6$Li from $3^+$ (2.16 MeV) state. The breakup threshold $E_{th}$ of $^6$Li$^* \rightarrow \alpha + d$ reaction is 1.47 MeV. The maximum possible relative angle between $\alpha$ and $d$-particles for $^{93}$Nb($^7$Li,$^6$Li$^*_{3^+} \rightarrow \alpha+d$) is $\sim 22°$ at $E_{lab} = 27.7$ MeV. The measured energy of $\alpha$-particle $E_\alpha$ vs. the relative energy $E_{\alpha d}$ spectrum is shown in Fig. 5.3(a) for $^7$Li+$^{93}$Nb system corresponding to $\theta_{rel} = 10°$ at energy $E_{lab} = 27.7$ MeV and the center of the detector at $\theta_{lab} = 60°$. The corresponding projections of the $\alpha$-particle energy are denoted by the shaded area in Fig. 5.3(b).
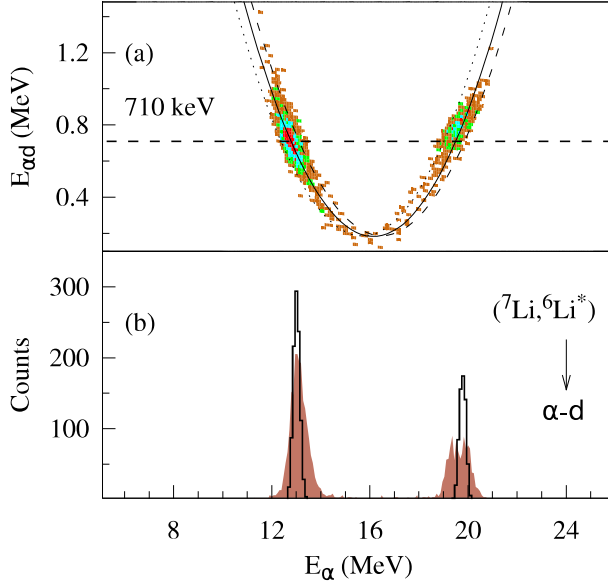


Figure 5.3: Measured energy correlation spectra of $\alpha$-$d$ for $^7$Li on $^{93}$Nb at $E_{lab} = 28$ MeV and $\theta_{lab} = 60°$. (a) $E_\alpha$ vs. $E_{\alpha d}$ corresponding to $\theta^{\alpha d}_{rel} = 10°$. The kinematical curves plotted as dashed, solid and dotted lines correspond to $E^*(^{94}$Nb$) = 0.0$, 0.5, and 1.0 MeV. (b) The shaded distributions correspond to projections of the $\alpha$-particle energy for the data in (a). $E_\alpha$ resulting from Monte Carlo simulations is shown as solid line (see text for details).

The measured spectra shown in Fig. 5.3 are understood using the Monte Carlo simulation. Considering the relative energy distributions as a Gaussian centered at 710 keV, simulated energy of $\alpha$-particles shown as histogram in Fig. 5.3(b) well explained the data. The simulated kinematical curves corresponding to excitation
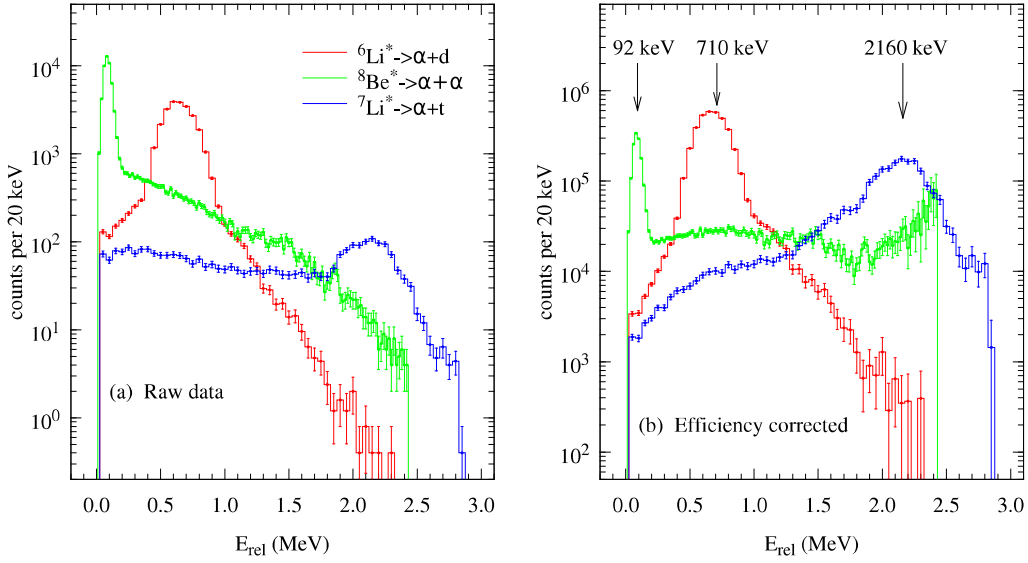
Figure 5.2: (a) The extracted relative energy spectra, (b) efficiency corrected relative energy spectra of $\alpha$-$\alpha$, $\alpha$-$d$ and $\alpha$-$t$ for the $^7$Li+$^{93}$Nb system at $E_{\mathrm{lab}} = 27.7$ MeV and $\theta_{\mathrm{lab}} = 60°$.

tion. For the simulation of $^8$Be$_{\mathrm{g.s.}}$ breakup into two $\alpha$-particles, the relative energy distribution is considered as Gaussian centered at 92 keV. The kinematical curves plotted as dashed, solid and dotted lines in Fig. 5.1 (a) correspond to $E^\star(^{92}\mathrm{Zr}) = 1$, 3, and 5 MeV. The yields corresponding to the high and low energy $\alpha$ particle are found to be symmetric for $\alpha$-$\alpha$ breakup as expected from the simulation.

## 5.1.2 $\alpha$-$d$ coincidence events

The presence of the two step process can be seen from Fig. 2.13(b) which shows the $\alpha + d$ coincidences for the $^7$Li+$^{89}$Y system. Two clear peaks are seen in the deuteron vs. alpha energy correlation plot, indicating a breakup of $^6$Li formed after one neutron stripping ($Q = $ -0.39 MeV) of $^7$Li and clearly not the direct breakup of $^7$Li into $\alpha + d + n$ ($Q = -8.73$ MeV). The 1$n$-stripping followed by breakup of
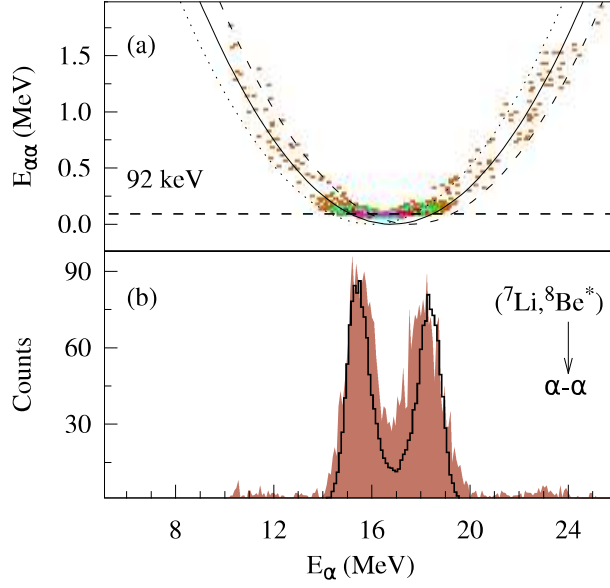
Figure 5.1: Measured energy correlation spectra of $\alpha$-$\alpha$ for $^7$Li on $^{93}$Nb at $E_{\text{lab}} = 27.7$ MeV and $\theta_{\text{lab}} = 60°$. (a) $E_\alpha$ vs. $E_{\alpha\alpha}$ corresponding to $\theta_{\text{rel}}^{\alpha\alpha} = 3°$. The kinematical curves plotted as dashed, solid and dotted lines correspond to $E^\star(^{92}\text{Zr}) = 1$, 3, and 5 MeV. (b) The shaded distributions correspond to projections of the $\alpha$-particle energy for the data in (a). $E_\alpha$ resulting from Monte Carlo simulations is shown as solid line (see text for details).

to $\alpha$-particles moving in the forward and backward direction in the rest frame of the $^8$Be prior to breakup. It is apparent from Fig. 4.6 that the difference between energies of the forward and backward moving fragments reduces as the relative angle between them increases. For this reason the two distinct peaks observed in the Fig. 5.1 (b), merge into a single peak for $\theta_{\text{rel}} \geq 5°$ in the present measurement.

The measured relative energy spectra for $\alpha$-$\alpha$ events is shown in Fig. 5.2(a) by green histogram. It has been shown in Sec. 4.1.2, that detection efficiency is highly dependent on the relative energy of the breakup fragments. The relative energy spectra after efficiency correction is plotted in Fig. 5.2(b). The rising trend in the spectrum peak above the $E_{\text{rel}} = 2.0$ MeV is a part of the $2^+$ ($E^* = 3.0$ MeV) state [82].

The measured observables kinetic energy, relative energy, $Q$-value of the reactions etc for each coincident event are interpreted using the Monte Carlo simula-

# 5.1   Correlation spectra of breakup fragments

The results obtained from the measurements of breakup fragments in coincidence are reported in this section. The experimental details are discussed in chapter 2. In the exclusive measurement three types of coincident events $\alpha$-$\alpha$, $\alpha$-$d$ and $\alpha$-$t$ are observed. The $\alpha$-$\alpha$ event rate is found to be highest and that for $\alpha$-$t$ is lowest. The reaction mechanisms, which are responsible for those coincident events, are identified and understood from correlation spectra, relative energy of the fragments and excitation energy of the target like nuclei.

## 5.1.1   $\alpha$-$\alpha$ coincidence events

The occurrence of the two step process can be seen from the measured energy correlation spectra of $\alpha$-$\alpha$ events for $^{7}$Li+$^{89}$Y system shown in Fig. 2.13(a). The correlation plots indicate that, the source of the $\alpha$-$\alpha$ events is due to the breakup of $^{8}$Be, which could be formed after $1p$-pickup. To identify the mechanism of $1p$-pickup followed by breakup of $^{8}$Be, the energy of any of the $\alpha$ particle $E_{\alpha}$ vs. the relative energy $E_{\alpha\alpha}$ is plotted and shown in Fig. 5.1(a) for $^{7}$Li+$^{93}$Nb system at energy $E_{\text{lab}} = 27.7$ MeV and with the center of the detector at $\theta_{\text{lab}} = 60°$. Most of the events are localized to $E_{\text{rel}} = 92$ keV, indicating the breakup of $^{8}$Be from ground state. The breakup threshold of $^{8}$Be$^{*} \rightarrow \alpha + \alpha$ is zero but the $Q$-value is 92 keV, which is emerging out as relative energy. The maximum possible relative angle between the two $\alpha$-particles for $^{93}$Nb($^{7}$Li,$^{8}$Be$_{\text{g.s.}} \rightarrow \alpha + \alpha$) is $\sim 8°$ at $E_{\text{lab}} = 27.7$ MeV. The data shown in Fig. 5.1 correspond to $\theta_{\text{rel}} = 3°$. The projections of the $\alpha$-particle spectrum of Fig. 5.1 (a) is shown as the shaded areas in Fig. 5.1 (b). The two peaks at high and low energy in the $E_{\alpha}$ spectra in Fig. 5.1 (b) are due

# 5

# Breakup and transfer-breakup reactions

The two step processes, inelastic excitation followed by breakup and nucleon transfer followed by breakup of the ejectile are the topic of current interest. In case of reaction involving weakly bound nuclei these processes play a key role on elastic scattering as well as fusion reactions. The two step mechanisms, namely direct breakup and transfer-breakup are studied using coincidence measurements together with coupled channels calculations. In this chapter, we will discuss the above mentioned mechanisms for $^7$Li$+^{89}$Y, $^{93}$Nb systems. The exclusive cross sections of different breakup mechanism $1p$ pickup followed by breakup ($^8$Be$^* \rightarrow \alpha+\alpha$), $1n$ stripping followed by breakup ($^6$Li$^* \rightarrow \alpha + d$) along with inelastic excitation followed by breakup ($^7$Li$^* \rightarrow \alpha + t$) are reported. The angular distribution of elastic and inclusive-$\alpha$ along with the cross sections of $1n$- $1p$-stripping leading to $^6$Li$_{g.s.}$ and $^6$He$_{g.s.}$ are presented. Coupled channels Born approximation and continuum discretized coupled channels calculations, carried out to understand the large number of observables, are also reported.

This conclusion also agrees with the direct stripping calculations discussed in Sec. 5.4.3. Although, estimation of the $d$-stripping cross section is not possible in the DWBA formalism due to the lack of suitable nuclear structure information concerning the $\langle ^{95}\text{Mo} \mid ^{93}\text{Nb} + d \rangle$ overlaps. The estimated $p$-stripping cross section is less than 10 mb agrees with the measurement (see Table 5.1). The $d$- and $t$-stripping cross sections are expected to be smaller than that for $p$ stripping, from the semi-classical trajectory matching conditions. Thus, neither process is expected to contribute significantly to the observed Mo residue cross sections. Breakup of $^7$Li followed by capture of the $t$ is the main mechanism for the $t$-capture reaction.

function of excitation energy ($E^*$) of the composite system $^{96}$Mo. The calculated $E^*$ and the corresponding breakup fusion cross section as a function of spin ($\sigma(J)$ vs. $J$) have been given as input to the statistical model code PACE for the calculation of the evaporation residue cross sections from decay of $^{96}$Mo formed after $t$-fusion. The calculated cross sections of $^{94,95}$Mo residues are plotted as solid and dashed curves in Fig. 6.12(a), respectively. In a similar way, the cross sections of $^{95,96}$Tc, which are populated in $\alpha$-capture reactions are also estimated and shown in Fig. 6.12(b) by dashed and solid lines, respectively.
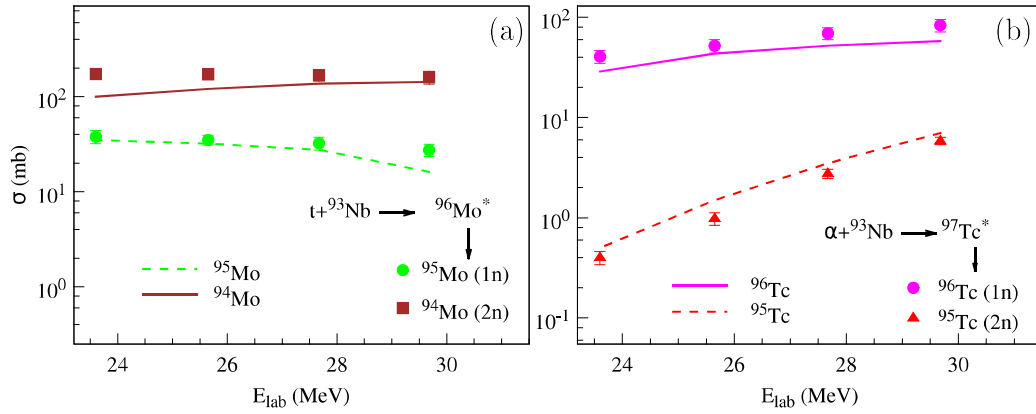


Figure 6.12: The cross sections of (a) $^{94,95}$Mo and (b) $^{95,96}$Tc nuclei populated due to $t$-capture followed by $1n$, $2n$ evaporation and $\alpha$-capture followed by $1n$, $2n$ evaporation channels are shown, respectively. The solid lines represent the estimated cross sections for those nuclei using the codes PLATYPUS and PACE.

The energy dependence of formation of the residues $^{94,95}$Mo and $^{95,96}$Tc agrees well with the dynamical model calculations combined with statistical model estimation. The simultaneous description of breakup, complete fusion, $t$-capture, $\alpha$-capture, and the individual residue ($^{94,95}$Mo and $^{96}$Tc) cross sections from the dynamical reaction model with stochastic breakup indicates the dominance of two step breakup fusion mechanism over the one step stripping reaction.

## 6.10   Breakup-fusion vs direct cluster stripping

The excitation energy $E^*$ of the composite system $^{94-96}$Mo and $^{97}$Tc, due to the capture of $p$, $d$, $t$, and $\alpha$ by $^{93}$Nb, have been listed in Table 6.5. The estimated $E^*$ of composite system for direct stripping and breakup followed by fusion reactions are given. As apparent from Table 6.5, the formation of composite system via both the processes, direct stripping and breakup followed by fusion, lead to similar excitation energies. Hence, only the residues cross sections are not sufficient to allude on the capture mechanisms.

Table 6.5: Excitation energies $E^*$ of the composite systems due to the capture of $p$, $d$, $t$, and $\alpha$ for $^7$Li+$^{93}$Nb system at lab energy 28 MeV. The $E^*$ are given for both the possible reaction mechanism, namely, direct stripping and breakup followed by fusion (ICF).

| Captured particle | Composite system | $E^*_{\text{stripping}}$ (MeV) | $E^*_{\text{ICF}}$ (MeV) |
|---|---|---|---|
| $\alpha$ | $^{97}$Tc | 16.9 | 17.0 |
| $t$ | $^{96}$Mo | 22.3 | 27.4 |
| $d$ | $^{95}$Mo | 12.3 | 18.9 |
| $p$ | $^{94}$Mo | 6.8 | 11.1 |

To get further insight into the mechanism of fragment capture, the measured cross sections of the residues $^{94,95}$Mo have been compared with the predictions of the statistical model calculations (PACE) for $t$-capture followed by $1n$ and $2n$ evaporation channels, using the angular momentum distribution and excitation energy of the primary composite system obtained from PLATYPUS, as discussed in Ref. [30]. The energy spectrum of the outgoing $\alpha$-particles, after capture of the complementary fragment ($t$), represents the cross section for breakup fusion as a function of the kinetic energy of the $\alpha$-particles ($E_\alpha$). This can be expressed as a

Table 6.3: Wood-Saxon potentials used in the PLATYPUS calculations for $^7$Li + $^{93}$Nb reaction.

| Mass Partition | $V_0$ (MeV) | $r_0$ (fm) | $a_0$ |
|:---:|:---:|:---:|:---:|
| $^7$Li + 93Nb | -109.2 | 1.33 | 0.81 |
| $\alpha$ + 93Nb | -100.0 | 1.25 | 0.77 |
| $t$ + 93Nb | -110.0 | 1.20 | 0.72 |
| $t + \alpha$ | -18.2 | 1.28 | 0.63 |
| $t$ + $^{97}$Tc | -110.0 | 1.20 | 0.72 |
| $\alpha$ + $^{96}$Mo | -100.0 | 1.25 | 0.77 |

the inter nuclear distance. The amplitude and slope of the breakup-probability function $\beta = \ln(A) = 27.5$ and $\alpha = 3.0$ fm$^{-1}$, respectively, have been obtained by reproducing the integrated cross sections of breakup, complete fusion, and incomplete fusion (sum of $t$- and $\alpha$-capture) simultaneously. Location of the breakup of $^7$Li into $\alpha$ and $t$ was determined by Monte Carlo sampling of the breakup function up to R = 50 fm. The initial excitation energy ($E^* \leq 6$ MeV) and angular momentum (up to $4\hbar$) of the $^7$Li nuclei have also been generated using Monte Carlo method. The cumulative cross sections of $\alpha$- and $t$-capture have been calculated using a sharp cut-off in angular momenta. The convergence of the calculated cross section are ensured by including projectile-target partial waves up to $50\hbar$, for a sample of 1000 projectiles per partial wave. The comparison between the calculation and the measured values are shown in Table 6.4.

Table 6.4: The calculated CF, $t$-capture, $\alpha$-capture, and breakup cross sections from code PLATYPUS for $^7$Li + $^{93}$Nb reaction are given along with the measured values.

| $E_{\text{lab}}$ | $t$-ICF | | $\alpha$-ICF | | CF | | BU | |
|:---:|:---:|:---:|:---:|:---:|:---:|:---:|:---:|:---:|
| | $\sigma_{\text{exp}}$ | $\sigma_{\text{cal}}$ | $\sigma_{\text{exp}}$ | $\sigma_{\text{cal}}$ | $\sigma_{\text{exp}}$ | $\sigma_{\text{cal}}$ | $\sigma_{\text{exp}}$ | $\sigma_{\text{cal}}$ |
| (MeV) | (mb) | (mb) | (mb) | (mb) | (mb) | (mb) | (mb) | (mb) |
| 29.7 | 210 ± 35 | 177 | 88 ± 14 | 65 | 833 ± 73 | 742 | 46± 5 | 52 |
| 27.7 | 206 ± 33 | 171 | 71 ± 9 | 57 | 742 ± 65 | 616 | 45± 4 | 56 |
| 25.6 | 202 ± 37 | 156 | 53 ± 7 | 46 | 587 ± 49 | 497 | 41± 5 | 59 |
| 23.6 | 199 ± 34 | 126 | 41 ± 6 | 30 | 491 ± 40 | 391 | 40± 5 | 62 |

obtained after fitting $\sigma_{t-cap}$ is re-plotted in Fig. 6.11(b) as the solid line and is found to explain the general trend observed for $\sigma_\alpha^{incl} - \sigma_\alpha^{CN}$ as well. This observation also suggests that the main contribution to $\sigma_\alpha^{incl}$ is $\sigma_{t-cap}$. For the light mass targets $^{12}$C, $^{27}$Al, and $^{28}$Si [115, 116, 117], there is a substantial contribution from $\alpha$-particle evaporation from the compound nucleus. However, for the heavier targets the $t$-capture mechanism is the main source of $\alpha$-particle production. For $^6$Li $d$-capture is reported to be the dominant mechanism of $\alpha$ production [4, 24, 33, 37].

## 6.9 Classical dynamical trajectory model calculation for fragment-capture reactions

A three-body classical dynamical trajectory model calculations have been carried out to do a consistent analysis of breakup, incomplete fusion, and complete fusion processes. The calculations have been performed using the PLATYPUS code [31, 36]. A brief description of the code is given in Sec. 3.4. In the calculations $^7$Li was considered as $\alpha + t$ cluster, having a binding energy of 2.47 MeV. The pre- and post-breakup Coulomb and nuclear interactions between the participants ($^7$Li + $^{93}$Nb, $\alpha$ + $^{93}$Nb, $t$ + $^{93}$Nb, $t$ + $\alpha$, $t$ + $^{97}$Tc and $\alpha$ + $^{96}$Mo), have been taken as those between a point charge and a spherical distribution for the heaviest fragment (=$1.2A^{1/3}$). The nuclear interaction has been parametrized by a Woods-Saxon potential as given in Table 6.3.

The entrance channel interaction potentials used the global $^7$Li parameters of Ref. [88] which give a satisfactory description of the measured elastic scattering data. The $t + \alpha$ interaction potentials is taken from Ref. [30]. The breakup-probability is calculated using the function $P_{BU}(R)$=Aexp(-$\alpha R$), where $R$ denotes

are the beam energy in the center of mass frame, $^7$Li and target atomic numbers, $^7$Li and target mass numbers, respectively. The $\sigma_{t-\mathrm{cap}}$ are found to follow the Wong formula [113], slightly modified to obtain a better fit at energies above the Coulomb barrier:

$$\sigma_{t-\mathrm{cap}} = \frac{ac}{2x} \ln \left[ 1 + \exp \left\{ \frac{2\pi}{c}(d-b) \tanh \left( \frac{x-b}{d-b} \right) \right\} \right] \tag{6.2}$$

where $x = E_{\mathrm{R}}$, and $a$, $b$, $c$ and $d$ are adjustable parameters.
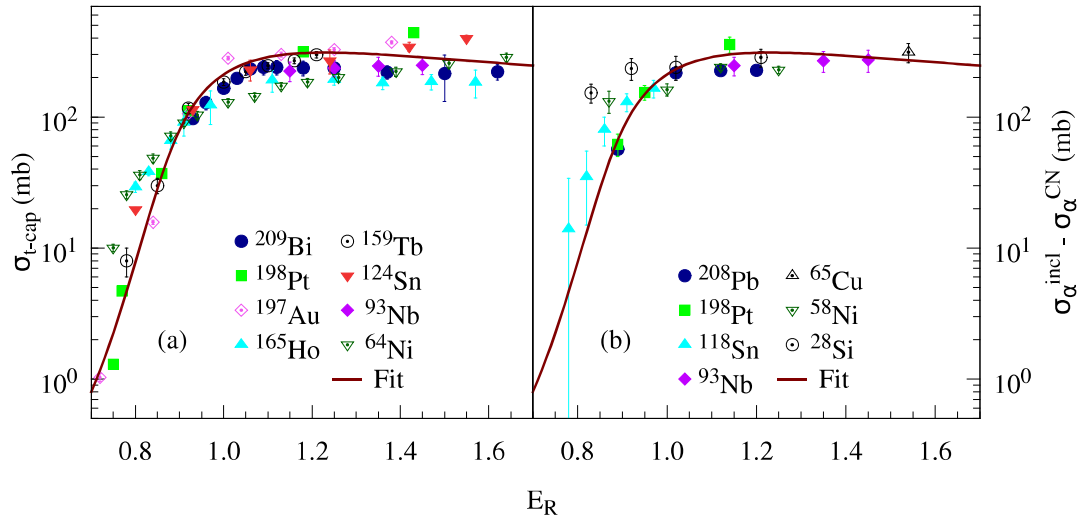


Figure 6.11:   (a) $t$-capture and (b) inclusive $\alpha$-production cross sections after the subtraction of the compound nuclear contribution, for $^7$Li projectiles incident on several targets including $^{93}$Nb (present data) as a function of $E_{\mathrm{R}} = E_{\mathrm{c.m.}}/[Z_{\mathrm{p}}Z_{\mathrm{t}}/(A_{\mathrm{p}}^{1/3} + A_{\mathrm{t}}^{1/3})]$. The solid lines represent the best fit to the $t$-capture data.

The inclusive $\alpha$ cross sections ($\sigma_\alpha^{\mathrm{incl}}$) after subtraction of the compound nuclear component ($\sigma_\alpha^{\mathrm{CN}}$) estimated using the statistical model code PACE for the $^7$Li+$^{208}$Pb [114], $^7$Li+$^{198}$Pt [51], $^7$Li+$^{118}$Sn [24], $^7$Li+$^{93}$Nb [50], $^7$Li+$^{65}$Cu [23], $^7$Li+$^{58}$Ni [24], and $^7$Li+$^{28}$Si [115] systems are presented in Fig. 6.11(b). The curve

Table 6.2: The cross sections of all possible reaction mechanisms contributing to the $\alpha$-particle yield. $t$-capture: $\sigma_{\text{t-cap}}$, $2n$ stripping $(^7\text{Li},^5\text{Li} \rightarrow \alpha + p)^{95}\text{Nb}$: $\sigma_\alpha^{\alpha-\text{p}}$, inelastic excitation $(^7\text{Li},^7\text{Li}^* \rightarrow \alpha + t)^{93}\text{Nb}$: $\sigma_\alpha^{\alpha-\text{t}}$, $1n$ stripping $(^7\text{Li},^6\text{Li}^* \rightarrow \alpha + d)^{94}\text{Nb}$: $\sigma_\alpha^{\alpha-\text{d}}$, $1p$ pickup $(^7\text{Li},^8\text{Be} \rightarrow \alpha+\alpha)^{92}\text{Zr}$: $\sigma_\alpha^{\alpha-\alpha}$, and $\alpha$-particle evaporation from the compound nucleus estimated using the code PACE: $\sigma_\alpha^{\text{CN}}$ are presented. The cumulative contribution $\sigma_\alpha^{\text{total}}$ along with the inclusive $\alpha$ yield $(\sigma_\alpha^{\text{incl}})$ are also given.

| $E_{\text{lab}}$ | 23.6 MeV | 25.6 MeV | 27.7 MeV | 29.7 MeV |
|---|---|---|---|---|
| reaction | $\sigma$ (mb) | $\sigma$ (mb) | $\sigma$ (mb) | $\sigma$ (mb) |
| $t$-capture | $199 \pm 34$ | $202 \pm 37$ | $206 \pm 33$ | $210 \pm 35$ |
| $2n$-stripping $(^7\text{Li},^5\text{Li} \rightarrow \alpha + p)$ | $17.3 \pm 3.0$ | $17.5 \pm 2.8$ | $20.1 \pm 2.5$ | $18.8 \pm 3.0$ |
| inelastic $(^7\text{Li},^7\text{Li}^* \rightarrow \alpha + t)$ | $15.1^a \pm 1.4$ | $15.9^b \pm 1.4$ | $16.8 \pm 1.2$ | $18.0^b \pm 1.2$ |
| $1n$ stripping $(^7\text{Li},^6\text{Li}^* \rightarrow \alpha + d)$ | $5.2 \pm 0.5$ | $5.5^b \pm 0.5$ | $5.8 \pm 0.4$ | $6.2 \pm 0.4$ |
| $1p$ pickup $(^7\text{Li},^8\text{Be} \rightarrow \alpha+\alpha)$ | $2.0 \pm 0.2$ | $2.2^a \pm 0.2$ | $2.6 \pm 0.2$ | $3.0 \pm 0.4$ |
| $\alpha$-particle evaporation | 27 | 39 | 53 | 69 |
| measured total $\sigma_\alpha^{\text{total}}$ | $266 \pm 39$ | $282 \pm 42$ | $304 \pm 38$ | $325 \pm 41$ |
| measured inclusive $\sigma_\alpha^{\text{incl}}$ | $273 \pm 40$ | $296^a \pm 50$ | $321 \pm 48$ | $340 \pm 52$ |
| $\sigma_\alpha^{\text{total}}/\sigma_\alpha^{\text{incl}}$ (%) | 97 | 95 | 95 | 96 |

[a]Extrapolated

[b]Interpolated

measured reaction processes and estimated CN contribution are also tabulated in Table 6.2, which explain $\sim$95% of the measured $\sigma_\alpha^{incl}$.

## 6.8 Systematic study on $t$-capture and inclusive-$\alpha$

A systematic study of the $t$-capture and inclusive $\alpha$ cross sections have been carried out for reactions involving $^7\text{Li}$ over a range of lighter to heavier targets including the present system. The measured $\sigma_{t-\text{cap}}$ for the $^7\text{Li}+^{93}\text{Nb}$ (present work), $^7\text{Li}+^{209}\text{Bi}$ [106], $^7\text{Li}+^{197}\text{Au}$ [108], $^7\text{Li}+^{198}\text{Pt}$ [30], $^7\text{Li}+^{165}\text{Ho}$ [109], $^7\text{Li}+^{159}\text{Tb}$ [110], $^7\text{Li}+^{124}\text{Sn}$ [111], and $^7\text{Li}+^{64}\text{Ni}$ [112] systems are presented in Fig. 6.11(a). The $x$-axis in Fig. 6.11 is defined as $E_{\text{R}} = E_{\text{c.m.}}/[Z_{\text{p}}Z_{\text{t}}/(A_{\text{p}}^{1/3} + A_{\text{t}}^{1/3})]$, where $E_{\text{c.m.}}$, $Z_{\text{p}}$, $Z_{\text{t}}$, $A_{\text{p}}$, $A_{\text{t}}$

results reported in earlier studies with $^7$Li projectiles [30, 106, 107]. The estimated $\alpha$-particle evaporation cross sections are also plotted in Fig. 6.10 as well as the calculated reaction cross sections from coupled channels calculations.
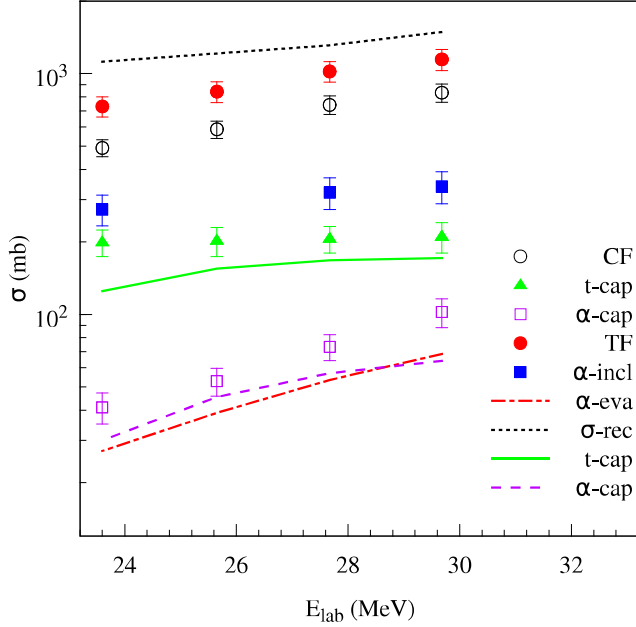


Figure 6.10: The measured CF, $t$-capture, $\alpha$-capture, TF, and $\alpha$-inclusive are presented by open circles, filled triangles, open boxes, filled circles and filled squares, respectively. The dot-dashed, dotted, solid, and dashed lines are corresponding to the estimated $\alpha$-evaporation, total reaction, $t$-capture, and $\alpha$-capture cross sections, respectively.

## 6.7 Sources of large inclusive-$\alpha$ yield

The cross sections of all important reaction mechanisms contributing to the $\alpha$-particle yield (as seen in Fig. 6.3(a)) from the present thesis work are listed in Table 6.2 for comparison. The statistical model predictions for $\alpha$-particle evaporation ($\sigma_\alpha^{CN}$) from the compound nucleus are also given. The $t$-capture process is found to be the dominant reaction mechanism, which accounts for ~62-73% of $\sigma_\alpha^{incl}$, whereas the combined contribution of the breakup and nucleon transfer followed by breakup channels is ~15%. The cumulative contributions from all these

## 6.5  Correction of CN contribution to the residues of fragment-capture reactions

The compound nuclear contribution to the cross sections of $^{93-95}$Mo and $^{95,96}$Tc residues have been estimated. The same statistical model parameters, which explain the evaporation residues discussed in the Sec. 6.4, are used. The calculated cross sections for $^{94,95}$Mo are found to be smaller by an order of magnitude relative to the measured cross sections at all energies, as shown in Fig. 6.6. The cross sections of $^{94-95}$Mo and $^{95,96}$Tc residues after the subtraction of CN contribution are shown in Fig. 6.12. This observation suggests that the dominant reaction mechanism responsible for production of $^{93-95}$Mo nuclei is not compound nuclear fusion but $t$-capture. Similarly, the predicted cross sections for $^{96}$Tc are also found to be far smaller than the measured values as shown in Fig. 6.8, implying that $^{95,96}$Tc nuclei are produced mainly due to the $\alpha$-capture mechanism.

## 6.6  Total cross sections of $t$-capture, $\alpha$-capture and complete fusion

The cross sections of individual residues from $\alpha$ and $t$-capture are corrected for the contribution from the compound nucleus. The $t$-capture, $\alpha$-capture and complete fusion cross sections have been obtained by taking the sum of individual residue cross sections and are presented in Fig. 6.10. The cross sections of $t$-capture and $\alpha$-capture reactions are tabulated in Table 6.4. The cross sections for $t$-capture are found to be larger than those for $\alpha$-capture at all energies, in agreement with the
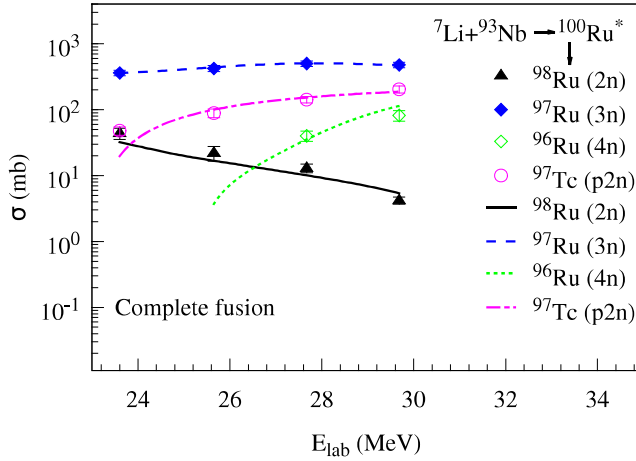
Figure 6.9: ER cross sections of $2n$, $3n$, $4n$, and $p2n$ evaporation channels following CF reaction are shown by filled triangles, open boxes, open diamonds, and open circles, respectively. The filled diamonds correspond to the measured cross sections of $^{97}$Ru from off-beam $\gamma$-ray counting method. The lines are the statistical model (PACE) estimations of corresponding residues.

## 6.4 Statistical model calculations for compound nuclear decay

Statistical model calculations have been carried out using the code PACE [78] to estimate the contribution from complete fusion to the residues resulting from $\alpha$ and $t$-capture. The angular momentum distribution obtained from the coupled-channel code CCFULL [105] is used as input at each energy to obtain the cross sections of the decay channels. The level density parameter $a = A/9$ was used in the calculations. The estimated ER cross sections explain the measured values as shown in Fig. 6.9.

Table 6.1: List of identified residues in the offline gamma ray measurement for the $^7$Li+$^{93}$Nb reaction along with their radioactive decay half-lives (T$_{1/2}$), $\gamma$-ray energies and intensities following their decays.

| Reaction | Residues | T$_{1/2}$ | E$_\gamma$ (keV) | I$_\gamma$ (%) |
|---|---|---|---|---|
| CF-3$n$ | $^{97}$Ru | 2.83 d | 215.7 | 85.6 |
| | | | 324.5 | 10.8 |
| CF-$\alpha$3$n$/ $t$-ICF-3$n$ | $^{93m}$Mo | 6.85 h | 263.1 | 57.4 |
| | | | 684.7 | 99.9 |
| CF-$p$3$n$/ $\alpha$-ICF-$n$ | $^{96g}$Tc | 4.28 d | 778.2 | 99.8 |
| | | | 812.5 | 82.0 |
| | | | 1126.9 | 15.2 |
| | $^{96m}$Tc | 51.5 min | 1200.1 | 1.1 |
| CF-$p$4$n$/ $\alpha$-ICF-2$n$ | $^{95g}$Tc | 20 h | 765.8 | 93.8 |
| | | | 947.7 | 1.95 |
| | | | 1073.7 | 3.74 |
| | $^{95m}$Tc | 61 d | 204.1 | 63.2 |
| | | | 835.2 | 26.6 |
| 2$n$-stripping | $^{95g}$Nb | 34.99 d | 765.8 | 99.8 |
| | $^{95m}$Nb | 3.61 d | 235.7 | 24.8 |

## 6.3.4 Complete fusion

The complete fusion of $^7$Li with $^{93}$Nb forms the compound nucleus (CN) $^{100}$Ru, which decays predominantly by neutron and proton emission. The characteristic prompt $\gamma$-ray transitions of the evaporation residues (ERs) $^{96-98}$Ru and $^{97}$Tc are labeled in Fig. 6.1. The cross sections of $^{96-98}$Ru and $^{97}$Tc are obtained using the in-beam method taking the level schemes from Refs. [102, 103]. The cross sections for $^{97}$Ru are also extracted using the off-beam $\gamma$-ray counting method and found to be consistent with the in-beam measurements and with the values reported in Ref. [104]. The weighted average values of the cross sections obtained from the in-beam and off-beam methods are shown in Fig. 6.9. The cross sections for $^{96,98}$Ru and $^{97}$Tc are plotted in the same figure.

by filled circles and stars respectively. The decay transitions from the ground state of $^{95}$Tc are represented by open circles. The cross sections are extracted following the same method as discussed for $^{93}$Mo and are shown in Fig.6.8. The cross sections of $^{95,96}$Tc are obtained by adding the corresponding cross sections of ground state and meta-stable state.
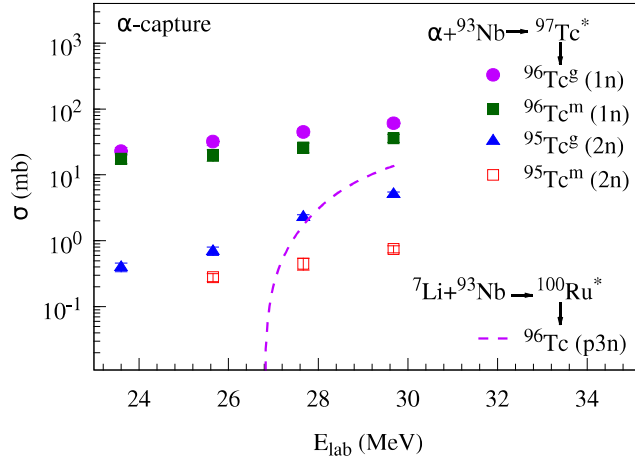


Figure 6.8: The measured residue cross sections of ground state and isomeric state of $^{95,96}$Tc residues for the $^7$Li+$^{93}$Nb reaction are shown by filled triangles, open boxes, filled circles, and filled boxes, respectively. The lines are the statistical model (PACE) estimations of corresponding residues.

### 6.3.3  2$n$-stripping

The 2$n$-stripping mechanism leads to $^{95}$Nb, which is radioactive with reasonable half-lives for decay from the ground states (T$_{1/2}$ = 34.99 d) and from the meta-stable states (T$_{1/2}$ = 3.61 d). The $\gamma$-ray transitions corresponding to the decay of $^{95}$Nb are labeled in Fig. 6.7. The cross sections are extracted following the half-lives and intensities of each transitions. The 2$n$-stripping cross sections have been obtained by taking the sum of the ground state and meta-stable state cross sections.

and intensity of $\gamma$-transitions, which were used to extract the cross sections are tabulated in Table 6.1. The extracted cross sections for $^{93m}$Mo are $0.06 \pm 0.01$ mb and $0.6 \pm 0.08$ mb at $E_{lab} = 27.7$ and 29.7 MeV, respectively. This is much smaller than the cross sections for $^{94-95}$Mo nuclei.
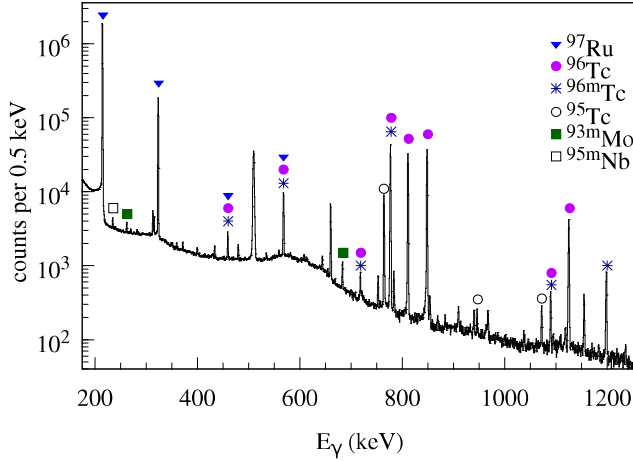


Figure 6.7: The off-beam $\gamma$-ray spectrum for the $^7$Li$+^{93}$Nb reaction at $E_{lab} = 27.7$ MeV. The $\gamma$ transitions from residues following CF ($^{97}$Ru), $\alpha$-capture ($^{95,96}$Tc), $t$-capture ($^{93m}$Mo) and $2n$-transfer ($^{95m}$Nb) are labeled.

The formation cross sections of $^{94}$Mo is found to be largest relative to the other isotopes. The radioactive half-life of ground state of $^{93}$Mo nuclei is $T_{1/2} = 4000$ years, and the formation cross section is also expected to be small ($\sim$1 mb), the present setup is not sensitive to measure $^{93g}$Mo residue.

## 6.3.2  $\alpha$-capture

The $\alpha$-capture reaction followed by $1n$ and $2n$ evaporation leads to $^{95,96}$Tc. Both $^{95,96}$Tc can be populated either in the ground state or the meta-stable state. These nuclei are radioactive with reasonable half-lives for decay from their ground states as well as from the meta-stable states. The half lives are $T_{1/2}(^{95g}$Tc$) = 20.0$ h, $T_{1/2}(^{96g}$Tc$) = 4.28$ d ($T_{1/2}(^{95m}$Tc$) = 61$ d, and $T_{1/2}(^{96m}$Tc$) = 51.5$ m. The $\gamma$-ray transitions from the ground state and meta-stable state of $^{96}$Tc are shown in Fig. 6.7

The parameters $a$, $J_0$, and $b$ were varied so as to minimize the $\chi^2$ fit to the data at each bombarding energy. The same value of $b = 1.697$ was used for different beam energies. The filled curves are plotted in Fig. 6.5. The cross sections of $^{94}$Mo are presented in Fig.6.6 by filled circles.
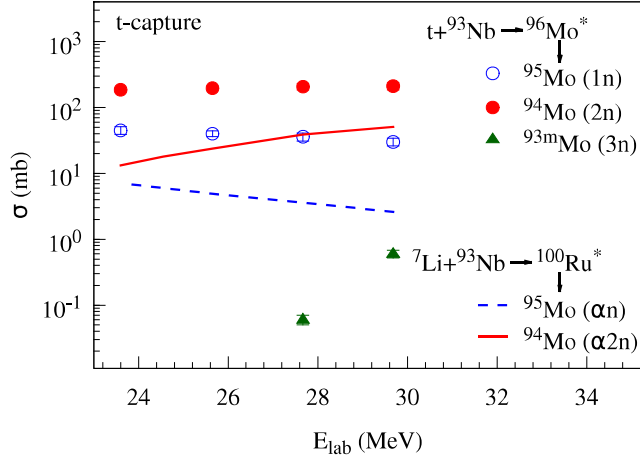


Figure 6.6: The cross sections of $^{93-95}$Mo nuclei populated in $^7$Li+$^{93}$Nb reaction are shown. The solid and dashed lines are estimated CN contribution from statistical model code (PACE for $\alpha n$ and $\alpha 2n$ channels.

For the odd-even $^{95}$Mo nuclei, due to fragmented transitions, the decay scheme is complicated [101]. In this case the cross sections are obtained by adding the $\gamma$-ray transitions, feeding directly to the ground state. The cross sections of $^{95}$Mo are presented in Fig. 6.6 by open circles.

The $^{93}$Mo nucleus has a $21/2^+$ isomeric state at $E_{ex} = 2.425$ MeV with half-life $T_{1/2} = 6.85$ h. The cross section for $^{93m}$Mo has been obtained by following the radioactive decay of the isomeric state. The details of the off-beam $\gamma$-counting method are discussed in Chapter 2. A typical $\gamma$-ray spectrum obtained after the end of the irradiation at $E_{lab} = 27.7$ MeV for a counting of $\sim$5 h has been shown in Fig. 6.7. The characteristic $\gamma$-rays are identified and labeled. The $\gamma$-ray transitions from the decay of $^{93m}$Mo are also labeled in the same figure. The details of the method for extraction of cross section is given in Sec. 2.9.3. The energy

### 6.3.1  *t*-capture

Though we have stated that Mo-isotopes can be populated from both the *t*-capture and complete fusion reaction, later in this chapter we have shown that the contribution of compound nuclear evaporation is comparably smaller than the *t*-capture reaction. We now discuss the measured cross sections of Mo-residues.
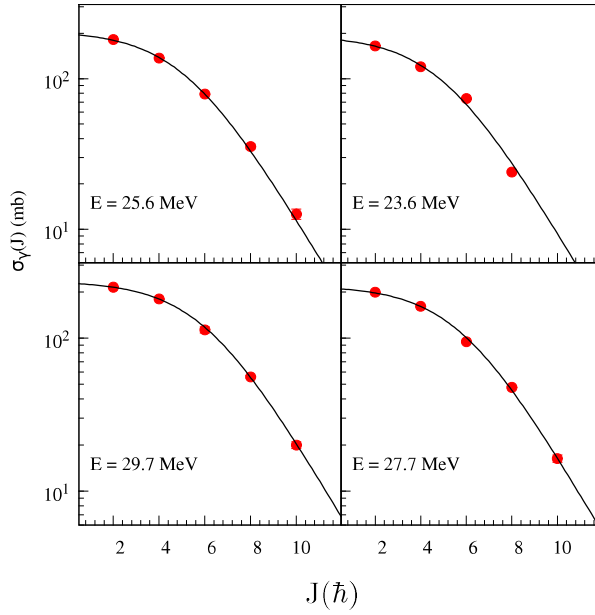


Figure 6.5: Transition cross sections for the ground state rotational band transition $J \to J\text{-}2$ of $^{94}$Mo populated in $^{7}$Li+$^{93}$Nb reaction at beam energies 23.6, 25.6, 27.7 and 29.7 MeV respectively. The solid curves are the fits to the data by using a Fermi function $\sigma_\gamma(J) = a/[1 + \exp[-(J - J_0 )/b]$ as described in the text.

In Fig. 6.5, the cross sections upto $10^+$ excited state of $^{94}$Mo from the yrast band [100] are shown. As discussed in Chapter 2, to extract the cross sections, the $\sigma_\gamma(\text{J})$ values were extrapolated up to the value corresponding to $J = 0$. The $\sigma_\gamma(\text{J})$ values were fitted using Fermi function,

$$\sigma_\gamma(J) = \frac{a}{1 + exp[(J - J_0)/b]}, \tag{6.1}$$

Where, $a$, $b$, and $J_0$ correspond to the normalization constant, the diffuseness of the $J$ distribution, and the value of $J$ at which $\sigma_\gamma(J)$ becomes $a/2$, respectively.

120
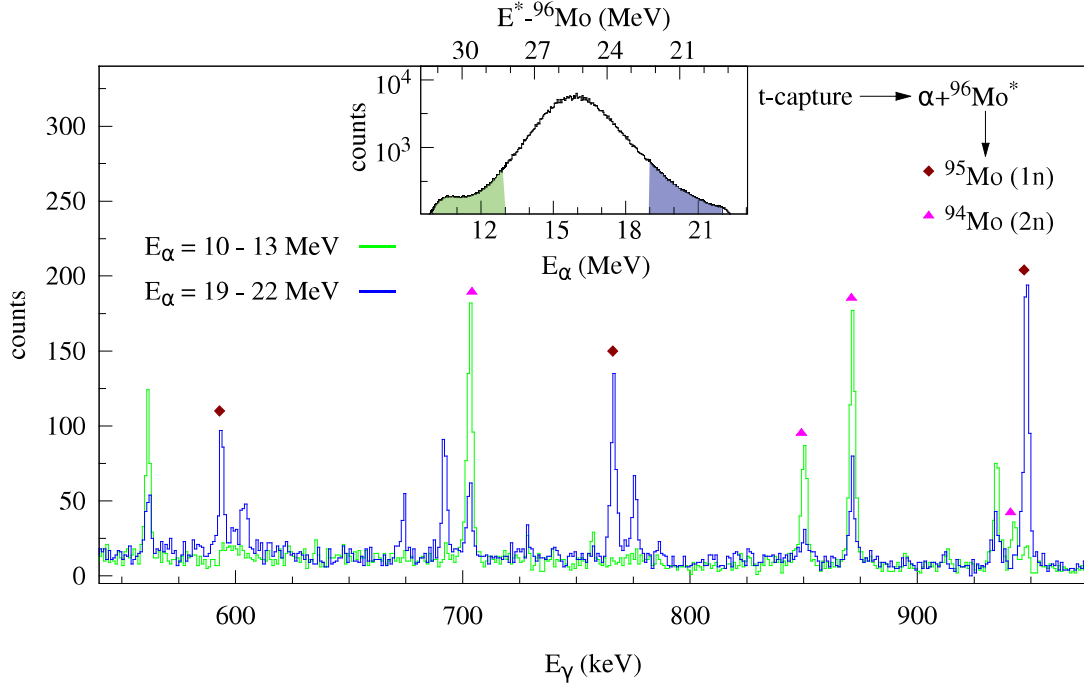
Figure 6.4: Prompt $\gamma$-ray spectrum in coincidence with $\alpha$-particle with different energy range for $^7$Li+$^{93}$Nb reaction at $E_{lab} = 27.7$ MeV. The energy spectra of the $\alpha$-particle measured in coincidence is shown in the inset. The $\gamma$-transitions from $^{94,95}$Mo nuclei due to $t$-capture followed by $1n$ and $2n$ evaporation are labeled. Unlabeled $\gamma$-lines are from residues populated in those reaction processes, which have $\alpha$-particles in the outgoing channels.

## 6.3 Cross sections of residues populated in the $^7$Li+$^{93}$Nb reaction

In the following sections the extracted cross sections of different residues populated in the present reactions have been discussed. The compound nuclear contribution to the residue populated due to different fragment-capture reactions are also estimated to extract the cross sections of $\alpha$-capture and $t$-capture mechanisms.

of $^{97}$Tc (CF followed by $p2n$ evaporation) is maximum. Similar to Mo isotopes, the observed $^{95,96}$Tc nuclei could also be populated due to $pxn$-evaporation from CN and $\alpha$-capture followed by $xn$-evaporation.

## 6.2.1 Prompt $\gamma$-ray in coincidence with $\alpha$-particle of different energy range

The two mechanisms breakup-fusion and direct stripping can not be easily differentiated from particle-$\gamma$ coincidence data, which is presented in Fig. 6.3(a). Thus a further attempt has been made to do so, which is as follows. Here, the $t$-capture reaction that leads to the $^{96}$Mo of different excitation energy has been studied by measuring the prompt $\gamma$-ray transitions in coincidence with $\alpha$-particle of different energy range. The projected energy spectra of the $\alpha$-particle of Fig. 6.2 is shown in the inset of Fig. 6.4. Two energy range $E_\alpha$ = 9-12 MeV and 19-22 MeV are shown by green and blue colored shaded area, respectively. The excitation energy of the $^{96}$Mo$^*$ is estimated from the kinematics, using the measured energy of the $\alpha$-particle, as labeled on the top axis of the inset of the Fig. 6.4. The variation in population of the residues for the selected energy bin of the $\alpha$-particle are plotted in Fig. 6.4. The outgoing $\alpha$-particle with higher (lower) kinetic energy corresponds to the lower (higher) excitation energy in $^{96}$Mo. As can be seen from the figure the $\gamma$-peaks of the residues, which is correspond to the one neutron evaporation channel ($^{95}$Mo), are dominant with the higher $\alpha$-energy bin while those from two neutron evaporation channel ($^{94}$Mo) are dominant with the lower energy bin. Excitation energy dependence of residue cross section for different kinetic energy of captured triton supports the process of breakup-fusion.

mechanisms. The reaction mechanisms contributing to $\alpha$-particle yield, e.g. $1p$ pickup $(^7\text{Li},^8\text{Be}^* \rightarrow \alpha+\alpha)^{92}\text{Zr}$, inelastic excitation $(^7\text{Li},^7\text{Li}^* \rightarrow \alpha + t)^{93}\text{Nb}$, $1n$ stripping $(^7\text{Li},^6\text{Li}^* \rightarrow \alpha+d)^{94}\text{Nb}$, and $2n$ stripping $(^7\text{Li},^5\text{Li}^* \rightarrow \alpha+p)^{95}\text{Nb}$ are also marked in Fig. 6.3(a).
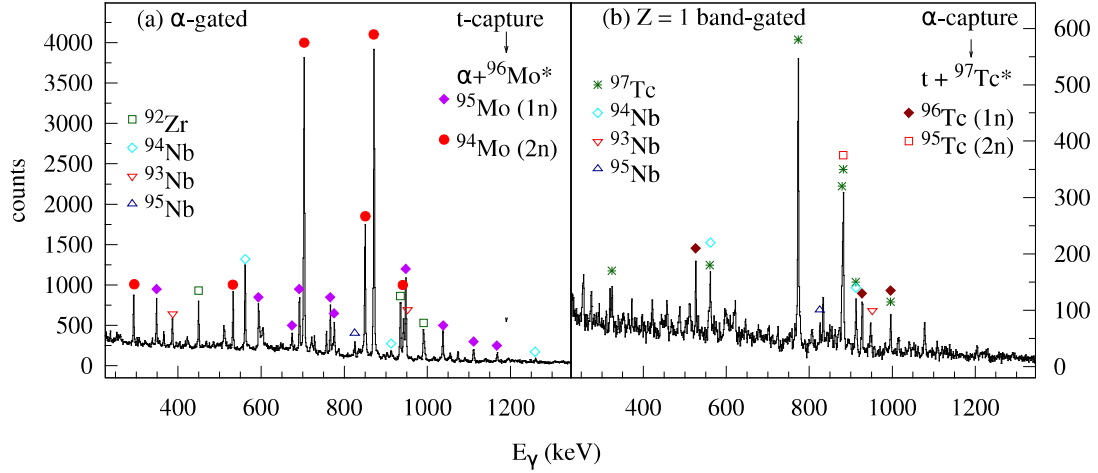


Figure 6.3: Charge particle gated prompt $\gamma$-ray spectra for $^7\text{Li}+^{93}\text{Nb}$ reaction at $E_{\text{lab}} = 27.7$ MeV. (a) Prompt $\gamma$-ray spectrum in coincidence with $\alpha$-particle in the outgoing channel. The $\gamma$-transitions from $^{94,95}\text{Mo}$ nuclei due to $t$-capture followed by $1n$ and $2n$ evaporation are labeled. The $\gamma$-transitions from target like nuclei $^{92}\text{Zr}$, $^{93,94,95}\text{Nb}$ formed due to $1p$ pickup followed by breakup $(^8\text{Be}^* \rightarrow \alpha+\alpha)$, inelastic excitation followed by breakup $(^7\text{Li}^* \rightarrow \alpha + t)$, $1n$ stripping followed by breakup $(^6\text{Li}^* \rightarrow \alpha + d)$, and $2n$ stripping followed by breakup $(^5\text{Li}^* \rightarrow \alpha + p)$ reaction mechanisms having $\alpha$-particle in the outgoing channels are also labeled. (b) Particle having Z=1 gated $\gamma$-ray spectrum. The $\gamma$-transitions from $^{95,96}\text{Tc}$ nuclei due to $\alpha$-capture followed by $1n$ and $2n$ evaporation are labeled. The photo peaks of the $\gamma$-transitions from the nuclei populated in the other reaction processes producing $p/d/t$ in the out going channels are also shown.

Gamma-ray spectrum gated with Z=1 band from the two-dimensional telescope spectrum is shown in Fig. 6.3(b). The photo peaks of the $\gamma$-ray transition from the residues populated due to complete fusion followed by $p2n$ evaporation $(^{97}\text{Tc})$, $\alpha$-capture followed by $xn$-evaporation, and other breakup processes that lead to $t, d$ and $p$ in the outgoing channels (discussed above) are labeled. It is found that yield

2*n*-stripping reactions, respectively, are also labeled.

A typical gain matched $\Delta E$ vs $E_{\text{tot}}$ spectrum of charged particles, detected in Si-surface barrier telescope, for $^7$Li+$^{93}$Nb system at energy $E_{\text{lab}}$ = 27.7 MeV and $\theta_{\text{lab}}$ = 35° is shown in Fig.6.2. This spectrum is generated using the digitized output of the preamplifier signals corresponding to Si-$\Delta E$ and $E$-detectors. The different Z-bands are well resolved and identified. But isotopic separation of Z=1 band is not achieved here, which is the limitation of the digital data acquisition system having 12-bit 100 MHz Flash Analog to Digital Converter (FADC).
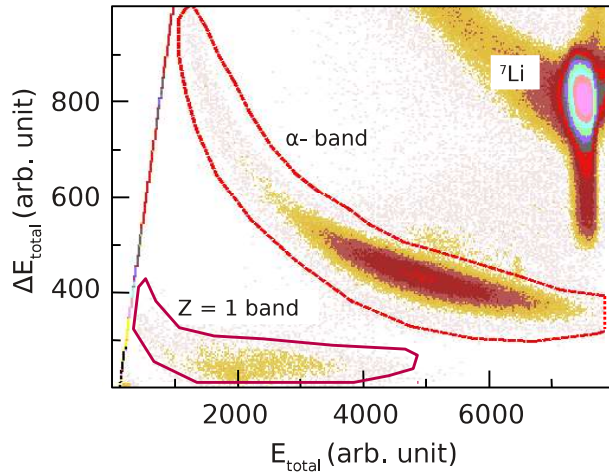


Figure 6.2: A typical two dimensional spectrum of $\Delta E$ vs $E_{\text{tot}}$ for $^7$Li on $^{93}$Nb at energy $E_{\text{lab}}$ = 27.7 MeV and $\theta_{\text{lab}}$ = 35°.

## 6.2  Particle-$\gamma$ coincidence

The $\alpha$-particle gated in-beam $\gamma$-ray spectra shown in Fig. 6.3(a), gives a snapshot of the major reaction processes contributing to $\alpha$-particle yields. It can be seen clearly, that the relative yields of $\gamma$-rays from $^{94,95}$Mo residues are more than the others. As already mentioned $^{94,95}$Mo residues could be populated due to complete fusion as well as *t*-capture. This coincidence data inferred that, main sources of $\alpha$-production are evaporated $\alpha$-particles from compound nucleus and *t*-capture

# 6.1 Inclusive $\gamma$-ray and charged particle spectra

The addback in-beam inclusive $\gamma$-ray spectrum measured by INGA-setup is shown in Fig.6.1. The complete fusion of $^7$Li with $^{93}$Nb forms the compound nucleus $^{100}$Ru, which decays predominantly by neutron and proton emission. The characteristic prompt $\gamma$-rays from CN residues $^{96,97,98}$Ru and $^{97}$Tc are observed and labeled in Fig.6.1.
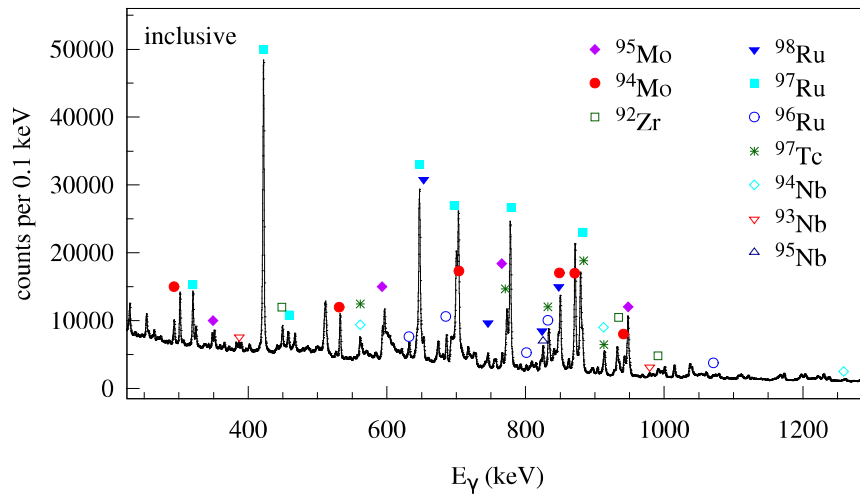


Figure 6.1: Addback in-beam $\gamma$-ray spectrum for $^7$Li+$^{93}$Nb reaction at $E_{\text{lab}} = 27.7$ MeV. The $\gamma$-transitions from $^{94,95}$Mo nuclei due to $t$-capture followed by $1n$ and $2n$ evaporation along with evaporation residues $^{96-98}$Ru and $^{97}$Tc are labeled. The characteristic prompt $\gamma$-rays from target like nuclei $^{92}$Zr, $^{93-95}$Nb formed due to $1p$ pickup followed by breakup ($^8$Be$^* \rightarrow \alpha+\alpha$), inelastic excitation followed by breakup ($^7$Li$^* \rightarrow \alpha + t$), $1n$ stripping followed by breakup ($^6$Li$^* \rightarrow \alpha + d$), and $2n$ stripping followed by breakup ($^5$Li$^* \rightarrow \alpha + p$) reaction mechanisms having $\alpha$-particle in the outgoing channels are also labeled.

The $\gamma$-transitions from $^{94,95}$Mo nuclei are also observed. The residue $^{94,95}$Mo could be formed either due to complete fusion followed by $\alpha xn$ evaporation or $t$-capture followed by $xn$ evaporation. The observed photo-peaks of $\gamma$ rays from $^{92}$Zr, $^{93,94}$Nb and $^{95}$Nb nuclei formed by $1p$-pickup, inelastic excitation, $1n$-stripping, and

duction cross sections in the reactions involving weakly bound projectiles with $\alpha + x$ cluster structure, e.g. $^{6,8}$He, $^{6,7}$Li, and $^{7,9}$Be. The observation of large $\alpha$-particle yield is interesting because it is large compared to that of the complementary fragments. If we presume that breakup process is the only responsible reaction mechanism for $\alpha$-particle yield, then the yield of complementary fragment is expected to be of the same order. We have measured the $\alpha$-production cross sections for $^{7}$Li + $^{89}$Y, $^{93}$Nb systems arising from various breakup reaction processes, namely, the breakup of $^{7}$Li ($^{7}$Li$^{*} \to \alpha + t$) together with $1p$-pickup followed by breakup ($^{8}$Be $\to \alpha + \alpha$) and $1n$-stripping followed by breakup ($^{6}$Li $\to \alpha + d$). As reported in the previous chapter, the cumulative contribution of all the measured reaction channels from exclusive measurements could explain only $\sim 8\%$ of the inclusive $\alpha$-yield for both the systems. For this reason it is interesting to measure the $t$-capture reaction, which also contributes to the $\alpha$-yield. The $t$-capture and $\alpha$-capture mechanisms have been investigated along with the complete fusion.

The Particle-$\gamma$ coincidence measurements were performed to identify the different fragment-capture reactions uniquely. The measurements were carried out for $^{7}$Li+$^{93}$Nb system at energies $E_{\text{lab}}$ = 23.6, 25.6, 27.7, and 29.7 MeV. The details of the measurements are given in Chapter 2. Due to the predominant $\alpha$-$t$ cluster structure, the $\alpha$-capture and $t$-capture are the dominant processes. The absolute cross sections of $\alpha$-capture, $t$-capture, and $2n$-stripping reactions along with complete fusion have been extracted by employing in-beam and off-beam $\gamma$-transitions counting method.

# 6

# Fragment-capture reaction

In the previous chapter, we discussed part of the investigation on reaction mechanisms populating the continuum states using the weakly bound nucleus $^7$Li. The study was limited specifically to the reaction channels, where none of the breakup fragments are captured by the target and could be detected in coincidence. The breakup of the weakly bound nuclei leads to another dominant reaction mode, where any one of the breakup-fragments can fuse with the target nuclei. This process can be looked upon as a two-step process, breakup followed by fusion (breakup-fusion) or incomplete fusion (ICF). As mentioned in Sec. 1.3.3, direct stripping of a cluster-fragment from the bound states of the projectile is indistinguishable from the breakup-fusion. In this thesis, the admixture of these two processes is referred to as fragment-capture mechanism. An extensive effort has been made to understand the relative importance of the two mechanisms. The breakup followed by fusion of all the fragments is also a possible reaction process, which is inseparable from complete fusion of the projectile (without breakup).

Another interesting phenomena is the observed large inclusive $\alpha$-particle pro-

[114] C. Signorini, M. Mazzocco, G. Prete, F. Soramel, L. Stroe, A. Andrighetto, I. Thompson, A. Vitturi, A. Brondi, M. Cinausero, et al., Eur. Phys. J. A **10**, 249 (2001).

[115] A. Pakou, N. G. Nicolis, K. Rusek, N. Alamanos, G. Doukelis, A. Gillibert, G. Kalyva, M. Kokkoris, A. Lagoyannis, A. Musumarra, et al., Phys. Rev. C **71**, 064602 (2005).

[116] V. V. Parkar, K. Mahata, S. Santra, S. Kailas, A. Shrivastava, K. Ramachandran, A. Chatterjee, V. Jha, and P. Singh, Nucl. Phys. A **792**, 187 (2007).

[117] K. Kalita, S. Verma, R. Singh, J. J. Das, A. Jhingan, N. Madhavan, S. Nath, T. Varughese, P. Sugathan, V. V. Parkar, et al., Phys. Rev. C **73**, 024609 (2006).

[103] D. Hippe, H. W. Schuh, U. Kaup, K. O. Zell, P. von Brentano, and D. B. Fossan, Z. Phys., A **311**, 329 (1983).

[104] D. Kumar, M. Maiti, and S. Lahiri, Phys. Rev. C **94**, 044603 (2016).

[105] K. Hagino, N. Rowley, and A. Kruppa, Comput. Phys. Commun. **123**, 143 (1999).

[106] M. Dasgupta, P. R. S. Gomes, D. J. Hinde, S. B. Moraes, R. M. Anjos, A. C. Berriman, R. D. Butt, N. Carlin, J. Lubian, C. R. Morton, et al., Phys. Rev. C **70**, 024606 (2004).

[107] V. V. Parkar, V. Jha, and S. Kailas, Phys. Rev. C **94**, 024609 (2016).

[108] C. S. Palshetkar, S. Thakur, V. Nanal, A. Shrivastava, N. Dokania, V. Singh, V. V. Parkar, P. C. Rout, R. Palit, R. G. Pillay, et al., Phys. Rev. C **89**, 024607 (2014).

[109] V. Tripathi, A. Navin, K. Mahata, K. Ramachandran, A. Chatterjee, and S. Kailas, Phys. Rev. Lett. **88**, 172701 (2002).

[110] A. Mukherjee, S. Roy, M. Pradhan, M. S. Sarkar, P. Basu, B. Dasmahapatra, T. Bhattacharya, S. Bhattacharya, S. Basu, A. Chatterjee, et al., Phys. Lett. B **636**, 91 (2006).

[111] V. V. Parkar *et al.*

[112] M. M. Shaikh, S. Roy, S. Rajbanshi, A. Mukherjee, M. K. Pradhan, P. Basu, V. Nanal, S. Pal, A. Shrivastava, S. Saha, et al., Phys. Rev. C **93**, 044616 (2016).

[113] C. Y. Wong, Phys. Rev. Lett. **31**, 766 (1973).

[92] S. P. V. Verst, D. P. Sanderson, K. W. Kemper, D. Shapira, R. L. Varner, and B. Shivakumar, Phys. Rev. C **36**, 1865 (1987).

[93] S. Cohen and D. Kurath, Nucl. Phys. A **101**, 1 (1967).

[94] R. E. Goans and C. R. Bingham, Phys. Rev. C **5**, 914 (1972).

[95] J. B. Moorhead and R. A. Moyer, Phys. Rev. **184**, 1205 (1969).

[96] R. Wadsworth, M. D. Cohler, M. J. Smithson, D. L. Watson, F. Jundt, L. Kraus, I. Linck, and J. C. Sens, Journal of Physics G: Nuclear Physics **9**, 1237 (1983).

[97] R. P. Chestnut, F. E. Cecil, and R. L. McGrath, Phys. Rev. C **10**, 2434 (1974).

[98] Y. Kucuk, I. Boztosun, and N. Keeley, Phys. Rev. C **79**, 067601 (2009).

[99] M. R. Cates *et al.*, Phys. Rev. **187**, 1682 (1969).

[100] B. Kharraja, S. S. Ghugre, U. Garg, R. V. F. Janssens, M. P. Carpenter, B. Crowell, T. L. Khoo, T. Lauritsen, D. Nisius, W. Reviol, et al., Phys. Rev. C **57**, 2903 (1998).

[101] J. M. Chatterjee, M. Saha-Sarkar, S. Bhattacharya, S. Sarkar, R. P. Singh, S. Murulithar, and R. K. Bhowmik, Phys. Rev. C **69**, 044303 (2004).

[102] B. Kharraja, S. S. Ghugre, U. Garg, R. V. F. Janssens, M. P. Carpenter, B. Crowell, T. L. Khoo, T. Lauritsen, D. Nisius, W. Reviol, et al., Phys. Rev. C **57**, 83 (1998).

[79] H. Fuchs, Nucl. Instr. and Meth. **200**, 361 (1982).

[80] Y. Tokimoto and H. Utsunomiya, Nuclear Instruments and Methods in Physics Research Section A: Accelerators, Spectrometers, Detectors and Associated Equipment **434**, 449 (1999).

[81] J. E. Mason, S. B. Gazes, R. B. Roberts, and S. G. Teichmann, Phys. Rev. C **45**, 2870 (1992).

[82] D. Tilley, J. Kelley, J. Godwin, D. Millener, J. Purcell, C. Sheu, and H. Weller, Nuclear Physics A **745**, 155 (2004).

[83] D. Brink, Phys. Lett. B **40**, 37 (1972).

[84] J. L. C. Ford, K. S. Toth, G. R. Satchler, D. C. Hensley, L. W. Owen, R. M. DeVries, R. M. Gaedke, P. J. Riley, and S. T. Thornton, Phys. Rev. C **10**, 1429 (1974).

[85] C. Beck, N. Keeley, and A. Diaz-Torres, Phys. Rev. C **75**, 054605 (2007).

[86] V. Avrigeanu, P. E. Hodgson, and M. Avrigeanu, Phys. Rev. C **49**, 2136 (1994).

[87] J. F. D. Becchetti and G. W. Greenlees, Polarization Phenomena in Nuclear Reactions (The University of Wisconsin Press, Madison, 1971) p. 682 (1971).

[88] J. Cook, Nucl. Phys. A **388**, 153 (1982).

[89] A. Weller *et al.*, Phys. Rev. Lett. **55**, 480 (1985).

[90] R. J. Puigh and K. W. Kemper, Nucl. Phys. A **313**, 363 (1979).

[91] F. Ajzenberg-Selove, Nucl. Phys. A **490**, 1 (1988).

[64] A. Bohr and B. R. Mottelson, vol. 2 (Benjamin, Reading, MA, 1975).

[65] G. R. Satchler (Macmillan Press, London, 1980).

[66] G. R. Satchler (Clarendon, Oxford, 1983).

[67] N. K. Glendenning (World Scientific, Singapore, 1983).

[68] N. Austern, R. M. Drisko, E. C. Halbert, and G. R. Satchler, Phys. Rev. **133**, B3 (1964).

[69] N. Austern (Wiley, New York, 1970).

[70] M. Gell-Mann and M. L. Goldberger, Phys. Rev. **91**, 398 (1953).

[71] G. H. Rawitscher, Phys. Rev. C **9**, 2210 (1974).

[72] I. Thompson and M. Nagarajan, Physics Letters B **106**, 163 (1981).

[73] Y. Sakuragi, M. Yahiro, and M. Kamimura, Progress of Theoretical Physics **68**, 322 (1982).

[74] N. Austern, Y. Iseri, M. Kamimura, M. Kawai, G. Rawitscher, and M. Yahiro, Physics Reports **154**, 125 (1987).

[75] J. E. Bowsher, T. B. Clegg, H. J. Karwowski, E. J. Ludwig, W. J. Thompson, and J. A. Tostevin, Phys. Rev. C **45**, 2824 (1992).

[76] K. Rusek and K. W. Kemper, Phys. Rev. C **61**, 034608 (2000).

[77] N. Keeley and K. Rusek, Physics Letters B **375**, 9 (1996).

[78] A. Gavron, Phys. Rev. C **21**, 230 (1980).

[52] S. K. Pandit, A. Shrivastava, K. Mahata, V. V. Parkar, R. Palit, N. Keeley, P. C. Rout, A. Kumar, K. Ramachandran, S. Bhattacharyya, et al., Phys. Rev. C **96**, 044616 (2017).

[53] K. G. Prasad, Nucl. Instr. and Meth. B **40/41**, 916 (1989).

[54] B. Srinivasan, S. K. Singh, R. G. Pillay, M. B. Kurup, and M. K. Pandey, Pramana **57**, 651 (2001).

[55] M. B. Kurup, Pramana **59**, 811 (2002).

[56] R. Palit, S. Saha, J. Sethi, T. Trivedi, S. Sharma, B. Naidu, S. Jadhav, R. Donthi, P. Chavan, H. Tan, et al., Nucl. Instrum. Methods Phys. Res., Sect. A **680**, 90 (2012).

[57] S. Gil, R. Vandenbosch, A. J. Lazzarini, D.-K. Lock, and A. Ray, Phys. Rev. C **31**, 1752 (1985).

[58] V. V. Parkar, R. Palit, S. K. Sharma, B. S. Naidu, S. Santra, P. K. Joshi, P. K. Rath, K. Mahata, K. Ramachandran, T. Trivedi, et al., Phys. Rev. C **82**, 054601 (2010).

[59] R. Broda, M. Ishihara, B. Herskind, H. Oeschler, S. Ogaza, and H. Ryde, Nucl. Phys. A **248**, 356 (1975).

[60] H. Feshbach, Annals of Physics **5**, 357 (1958).

[61] H. Feshbach, Annals of Physics **19**, 287 (1962).

[62] W. Tobocman, Phys. Rev. C **12**, 741 (1975).

[63] A. Bohr and B. R. Mottelson, vol. 1 (Benzamin, New York, 1975).

[43] R. Rafiei, R. d. Rietz, D. H. Luong, D. J. Hinde, M. Dasgupta, M. Evers, and A. Diaz-Torres, Phys. Rev. C **81**, 024601 (2010).

[44] D. H. Luong, M. Dasgupta, D. J. Hinde, R. du Rietz, R. Rafiei, C. J. Lin, M. Evers, and A. Diaz-Torres, Phys. Rev. C **88**, 034609 (2013).

[45] D. Martinez Heimann, A. J. Pacheco, O. A. Capurro, A. Arazi, C. Balpardo, M. A. Cardona, P. F. F. Carnelli, E. de Barbará, J. O. Fernández Niello, J. M. Figueira, et al., Phys. Rev. C **89**, 014615 (2014).

[46] S. P. Hu, G. L. Zhang, J. C. Yang, H. Q. Zhang, P. R. S. Gomes, J. Lubian, J. L. Ferreira, X. G. Wu, J. Zhong, C. Y. He, et al., Phys. Rev. C **93**, 014621 (2016).

[47] O. Capurro, A. Pacheco, A. Arazi, P. Carnelli, J. F. Niello, and D. M. Heimann, Nucl. Phys. A **945**, 186 (2016).

[48] D. Chattopadhyay, S. Santra, A. Pal, A. Kundu, K. Ramachandran, R. Tripathi, D. Sarkar, S. Sodaye, B. K. Nayak, A. Saxena, et al., Phys. Rev. C **94**, 061602 (2016).

[49] D. R. Otomar, J. Lubian, P. R. S. Gomes, and T. Correa, Journal of Physics G: Nuclear and Particle Physics **40**, 125105 (2013).

[50] S. K. Pandit, A. Shrivastava, K. Mahata, N. Keeley, V. V. Parkar, P. C. Rout, K. Ramachandran, I. Martel, C. S. Palshetkar, A. Kumar, et al., Phys. Rev. C **93**, 061602 (2016).

[51] S. K. Pandit *et al.*, to be published.

[32] O. Sgouros, A. Pakou, D. Pierroutsakou, M. Mazzocco, L. Acosta, X. Aslanoglou, C. Betsou, A. Boiano, C. Boiano, D. Carbone, et al., Phys. Rev. C **94**, 044623 (2016).

[33] S. Santra, S. Kailas, V. V. Parkar, K. Ramachandran, V. Jha, A. Chatterjee, P. K. Rath, and A. Parihari, Phys. Rev. C **85**, 014612 (2012).

[34] J. Lei and A. M. Moro, Phys. Rev. C **95**, 044605 (2017).

[35] I. J. Thompson, Comput. Phys. Rep. **7**, 167 (1988).

[36] A. Diaz-Torres, Comput. Phys. Commun. **182**, 1100 (2011).

[37] C. Signorini, A. Edifizi, M. Mazzocco, M. Lunardon, D. Fabris, A. Vitturi, P. Scopel, F. Soramel, L. Stroe, G. Prete, et al., Phys. Rev. C **67**, 044607 (2003).

[38] A. Pakou et al., Phys. Lett. B **633**, 691 (2006).

[39] S. Santra, V. V. Parkar, K. Ramachandran, U. K. Pal, A. Shrivastava, B. J. Roy, B. K. Nayak, A. Chatterjee, R. K. Choudhury, and S. Kailas, Phys. Lett. B **677**, 139 (2009).

[40] F. Souza, C. Beck, N. Carlin, N. Keeley, R. L. Neto, M. de Moura, M. Munhoz, M. D. Santo, A. Suaide, E. Szanto, et al., Nucl. Phys. A **821**, 36 (2009).

[41] D. Luong, M. Dasgupta, D. Hinde, R. du Rietz, R. Rafiei, C. Lin, M. Evers, and A. Diaz-Torres, Phys. Lett. B **695**, 105 (2011).

[42] E. C. Simpson, K. J. Cook, D. H. Luong, S. Kalkal, I. P. Carter, M. Dasgupta, D. J. Hinde, and E. Williams, Phys. Rev. C **93**, 024605 (2016).

[22] L. F. Canto, P. R. S. Gomes, R. Donangelo, and M. Hussein, Phys. Rep. **426**, 1 (2006).

[23] A. Shrivastava, A. Navin, N. Keeley, K. Mahata, K. Ramachandran, V. Nanal, V. V. Parkar, A. Chatterjee, and S. Kailas, Phys. Lett. B **633**, 463 (2006).

[24] K. Pfeiffer, E. Speth, and K. Bethge, Nucl. Phys. A **206**, 545 (1973).

[25] J. L. Québert, B. Frois, L. Marquez, G. Sousbie, R. Ost, K. Bethge, and G. Gruber, Phys. Rev. Lett. **32**, 1136 (1974).

[26] J. R. Hurd, D. R. James, J. J. Bevelacqua, and L. R. Medsker, Phys. Rev. C **20**, 1208 (1979).

[27] C. M. Castaneda, H. A. Smith Jr., P. Singh, J. Jastrzebski, H. Karwowski, and A. Gaigalas, Phys. Lett. B **77**, 371 (1978).

[28] H. Utsunomiya, S. Kubono, M. H. Tanaka, M. Sugitani, K. Morita, T. Nomura, and Y. Hamajima, Phys. Rev. C **28**, 1975 (1983).

[29] V. Tripathi, A. Navin, V. Nanal, R. G. Pillay, K. Mahata, K. Ramachandran, A. Shrivastava, A. Chatterjee, and S. Kailas, Phys. Rev. C **72**, 017601 (2005).

[30] A. Shrivastava, A. Navin, A. Diaz-Torres, V. Nanal, K. Ramachandran, M. Rejmund, S. Bhattacharyya, A. Chatterjee, S. Kailas, A. Lemasson, et al., Phys. Lett. B **718**, 931 (2013).

[31] A. Diaz-Torres, D. J. Hinde, J. A. Tostevin, M. Dasgupta, and L. R. Gasques, Phys. Rev. Lett. **98**, 152701 (2007).

[12] D. Tilley, C. Cheves, J. Godwin, G. Hale, H. Hofmann, J. Kelley, C. Sheu, and H. Weller, Nucl. Phys. A **708**, 3 (2002).

[13] Z. H. Li, E. T. Li, B. Guo, X. X. Bai, Y. J. Li, S. Q. Yan, Y. B. Wang, G. Lian, J. Su, B. X. Wang, et al., The European Physical Journal A **44**, 1 (2010).

[14] Y. Kanada-En'yo and T. Suhara, Phys. Rev. C **85**, 024303 (2012).

[15] J. S. Vaagen, D. K. Gridnev, H. Heiberg-Andersen, B. V. Danilin, S. N. Ershov, V. I. Zagrebaev, I. J. Thompson, M. V. Zhukov, and J. M. Bang, Physica Scripta **2000**, 209 (2000).

[16] A. Lemasson, A. Navin, N. Keeley, M. Rejmund, S. Bhattacharyya, A. Shrivastava, D. Bazin, D. Beaumel, Y. Blumenfeld, A. Chatterjee, et al., Phys. Rev. C **82**, 044617 (2010).

[17] A. Chatterjee, A. Navin, A. Shrivastava, S. Bhattacharyya, M. Rejmund, N. Keeley, V. Nanal, J. Nyberg, R. G. Pillay, K. Ramachandran, et al., Phys. Rev. Lett. **101**, 032701 (2008).

[18] I. Tanihata, T. Kobayashi, O. Yamakawa, S. Shimoura, K. Ekuni, K. Sugimoto, N. Takahashi, T. Shimoda, and H. Sato, Physics Letters B **206**, 592 (1988).

[19] B. D. Fields, Annual Review of Nuclear and Particle Science **61**, 47 (2011).

[20] S. Abrahamyan et al. (PREX Collaboration), Phys. Rev. Lett. **108**, 112502 (2012).

[21] R. J. de Meijer and R. Kamermans, Rev. Mod. Phys. **57**, 147 (1985).

# Bibliography

[1] G. Baur, C. Bertulani, and H. Rebel, Nuclear Physics A **458**, 188 (1986).

[2] C. Bertulani and T. Kajino, Progress in Particle and Nuclear Physics **89**, 56 (2016).

[3] J. J. Kolata, V. GuimarÃčes, and E. F. Aguilera, Eur. Phys. J. A **52**, 123 (2016).

[4] L. F. Canto, P. R. S. Gomes, R. Donangelo, J. Lubian, and M. Hussein, Phys. Rep. **596**, 1 (2015).

[5] N. Keeley, N. Alamanos, K. W. Kemper, and K. Rusek, Prog. Part. Nucl. Phys. **63**, 396 (2009).

[6] N. Keeley, R. Raabe, N. Alamanos, and J. Sida, Progress in Particle and Nuclear Physics **59**, 579 (2007).

[7] I. Tanihata, H. Hamagaki, O. Hashimoto, Y. Shida, N. Yoshikawa, K. Sugimoto, O. Yamakawa, T. Kobayashi, and N. Takahashi, Phys. Rev. Lett. **55**, 2676 (1985).

[8] T. Aumann, Journal of Physics: Conference Series **381**, 012008 (2012).

[9] C. Broggini, L. Canton, G. Fiorentini, and F. Villante, Journal of Cosmology and Astroparticle Physics **2012**, 030 (2012).

[10] M. Freer, Reports on Progress in Physics **70**, 2149 (2007).

[11] H. Horiuchi, K. Ikeda, and K. Kato, Progress of Theoretical Physics Supplement **192**, 1 (2012).

tract the relative contributions of the $p$- $d$- $t$-capture processes, which can not be separated by only particle-$\gamma$ coincidence method.

4. Extension of similar studies with exotic unstable nuclei:

The documented analysis method will be useful to study reaction dynamics involving exotic unstable nuclei (e.g. $^{6,8}$He, $^{8-11}$Li, $^{7,11}$Be etc.), for which beam current is very low. It will be interesting to study the breakup and fragment-capture reaction processes involving neutron deficient nucleus $^{7}$Be ($\alpha$+$^{3}$He), which is mirror nucleus of $^{7}$Li ($\alpha + t$).

standing of the reaction dynamics involving weakly bound stable nuclei. The data set can be used to improve the existing models as well as to develop a single theoretical model for simultaneous estimations of breakup, transfer breakup, complete fusion, and fragment-capture reactions.

## 7.2 Future outlook

In near future it will be interesting to extend the present study to reaction channels that could not be measured in this thesis work. Some of the possible studies along with the improved detection setup are listed below.

1. Breakup processes leading to neutrons in the outgoing channels:

   The influence of transfer breakup processes, where ejectile breaks into the configuration of neutrons+$x$ (e.g., $^5$He$\to \alpha + n$, $^6$He$\to \alpha + n + n$, $^8$Li$\to$ $^7$Li $+ n$, etc.) are of interest. These reaction processes can be studied from a coincidence measurement between the out going neutrons and charged particles employing the neutron detector array, that is being developed.

2. Efficient Particle-$\gamma$ coincidence measurements:

   Implementation of a charged particle detector array together with the $\gamma$-detector array will enable us to investigate fragment-capture processes that have low cross sections (e.g., capture of $^{5,6}$He). This information can be useful for studying nuclear structure of the nuclei formed as $^{5,6}$He $+$ target using a $^7$Li beam.

3. Particle-$\gamma$-*neutron* triple coincidence:

   A triple coincidence measurement of particle-$\gamma$-*neutron* can be used to ex-

ments of breakup fragments along with theoretical analysis show unambiguously that the cross sections of $1n$-stripping account for $\sim 2$ % and $1p$-pickup only $\sim 0.8$ % of the inclusive $\alpha$ yields. Overall, the combination of measurements and calculations suggests that at most only $\sim 8$ % of the inclusive $\alpha$ yield can be accounted for by non-capture breakup processes. To identify the reaction mechanisms responsible for the remaining unaccounted $\alpha$-particle yields, measurements of prompt $\gamma$-rays in coincidence with the $\alpha$-particle in the outgoing channels have been carried out. The relative yields of $\gamma$-rays from residues of $t$-capture are found to be more than those from the other processes. The $2n$-stripping channel, contributing to the $\alpha$ particle yield via breakup of the unbound $^5$Li, has also been obtained by counting the $\gamma$ rays corresponding to radioactive decay of $^{95}$Nb. The measurements show that the $t$-capture mechanism is the dominant reaction channel for the production of $\alpha$-particle and account for 60-75% of the measured $\alpha$-inclusive cross sections. The estimated $\alpha$-evaporation cross sections from the statistical model calculations account for 10-20% of the $\alpha$-inclusive cross sections. The combination of $\alpha$-production due to, (a) $t$-capture, (b) evaporation from compound nucleus, and (c) breakup and nucleon transfer followed by breakup, explain $\sim$95% of the measured $\alpha$-inclusive cross sections for $^7$Li + $^{93}$Nb system at the measured energy range. For the first time, allmost all the $\alpha$-yield has been accounted for $^7$Li induced reaction. A systematic study of the $t$-capture and inclusive $\alpha$ cross sections for reactions involving $^7$Li on various targets over a wide mass range has also been performed.

In the present work, we have measured absolute cross sections for all major reaction channels dealing with breakup processes. The rather complete nature of the data set combined with different theoretical calculations improved the under-

provide an important benchmark.

The fragment-capture reaction mechanism has been studied by measuring prompt γ-rays arising from the residue in coincidence with the outgoing fragments for $^7$Li+$^{93}$Nb system. The absolute cross sections for $t$-capture and $\alpha$-capture along with the complete fusion have been measured at energies 23.6, 25.6, 27.7, and 29.7 MeV using the in-beam and off-beam γ-ray counting methods. Statistical model calculations have been performed to estimate the compound nuclear contribution to the cross sections of residues populated in $t$-capture and $\alpha$-capture reactions. The measured $t$-capture cross sections are found to be greater than the $\alpha$-capture cross sections at all energies.

A consistent analysis of non-capture breakup, $t$-capture, $\alpha$-capture, and complete fusion reactions has been performed for the first time at several energies using three-body dynamical trajectory model calculations [31] to understand whether the observed fragment-capture is a direct and/or two-step process. The relative population of different residues due to the fragment-capture reactions has been reproduced by using the angular momentum distribution and excitation energy from trajectory model as input to statistical model calculations. The results suggest, the dominant mechanism for fragment-capture is breakup of $^7$Li followed by the capture. In addition, the predicted direct $p$- $d$- $t$-stripping cross sections from Distorted wave Born approximation are negligible relative to measured corresponding capture cross sections. This result also supports the dominance of the two step process, breakup followed by fusion, over the one step process of stripping of the fragment.

The origin of the large inclusive-$\alpha$ cross section has also been investigated for the $^7$Li+$^{93}$Nb system at energies around the Coulomb barrier. The exclusive measure-

has been developed using the Monte Carlo technique to interpret the observables of different breakup processes and estimate the efficiency for coincident detection of the breakup fragments. Angular distributions for elastic scattering and nucleon transfer to bound states have also been measured. From the extensive analysis of the data along with calculations, it has been shown that the $\alpha+d$ and $\alpha+\alpha$ coincidences mostly result from direct $1n$-stripping to the $^6\text{Li}_{3_1^+}$ state and $1p$-pickup to the $^8\text{Be}_{\text{g.s.}}$ state, respectively. The cross sections for $\alpha+d$ events are found to be larger than those for $\alpha+t$ events due to the breakup of $^7\text{Li}_{\frac{7}{2}+}$. These results signify the dominance of $n$-stripping followed by breakup over the direct breakup of $^7\text{Li}$ from the $\frac{7}{2}^+$ resonance state, in agreement with the results reported in the earlier studies with $^7\text{Li}+^{65}\text{Cu}$ system [23]. The breakup probability of $^7\text{Li}$ from continuum states are found to be order of magnitude less than the breakup from resonance state $\frac{7}{2}^+$. The measured cross sections for $1p$-pickup (with a large positive $Q_{\text{gg}}$) are found to be smaller than those for $1n$-stripping at all energies for both the systems, which could be attributed to poor kinematical matching [83].

Continuum discretized coupled channels (CDCC) and coupled channels Born approximation (CCBA) calculations have been performed to analyze a comprehensive data set comprising elastic scattering, direct breakup and transfer-breakup. The CCBA calculations agree well with the $\alpha+d$ and $\alpha+\alpha$ coincidence data, both in terms of the shapes of the angular distributions and the absolute cross sections. Population of the $^6\text{Li}_{\text{g.s.}}$ is also reproduced by the same calculations. Calculations omitting direct population of the $^6\text{Li}_{\text{g.s.}}$ confirmed that transfer to the $^6\text{Li}_{\text{g.s.}}$ state followed by excitation of the $3_1^+$ resonance makes a negligible contribution.

In this respect, the rather complete data sets for the breakup and transfer-breakup mechanisms for a stable weakly bound nucleus plus the theoretical analysis

# 7

# Summary, conclusion and future outlook

The reaction dynamics involving weakly bound nucleus $^7$Li, populating the continuum states, has been investigated. In the first part of the investigation, we have studied the reaction processes, where none of the breakup fragments are captured by the target and can be detected in coincidence. In the second part of the investigation, the fragment capture reaction mechanisms have been studied. The source of large $\alpha$-production cross section has been investigated by measuring almost all the reaction channels contributing to the $\alpha$-yield.

## 7.1   Summary and Conclusion

The present thesis reports the first simultaneous measurement of absolute differential cross sections for both 1$p$-pickup and 1$n$-stripping followed by breakup of the ejectile as well as direct breakup of the weakly bound projectile over a wide angular range. The investigation has been carried out for two different system $^7$Li+$^{89}$Y and $^7$Li+$^{93}$Nb at several energies near the Coulomb barrier. A simulation code